

MIXED FINITE ELEMENT METHODS
FOR DISCRETIZATION AND STREAMLINE TRACING

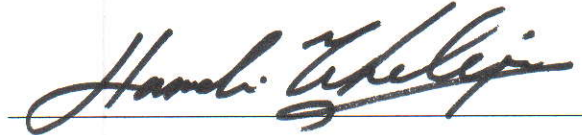
A DISSERTATION
SUBMITTED TO THE DEPARTMENT OF ENERGY
RESOURCES ENGINEERING
AND THE COMMITTEE ON GRADUATE STUDIES
OF STANFORD UNIVERSITY
IN PARTIAL FULFILLMENT OF THE REQUIREMENTS
FOR THE DEGREE OF
DOCTOR OF PHILOSOPHY

Sébastien François Matringe

June 2008


© Copyright by Sébastien François Matringe 2008
All Rights Reserved

I certify that I have read this dissertation and that, in my opinion, it is fully adequate in scope and quality as a dissertation for the degree of Doctor of Philosophy.

A handwritten signature in black ink, reading "Hamdi A. Tchelepi", written over a horizontal line.

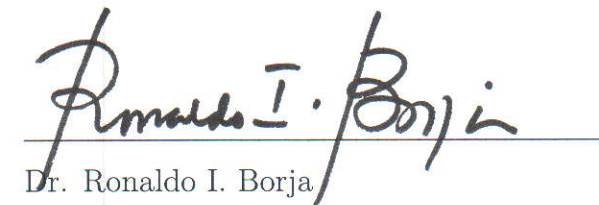
Dr. Hamdi A. Tchelepi Principal Advisor

I certify that I have read this dissertation and that, in my opinion, it is fully adequate in scope and quality as a dissertation for the degree of Doctor of Philosophy.

A handwritten signature in black ink, reading "Ruben Juanes", written over a horizontal line.

Dr. Ruben Juanes Advisor

I certify that I have read this dissertation and that, in my opinion, it is fully adequate in scope and quality as a dissertation for the degree of Doctor of Philosophy.

A handwritten signature in black ink, reading "Ronaldo I. Borja", written over a horizontal line.

Dr. Ronaldo I. Borja

Approved for the University Committee on Graduate Studies.

Abstract

This thesis develops mixed finite-element (MFE) methods for the discretization and numerical simulation of the reservoir flow equations. MFE methods provide the proper framework for the interpretation and theoretical analysis of multipoint flux approximations (MPFA), which are the industry standard discretization methods for reservoir simulation on advanced grids. The key contributions of this research are: (1) a proof of convergence of MPFA methods on three-dimensional rectangular parallelepipedic grids, and (2) a new streamline tracing method that gives exact streamlines from MPFA discretizations.

On two-dimensional triangular, or quadrilateral grids, and on three-dimensional tetrahedral grids, Wheeler and Yotov employed the first-order Brezzi–Douglas–Marini (BDM₁) space to provide the link between MPFA and MFE methods, which allowed them to prove convergence of MPFA on such grids. On hexahedral grids, however, a different velocity space must be introduced to establish the bridge between MFE and MPFA discretizations.

In this dissertation, we present a new velocity space on three-dimensional hexahedra. The new velocity space is defined using four degrees of freedom per face, which are the normal components of the velocity field at the vertices of each face. The new space is compatible in the sense of Babuška and Brezzi with a piecewise constant pressure discretization and therefore yields a consistent MFE method. An error analysis of the new MFE discretization proves its convergence and leads to error

estimates for the scalar and vector variables.

The application of a vertex-based quadrature rule reduces the new MFE to the widely used MPFA O-method on three-dimensional hexahedra. This represents the first direct link between MFE and MPFA on hexahedral grids, which we exploit to provide a proof of convergence of the MPFA O-method, along with error estimates for the pressure and velocity fields.

In the context of streamline simulation, the quality of the velocity field is essential to the accuracy of the overall method. The streamlines are traced by integration of the velocity field, which is interpolated from the MPFA fluxes. Current streamline tracing algorithms rely on low-order velocity reconstruction techniques that do not preserve the accuracy of the fluxes computed by MPFA discretizations. On advanced grids, this can lead to $O(1)$ numerical errors.

In this work, we exploit the links between MPFA and MFE methods to interpret the MPFA fluxes as MFE degrees of freedom. The MPFA velocity field is then reconstructed through interpolation of the fluxes by the MFE velocity shape functions. Therefore, the streamlines are traced on the velocity field corresponding exactly to the MPFA discretization. After a detailed description of the streamline tracing algorithm, we provide comparisons of low- and high-order accurate tracing methods by means of challenging numerical experiments.

Acknowledgments

I feel extremely privileged to have spent my graduate studies in the department of Energy Resources Engineering at Stanford. This has been an exceptional learning and personal experience for me. I take this opportunity to thank some of the many people who contributed to making this experience a wonderful one.

First and foremost, I would like to thank my advisors, Hamdi Tchelepi and Ruben Juanes. This work would never have been completed without their help and guidance, and for that, I am deeply indebted to them. Beyond the technical advice, I am grateful for the manner in which we interacted. They managed to keep an ideal balance between giving me the independence necessary for creativity, and following my work closely during challenging times.

I thank Ronaldo Borja for his careful reading of the draft manuscript and valuable input in my work. I also wish to thank Peter Pinsky and Roland Horne for being in my examination committee.

I address my sincere gratitude to the faculty members of the department of Energy Resources Engineering, who taught me so much and so well. I also thank the department staff for their tremendous help in assisting me with all the administrative matter.

Funding from the Stanford University Petroleum Research Institute – Reservoir Simulation (SUPRI-B) program is gratefully acknowledged. It has been an honor to belong to such a talented and dynamic group of individuals.

I would also like to thank the various teams in which I spent almost a year's worth of internships at ConocoPhillips, ExxonMobil and Chevron. These interactions with the petroleum industry have been extremely rewarding and have helped put my work into perspective.

At a more personal level, I wish to thank all my friends from Stanford and beyond, whose company has made my years here memorable ones. I would like to dedicate this work, to my family, Ghislaine, François, Laurence and Hadrien for their support and love.

Contents

Abstract	iv
Acknowledgments	vi
1 Introduction	1
1.1 Reservoir simulation grids	1
1.1.1 Geological models	1
1.1.2 Simulation models	3
1.2 Governing equations	5
1.2.1 Single phase flow	5
1.2.2 Multiphase flow	6
1.2.3 The fractional flow formulation	7
1.3 Finite volume discretizations	9
1.3.1 Two-point flux approximation	12
1.3.2 Multipoint flux approximations	14
1.4 Streamline simulation	16
1.5 Problem statement	18
1.6 Thesis overview	19
2 Mixed finite element methods	22

2.1	The mixed variational formulation	22
2.2	Discretization	25
2.3	Numerical integration	27
2.4	Solution of the MFE system	27
2.5	The reference element	28
2.5.1	Coordinate mapping	28
2.5.2	The Piola transform	31
2.6	Velocity spaces	31
2.6.1	Compatible mixed finite elements	31
2.6.2	The lowest-order Raviart–Thomas–Nédélec space	32
2.6.3	The first-order Brezzi–Douglas–Marini space	33
3	MPFA as a new MFE method	38
3.1	Relationship between FV and MFE methods	38
3.2	A new mixed finite element	40
3.2.1	Velocity space	41
3.2.2	Pressure space	45
3.2.3	The new mixed finite element	45
3.3	Trapezoidal quadrature	47
3.4	Localization into MPFA	48
3.5	Numerical experiments	54
3.5.1	Patch tests	54
3.5.2	Monotonicity properties	57
3.6	Summary	59
4	Convergence analysis	61
4.1	Consistency and convergence of the new MFE	61
4.2	Consistency and convergence of MPFA	65

4.2.1	Consistency	65
4.2.2	Preliminary results	65
4.2.3	Velocity error analysis	70
4.2.4	Pressure error analysis	73
4.3	Numerical experiments	74
5	A new framework for streamline tracing	78
5.1	Streamline tracing for MFE discretizations	79
5.1.1	General strategy	79
5.1.2	Tracing in the reference space	80
5.1.3	Integration of the streamline path	81
5.1.4	Time-of-flight computation	82
5.2	Streamline tracing for FV discretizations	83
5.2.1	A new approach	83
5.2.2	Low-Order Tracing	84
5.2.3	High-Order Tracing	84
5.3	Numerical Experiments	86
5.3.1	Mixed finite element discretizations	86
5.3.2	MPFA discretizations	97
5.3.3	Three-dimensional unstructured grids	104
6	Conclusions and Future Work	111
6.1	Conclusions	111
6.2	Future work	113
	Bibliography	115

List of Tables

3.1	Average time-of-flight error of the various discretizations on the three patch tests.	55
4.1	Error values and convergence rates for the first example.	76
4.2	Error values and convergence rates for the second example.	77
5.1	Average time-of-flight error for the diagonal flow problem.	90
5.2	Average time-of-flight error in the presence of heterogeneity.	93
5.3	Average time-of-flight error for the heterogeneous unstructured grid test case.	96
5.4	Relative time of flight error for each streamline traced on the chevron grids.	101
5.5	Relative time of flight error for the streamlines traced on the unstructured grid.	106

List of Figures

1.1	Schematic of the two-point flux approximation method for one-dimensional problems.	13
1.2	5-point (\times) and 9-point (\circ) stencils corresponding to the TPFA and MPFA methods on a two dimensional Cartesian grid.	13
1.3	MPFA stencil for a two-dimensional structured quadrilateral grid. . .	15
1.4	Interaction region (dashed line) for a sub-interface flux in MPFA on a two-dimensional structured quadrilateral grid.	15
2.1	Mapping of triangular elements.	29
2.2	Mapping of quadrilateral elements.	29
2.3	Mapping of tetrahedral elements.	30
2.4	Mapping of hexahedral elements.	30
2.5	Two-dimensional RTN_0 shape functions for the top edge of the reference triangle (left) and quadrilateral (right).	34
2.6	Three-dimensional RTN_0 shape functions for the top face of the reference tetrahedron (left) and hexahedron (right).	34
2.7	The two BDM_1 recirculation shape functions for the top face of the reference hexahedron.	37
3.1	The four vertex-based MJT shape functions for the top face of the reference hexahedron.	49

3.2	Representation of the four vertex-based MJT velocity degrees of freedom associated with a face of a three-dimensional Cartesian grid. . .	50
3.3	The eight elements (dotted line) and twelve subfaces (solid lines) of an MPFA interaction region and their associated twelve MJT velocity degrees of freedom (arrows) for a three-dimensional Cartesian grid. . .	51
3.4	Stencils of the fully-integrated (top) and localized new mixed finite element method in the case of diagonal (bottom-left) and full-tensor (bottom-right) permeability coefficients.	53
3.5	Matrix of the localized M -based MFE for a $5 \times 5 \times 5$ grid, reproducing the well-known structure of the 27-point stencil.	54
3.6	RT_0 (left) failing and BDM_1 (right) passing the first patch test involving elements in shape of truncated pyramids.	56
3.7	RT_0 (left) failing and BDM_1 (right) passing the second patch test involving a nonplanar face.	56
3.8	$4 \times 4 \times 4$ grid of general hexahedra used for the third patch test. . . .	57
3.9	Streamlines obtained by RT_0 (top-left), fully integrated BDM_1 (top-right), fully integrated MJT (bottom-left) and localized MJT (bottom-right) for the third patch test.	58
3.10	Monotonicity test of the various discretization methods for a rotating permeability tensor with 100/1 anisotropy ratio.	60
5.1	RTN_0 streamlines for the uniform flow problem on a Cartesian (top-left), chevron (top-right), random (bottom-left) and skewed (bottom-right) grids.	88
5.2	RTN_0 (left) and BDM_1 (right) streamlines on a quadrilateral chevron grid.	90

5.3	RTN ₀ (left) and BDM ₁ (right) streamlines on a triangular Cartesian grid.	91
5.4	Permeability field employed, taken from a test case in [56]. Permeability values: white = 1; light gray = 10 ⁻¹ ; dark gray = 10 ⁻² ; black = 10 ⁻³	92
5.5	RTN ₀ (left) and BDM ₁ (right) streamlines for a grid of 200 triangular elements.	93
5.6	RTN ₀ (left) and BDM ₁ (right) streamlines for a grid of 3200 triangular elements.	93
5.7	Average time-of-flight error as a function of the number of unknowns for a sequence of triangular grids.	94
5.8	Base case for the unstructured grid discretization.	95
5.9	RTN ₀ (left) and BDM ₁ (right) streamlines for a 148-element grid. . .	96
5.10	RTN ₀ (left) and BDM ₁ (right) streamlines for a 350-element grid. . .	96
5.11	Pressure solution on the quadrilateral chevron grid and reference streamlines.	99
5.12	Streamlines traced on the quadrilateral chevron grid with the RTN ₀ (solid lines) and BDM ₁ (dotted lines) velocity fields.	100
5.13	Pressure solution on the triangular chevron grid and reference streamlines.	100
5.14	Streamlines traced on the triangular chevron grid with the RTN ₀ (solid lines) and BDM ₁ (dotted lines) velocity fields.	101
5.15	MPFA streamlines from the RTN ₀ and BDM ₁ -based tracing (overlapping exactly).	103
5.16	Location of the streamline launching points on the edges of the gridcell containing the injection well.	104
5.17	Coarse unstructured grid and permeability field.	105

5.18 Reference unstructured grid.	105
5.19 Streamlines traced on the reference unstructured grid.	106
5.20 Streamlines traced on the coarse unstructured grid with the RTN_0 (top) and BDM_1 (bottom) based tracing.	107
5.21 Top view of the synthetic reservoir.	109
5.22 Side view of the synthetic reservoir.	109
5.23 Full set of streamlines necessary to solve the transport problem . . .	110
5.24 A selection of representative streamlines traced using the BDM_1 -based method	110

Chapter 1

Introduction

This chapter presents the challenges posed by modern reservoir simulation grids on the discretization of the traditional and streamline-based reservoir simulation equations, defines our objectives and outlines the contents of the thesis.

1.1 Reservoir simulation grids

1.1.1 Geological models

Petroleum reservoirs are hydrocarbon bearing geologic formations. The reservoir rock is a porous medium filled with a variety of chemical components (hydrocarbons, water, gases, etc) that can form several fluid phases. Reservoir models play a central role in the development and production of petroleum fields. They are used to understand, monitor and predict the flow of reservoir fluids in order to optimize the hydrocarbon production.

The most challenging task in building a reliable reservoir model is the accurate representation of the geology. The remote subsurface location of petroleum reservoirs limits the amount and quality of data available for their characterization. Actual

measurements of rock properties is only possible at the wells, which leads to very sparse *hard* data sets. Remote sensing techniques based on geophysical principles such as seismic imaging are used to infer rock properties between the wells. However, the seismic data are composed of impedance and velocity measurements that are only an indirect measure of the rock porosity. Complex deconvolution techniques are required to interpret the seismic data as *soft* geological data. Current technologies allow large-scale reservoir features, such as the geometry of trapping structures, bedding horizons, faults or fractures to be visible in the deconvoluted seismic images. However, small-scale geological features, such as porosity or permeability variations within a depositional bed, are hard to distinguish from the noise in the seismic signal that traveled through miles of rock. Geophysical data are therefore only exploitable to determine the main geological features of petroleum reservoirs.

Geostatistical methods are used to integrate the hard data at the wells and the soft geophysical data into a realistic and coherent geologic model, and to represent in a statistical sense the small-scale rock property variations invisible in the soft data. The main objective is to represent the property (e.g. porosity and permeability) distributions properly, which is the key factor in a reservoir flow response. The first step in building a geostatistical model is to understand the reservoir geology. The types of deposition, erosion and deformation that created and transformed the reservoir are inferred from the general geology of the field area as well as from analog outcrops and from the hard and soft data available. The geological assumptions are then translated by geostatistical methods into spatial correlation models. Two main types of geostatistics are used to model spatial correlation structures: two-point statistics, based on variogram models, and multipoint statistics, based on training images [18; 29; 36; 65]. Typically, multipoint statistics are used to generate realistic depositional, or erosional, patterns and to determine the distributions of the geological facies within the reservoir. Within each facies, the spatial variations in the rock

properties, such as porosity or permeability, are then modeled through two-point statistics.

Modern reservoir characterization techniques lead to highly detailed geological models. Reservoirs are usually represented by a hexahedral grid, fine enough to accurately render the complex geometry of the main geological features and to properly account for the rock property variations, which are both essential for reliable modeling of reservoir flow performance. The grid is also usually distorted to better follow the geology [47] and each gridblock is assigned a porosity and a permeability value.

1.1.2 Simulation models

The high level of detail displayed in the geological models (or *geomodels*) limits their use for flow simulation applications. These models commonly have on the order of 10^7 or 10^8 gridblocks. Despite the fast progress of parallel computing techniques, solving complex flow and transport problems on such grids remains out of reach. Even if direct flow simulation is possible on the geomodel, it is simply too slow to be routinely used by reservoir engineers.

To perform flow simulations, a model of manageable size (10^5 or 10^6 gridblocks) is usually constructed. *Upscaling* techniques are used to generate this coarser reservoir model from the high-resolution geomodel. A variety of upscaling methods exist and are employed throughout the industry [21; 32]. The challenge is to build a grid that retains the important flow characteristics of the geological model.

Nowadays, selection of the geological features that are of significance for flow simulations is usually based on a simple single-phase flow simulation performed on the geomodel. Because of its efficiency, the streamline method is often used to perform this first rough estimation of the reservoir flow behavior [40; 61]. The streamlines provide a natural way to select the geological features to retain in the simulation model.

Features at a variety of scales need to be accounted for. Some large scale features, such as major faults or pinchouts often play an essential role in the reservoir flow behavior. Other large-scale characteristics like some depositional layerings have minimal impact on the flow behavior and are often discarded. Similarly, some small high-permeability streaks or some small fractures often have a dramatic effect on the flow, while the streamlines might be completely insensitive to other small-scale geological features.

To limit the numerical errors, the simulation grid is designed to follow closely the geological structures that have a strong impact on the flow behavior. The vast majority of simulation grids are composed of general hexahedral elements that are distorted to accommodate the geological geometries. Unstructured grids, composed of more general-shaped elements, such as tetrahedra, have recently gained popularity. Their inherent flexibility allows them to conform to complex geometries with much less elements than required by structured hexahedral grids.

Once the simulation grid is created, it must be populated with porosity and permeability values that provide the simulation grid with the same flow characteristics as the geostatistical grid. A variety of methods have been devised to obtain upscaled rock properties equivalent to the fine scale geology. To properly represent geological features that are not necessarily aligned with the simulation grid, tensor permeability coefficients are necessary [21; 32].

In this thesis, we will consider reservoir simulation grids composed of general triangles or quadrilaterals in two dimensions and general tetrahedra or hexahedra in three dimensions. The general hexahedral elements are by far the most commonly used in the oil industry, and they play a central role in this work. Unless otherwise mentioned, the grids considered can be distorted, but for simplicity their elements must remain properly defined (non-degenerate) and convex. General full permeability tensors are considered, with the restriction that they must remain symmetric and

positive definite, for physical reasons.

1.2 Governing equations

Although petroleum engineering problems rarely involve a single fluid phase, the single phase flow problem plays a central role in the development of numerical simulation techniques. This section therefore begins with a description of this simple flow problem. We then present the complexities introduced when several fluid phases are flowing simultaneously through the porous rock. The last part shows how these complications are usually handled by introducing the fractional flow formulation.

1.2.1 Single phase flow

Let us consider a single fluid phase flowing in the porous rock. Darcy's law states that a fluid moves through a porous medium with a volumetric velocity \mathbf{u} inversely proportional to the potential gradient $\nabla\Phi$

$$\mathbf{u} = -\frac{\mathbf{k}}{\mu}\nabla\Phi, \quad (1.1)$$

where \mathbf{k} is a symmetric positive definite tensor representing the rock permeability and μ represents the fluid dynamic viscosity. The potential Φ combines a pressure and a gravity term:

$$\Phi = p + \rho g D, \quad (1.2)$$

where p , ρ , g and D are respectively, the fluid pressure and density, the gravitational constant and the depth.

In the remainder of this thesis, we will neglect gravity effects and identify the flow potential with the fluid pressure. It is understood that if the gravity term is non-negligible, the pressure has to be replaced by the full expression of the flow potential.

The continuity equation, stating the conservation of mass of the fluid phase, reads

$$\frac{\partial \phi \rho}{\partial t} + \nabla \cdot (\rho \mathbf{u}) = \rho f, \quad (1.3)$$

where ϕ is the rock porosity and f is a volumetric source term. If the fluid and rock are assumed incompressible, (1.3) is simplified into

$$\nabla \cdot \mathbf{u} = f, \quad (1.4)$$

which is combined with (1.1) to give the second-order pressure equation:

$$-\nabla \cdot \frac{\mathbf{k}}{\mu} \nabla p = f. \quad (1.5)$$

Since \mathbf{k} is positive definite and $\mu > 0$, (1.5) forms an elliptic problem, which would become parabolic for compressible flow.

1.2.2 Multiphase flow

Consider, for simplicity, two immiscible and incompressible fluid phases. A more comprehensive presentation of multiphase flow problems can be found in [10] or [20]. The wetting phase is denoted w (e.g. water) and the non-wetting phase o (e.g. oil.) The two phases share the pore space, and we denote by S_w and S_o their respective saturations linked through

$$S_w + S_o = 1. \quad (1.6)$$

Capillary effects allow the two phases to have distinct pressures, p_w and p_o , linked by the capillary pressure function

$$P_c(S_w) = p_o - p_w, \quad (1.7)$$

where P_c is in general considered to be a function of the wetting phase saturation. Capillary effects can be included in the formulation by using the global pressure [20]. Here, we assume negligible capillary forces and write

$$p = p_o = p_w. \quad (1.8)$$

Under the incompressibility assumption, the mass balance of either phase reads

$$\phi \frac{\partial S_\alpha}{\partial t} + \nabla \cdot \mathbf{u}_\alpha = f_\alpha, \quad (1.9)$$

where α represents either phase ($\alpha = o, w$). f_α is the α -phase volumetric source term. The volumetric α -phase velocity \mathbf{u}_α is given by Darcy's law

$$\mathbf{u}_\alpha = -\frac{k_{r\alpha}}{\mu_\alpha} \mathbf{k} \nabla p = -\lambda_\alpha \mathbf{k} \nabla p, \quad (1.10)$$

modified in the case of multiphase flow by introducing the relative permeability $k_{r\alpha}$. Here μ_α and λ_α are respectively the α -phase viscosity and mobility.

1.2.3 The fractional flow formulation

The solution of the multiphase flow equations is greatly simplified by using the fractional flow formulation that leads to a pressure equation and a saturation equation (or a set of saturation equations when more than two phases are present). We introduce the total velocity

$$\mathbf{u} = \mathbf{u}_w + \mathbf{u}_o, \quad (1.11)$$

which can be written

$$\mathbf{u} = -(\lambda_w + \lambda_o) \mathbf{k} \nabla p = -\lambda \mathbf{k} \nabla p, \quad (1.12)$$

where we use λ to represent the total fluid mobility.

The continuity equation for the total fluid velocity is obtained by summing both equations of (1.9) and using (1.6):

$$\nabla \cdot \mathbf{u} = f_w + f_o = f, \quad (1.13)$$

where f is a total volumetric source term.

The combination of (1.12) and (1.13) yields the second-order pressure equation

$$-\nabla \cdot (\lambda \mathbf{k} \nabla p) = f. \quad (1.14)$$

The total mobility λ is always strictly positive, which provides an elliptic character to the pressure equation. Once again, as in the single phase case, the compressibility effects would make the pressure equation parabolic.

To obtain the saturation equation, we introduce the fractional flow function

$$\varphi_w = \frac{\lambda_w}{\lambda}, \quad (1.15)$$

that is used to express the wetting phase velocity in terms of the total velocity:

$$\mathbf{u}_w = \varphi_w \mathbf{u}. \quad (1.16)$$

Injecting (1.16) in (1.9) provides an equation relating the water saturation to the total fluid velocity:

$$\phi \frac{\partial S_w}{\partial t} + \nabla \cdot (\varphi_w \mathbf{u}) = f_w. \quad (1.17)$$

This saturation equation is hyperbolic in nature and becomes parabolic when the capillary effects are accounted for.

The fractional flow formulation allows a transformation of the problem (1.9) into the pressure and saturation equations of (1.14)–(1.17), which are coupled through

the total fluid velocity \mathbf{u} . The major advantage of this formulation is that it allows the use of distinct numerical methods to solve the two equations, which have very different mathematical properties.

General-purpose simulators model multi-component multiphase flow and transport in reservoirs. For such systems, while the number of coupled conservation equations grows with the number of components, the overall mathematical structure is similar to the simple two-phase flow problem just described. That is, the flow problem is described by a near-elliptic pressure equation, and the transport of the components is described by a set of near-hyperbolic conservation laws. The discretization operator is divided in two parts: (1) a static geometric part that accounts for permeability and geometry variations between the control volumes, and (2) a dynamic part, λ_p . The static part is obtained through a pre-processing step from the discretization of the elliptic pressure equation (1.14), and is provided to the simulator as input. In this work, we focus on the solution of the elliptic pressure equation. We present in the following section the classical discretization method used in the oil industry to solve this flow problem.

1.3 Finite volume discretizations

Let $\Omega \subset \mathbb{R}^d$ be the reservoir domain in dimension $d = 2, 3$. The simulation grid represents a partition \mathcal{T}_h of Ω into a set of N non-overlapping control volumes K_i , $i = 1, \dots, N$. Each gridcell is associated with a node \mathbf{x}_i located at its center.

The goal of finite volume (FV) methods is to compute numerically the pressure p_i in each gridblock K_i . To find the N pressure unknowns, an integral form of the mass balance equation is enforced on each control volume. Focusing on the elliptic problem of (1.4) or (1.13), the continuity equation is integrated over an element K_i

to give

$$\int_{K_i} \nabla \cdot \mathbf{u} \, dK_i = \int_{K_i} f \, dK_i. \quad (1.18)$$

The Gauss-Ostrogradsky theorem transforms the left-hand side into an integral on the boundary Γ_i of K_i :

$$\int_{\Gamma_i} \mathbf{u} \cdot \mathbf{n}_i \, d\Gamma_i = \int_{K_i} q \, dK_i, \quad (1.19)$$

where \mathbf{n}_i is the outward-pointing unit normal to Γ_i . We define the scalar flux out of the element K_i as

$$F_i := \int_{\Gamma_i} \mathbf{u} \cdot \mathbf{n}_i \, d\Gamma_i. \quad (1.20)$$

The flux F_i is linked to the fluid pressure by (1.1) or (1.12). We write

$$F_i = - \int_{\Gamma_i} \lambda (\mathbf{k} \nabla p) \cdot \mathbf{n}_i \, d\Gamma_i, \quad (1.21)$$

with the understanding that in the case of single-phase flow λ represents the inverse of the dynamic viscosity, and for multiphase flow λ is the total mobility. In essence, the multiphase pressure equation only differs from the single phase flow problem in that the mobility λ depends on the saturation (through the relative permeabilities).

Let us now introduce the set J_i of indices j of elements K_j sharing a face Γ_{ij} with element K_i . The total flux F_i is expressed as

$$F_i = \sum_{j \in J_i} F_{ij}, \quad (1.22)$$

where F_{ij} is the fluid flux from K_i to K_j :

$$F_{ij} = - \int_{\Gamma_{ij}} \lambda (\mathbf{k} \nabla p) \cdot \mathbf{n}_{ij} \, d\Gamma_{ij}, \quad (1.23)$$

where \mathbf{n}_{ij} is a unit vector normal to Γ_{ij} and oriented from K_i to K_j .

We now make one of the key assumptions for spatial discretization methods in reservoir simulation. We assume that in the neighborhood of the interface Γ_{ij} , the mobility λ is smooth enough to be considered constant, so that the interface flux is rewritten as

$$F_{ij} \approx -\lambda_{ij} \int_{\Gamma_{ij}} (\mathbf{k}\nabla p) \cdot \mathbf{n}_{ij} \, d\Gamma_{ij}, \quad (1.24)$$

where λ_{ij} is the average mobility at the interface Γ_{ij} . This approximation allows a decoupling of the *dynamic* data contained in λ from the *static* data included in the permeability tensor \mathbf{k} and implicitly present in the geometry of the face Γ_{ij} and in the gradient operator ∇ . We define the static part of the flux as

$$\tilde{F}_{ij} = - \int_{\Gamma_{ij}} (\mathbf{k}\nabla p) \cdot \mathbf{n}_{ij} \, d\Gamma_{ij}. \quad (1.25)$$

The total flux is then obtained from its static part through

$$F_{ij} \approx \lambda_{ij} \tilde{F}_{ij}. \quad (1.26)$$

We now focus on the computation of the static flux from a set of neighboring pressure nodes. Let us define the set Λ_{ij} of elements K_l touching the interface Γ_{ij} , i.e. $K_l \in \Lambda_{ij}$ if it shares at least a vertex with the interface Γ_{ij} . The cornerstone of finite volume methods is the approximation of \tilde{F}_{ij} from the pressure nodes of Λ_{ij} through a discretization of the pressure gradient. The resulting flux approximation expresses \tilde{F}_{ij} as a linear combination of the neighboring pressure points

$$\tilde{F}_{ij} = \sum_{K_l \in \Lambda_{ij}} T_l p_l, \quad (1.27)$$

where T_l are static transmissibility coefficients [10]. In reservoir simulation, these static coefficients are preprocessed before the full multiphase flow simulation. The total

transmissibility coefficient is then obtained by multiplying the static transmissibility by the mobility λ_{ij} . This separation of the static and dynamic part of the transmissibility allows a decoupling of the spatial discretization from the non-linearities of the flow problem.

The number of pressure points necessary to properly approximate the flux through an interface depends strongly on the grid geometry and the complexity of the permeability field. Two main methods are used: the two-point flux approximation (TPFA) only uses the upstream and downstream elements K_i and K_j , and the multipoint flux approximation (MPFA) takes into account the entire set Λ_{ij} in the flux computation.

1.3.1 Two-point flux approximation

The TPFA method is best understood in the context of one-dimensional flow. The pressure is assumed to vary linearly within each of the two control volumes sharing an interface (see **Figure 1.1**). The potential gradient is therefore taken constant in each control volume. Enforcing the pressure and flux continuity across the interface leads to an expression of the static flux:

$$\tilde{F}_{12} = T_1 p_1 + T_2 p_2, \quad (1.28)$$

where the transmissibility coefficients

$$T_1 = -T_2 = \frac{2}{\Delta x_1/k_x^1 + \Delta x_2/k_x^2} \quad (1.29)$$

verify the usual harmonic permeability average property.

For multidimensional problems, TPFA is based on a dimensional split, such that the interface transmissibilities is computed in each direction independently. This

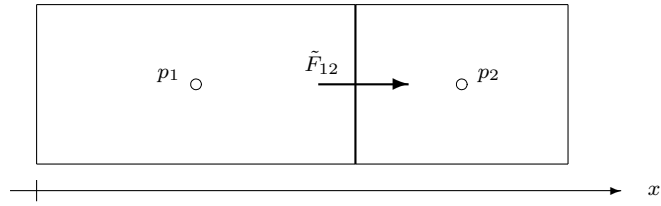


Figure 1.1. Schematic of the two-point flux approximation method for one-dimensional problems.

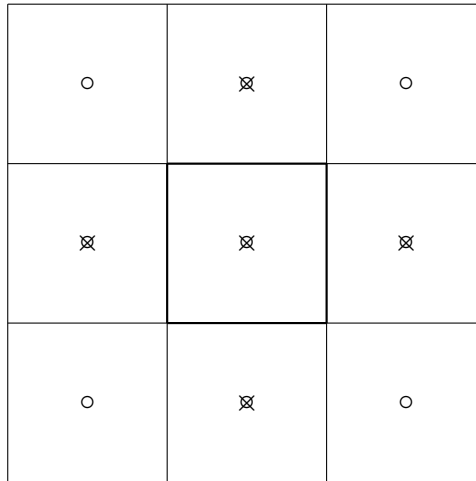


Figure 1.2. 5-point (\times) and 9-point (\circ) stencils corresponding to the TPFA and MPFA methods on a two dimensional Cartesian grid.

procedure leads to a five-point stencil in two dimensions (**Figure 1.2**) and to a seven-point stencil in three dimensions. As a matter of fact, on Cartesian grids and in the presence of diagonal permeability coefficients, TPFA is equivalent to the classical seven-point finite difference method in three dimensions [10].

TPFA represents the most widely used discretization method in reservoir simulation. However, the basic underlying assumptions of TPFA do not allow the method to represent grid distortion, or non-diagonal tensor permeabilities, properly. In such

cases, the TPFA method does not lead to a convergent discretization, and can produce $O(1)$ errors in the computations.

1.3.2 Multipoint flux approximations

MPFA methods are designed to overcome the deficiencies of TPFA for advanced simulation grids. An excellent introduction (including an extensive literature review) to MPFA discretizations is given by Aavatsmark [1].

The first derivation of these methods was presented for two-dimensional structured grids independently by Aavatsmark *et al.* [2] and Edwards and Rogers [34]. These methods have been extended to unstructured grids [3; 4; 33; 67] and three-dimensional hexahedral grids [5; 45; 46].

To simplify the presentation, we present MPFA methods on two-dimensional structured quadrilateral grids. Extensions to unstructured or three-dimensional grids are straightforward, since they rely on the same concepts as those developed for two-dimensional structured quadrilateral grids.

MPFA methods employ an extended stencil to approximate the interface static fluxes. \tilde{F}_{ij} is thus computed as in (1.27) with the pressure nodes from the entire set Λ_{ij} of gridblocks K_l touching the interface Γ_{ij} . For a structured quadrilateral grid, six pressure nodes are thus used to compute a flux (**Figure 1.3**), which leads to a nine-point stencil (**Figure 1.2**). On three-dimensional structured hexahedral grids, a 27-point stencil is used.

To compute the transmissibility coefficients of (1.27), a *dual grid* is created, staggered with the primal grid defined by the gridblocks. Each cell of the dual grid is referred to as an *interaction region* and is centered on a node of the primal grid (**Figure 1.4**). The interaction regions divide each cell into four *subcells* and each cell interface into two *subinterfaces*. The transmissibility coefficients of (1.27) are obtained by solving local problems on the interaction regions.

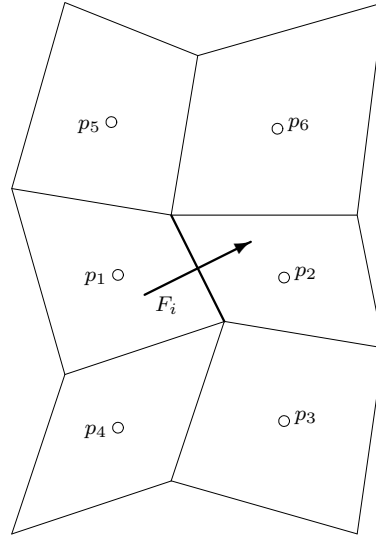


Figure 1.3. MPFA stencil for a two-dimensional structured quadrilateral grid.

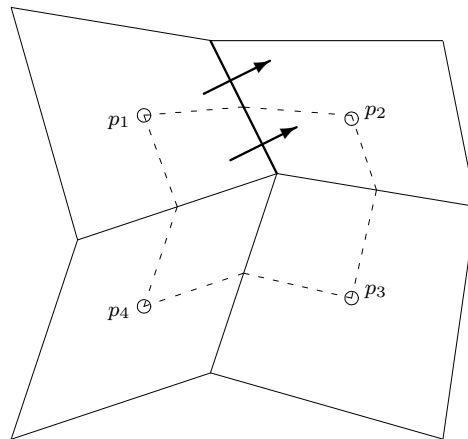


Figure 1.4. Interaction region (dashed line) for a sub-interface flux in MPFA on a two-dimensional structured quadrilateral grid.

MPFA methods are constructed to be linearly exact for general grid geometries and tensor coefficients. This means that a linear pressure variation must be represented exactly by the MPFA discretization. The local problem is defined through an approach similar to that of the one-dimensional problem, but generalized in two dimensions to assume that the pressure varies linearly within each subcell. A flux continuity condition is enforced on each subinterface to guarantee mass conservation across the interfaces. Pressure continuity can only be enforced weakly. Existing MPFA methods differ mainly in the way this weak pressure continuity is formulated. In the so-called O-method, one imposes the pressure to be continuous at the midpoint of the interface.

In two-dimensional structured grids, a linear pressure approximation in each of the four subcells leads to the definition of $3 \times 4 = 12$ degrees of freedom in the local system of an interaction region. The 12 conditions used to determine the system are: (a) four flux continuity conditions across the subinterfaces, (b) four pressure continuity conditions across the subinterfaces and (c) honoring the pressure values at the gridcell centers. On three-dimensional structured hexahedral grids, an interaction region is composed of eight subcells. Allowing the pressure to vary linearly within each subcell leads to the definition of $4 \times 8 = 32$ degrees of freedom. The system is closed with (a) flux continuity conditions across the twelve subinterfaces, (b) twelve pressure continuity conditions at the interface midpoints and (c) honoring the pressures at the centers of the eight gridcells of the interaction regions.

1.4 Streamline simulation

Streamline simulation is a fast alternative to classical reservoir simulation methods and as such, it is increasingly used in reservoir engineering applications. We here recall the main steps of the basic streamline method. For simplicity, we consider as in

Section 1.2 the case of a two-phase immiscible displacement process, with negligible capillarity and gravity forces. A more complete introduction to streamline methods can be found in [12; 28].

The streamline method relies on the fractional flow formulation that separates the pressure equation (1.14), representing the *flow* problem, from the saturation equation (1.17), governing the *transport* problem. In the absence of sources, the divergence of the total-velocity vanishes, and the transport problem can be written as

$$\phi \frac{\partial S_w}{\partial t} + \mathbf{u} \cdot \nabla \varphi_w = 0. \quad (1.30)$$

Using the identity

$$\mathbf{u} \cdot \nabla \equiv \|\mathbf{u}\| \frac{\partial}{\partial s}, \quad (1.31)$$

where s is the arc-length of a streamline, we can reformulate the saturation equation into a one-dimensional transport problem

$$\phi \frac{\partial S_w}{\partial t} + \|\mathbf{u}\| \frac{\partial \varphi_w}{\partial s} = 0. \quad (1.32)$$

Let us now introduce the time-of-flight variable τ , defined as the travel time of a fluid particle along a streamline. The time-of-flight is linked to the arc-length s and total velocity through

$$\frac{\partial \tau}{\partial s} = \frac{\phi}{\|\mathbf{u}\|}. \quad (1.33)$$

The streamline method uses the time-of-flight variable to put the transport problem in an extremely simple form:

$$\frac{\partial S_w}{\partial t} + \frac{\partial \varphi_w}{\partial \tau} = 0. \quad (1.34)$$

Instead of solving the hyperbolic transport problem on the simulation grid, where the time-step size is limited by stability conditions [27], the streamline method solves

the saturation equations as a series of unconditionally stable one-dimensional displacement problems along the flow paths (i.e. streamline coordinates).

Streamline simulation uses a sequential approach to solve the flow and the modified transport problem. First, the pressure equation is solved on the simulation grid and the streamlines are traced. Second, the transport problem is posed along the streamlines where the saturations are advected according to (1.34). The quality of the streamlines, in terms of location and time-of-flight, is therefore crucial to recover an accurate overall solution.

To trace streamlines, the velocity field within each control volume is expressed as a function of interface fluxes. The streamline is then integrated using this (reconstructed) velocity field by following the path of a fluid particle in time. This integration is usually performed to arbitrary precision, either analytically or numerically depending on the complexity of the velocity field. The real challenge in tracing accurate streamlines is the reconstruction of an accurate velocity field from the interface fluxes. This reconstruction obviously depends on the discretization used for the pressure equation and becomes a challenging problem in the presence of grid distortion and permeability tensors.

1.5 Problem statement

Conventional finite-volume and streamline-based reservoir simulation rely on MPFA methods to discretize the pressure equation on distorted grids and/or in the presence of tensor permeability coefficients. Despite the wide use of MPFA methods in the oil industry, rigorous analysis of their properties is still limited by the mathematical framework on which they rely. In this work, we place MPFA methods in the context of mixed finite element (MFE) discretizations. MFE methods have a powerful mathematical framework that is well-suited for theoretical analysis of discretization

problems. On two-dimensional triangles and quadrilaterals and on three-dimensional tetrahedra, a link between MPFA and MFE method has been established recently [70], but this correspondence does not exist on hexahedra. We present a new MFE method on hexahedra that reduces into an MPFA method thus providing the missing link.

In light of this new MFE method, the question of the convergence of MPFA methods on hexahedral grids is addressed in this work. Hexahedral grids form the majority of the reservoir simulation models and TPFA methods are known to yield non-convergent discretizations on such grids in the presence of grid distortion or permeability tensors. Although the convergence of MPFA has been observed numerically [6], a proof has remained elusive. We here provide, for the first time, an error analysis that establishes mathematically the convergence of MPFA on rectangular hexahedra and provides theoretical error estimates confirmed by numerical experiments.

We further exploit the MFE framework to tackle the problem of tracing accurate streamlines when MPFA is used to discretize the pressure equation. The reliability of streamline simulations relies heavily on the quality of the streamlines used to solve the transport problem. We revisit the problem of streamline tracing by relying on the MFE framework. A theoretical justification for the low-order streamline tracing methods currently in use [26; 60] is provided, and high-order methods adapted to MPFA discretizations are outlined.

1.6 Thesis overview

Chapter 2 is an introduction to mixed finite-element methods applied to the solution of the elliptic pressure equation. These methods use a finite-element approach to solve the mixed variational form of the flow problem, in which the unknowns are both the pressure and velocity fields. Just as finite-volume methods use two- or

multiple pressure points to obtain a flux description, MFE discretizations can involve velocity fields of different accuracy. The choice of velocity fields is, however, limited by compatibility conditions between the pressure and the velocity spaces. When a single pressure unknown per element is used, which is of primary interest for finite-volume schemes, two velocity fields can be chosen: the Raviart-Thomas-Nédélec [58; 63] and the Brezzi-Douglas-Marini [15; 16] velocities that we present at the end of the chapter.

These two velocity spaces do not allow a link to be established between MPFA and MFE methods on hexahedra. We therefore devote Chapter 3 to the presentation of a new velocity space on hexahedra that allows MPFA methods to be placed in the context of MFE methods. In Chapter 3, we also present the link between the MFE and FV method that relies on an inexact numerical quadrature. The chapter is concluded by comparing numerically the performance of the various discretizations in terms of accuracy and monotonicity.

Chapter 4 is focused on mathematical analysis of both the new MFE method and its localized form into MPFA. In particular, we establish that the new velocity space induces the Babuška-Brezzi condition, when combined with a piecewise constant pressure description. The MFE method is shown to be convergent, and we provide error estimates for the pressure and velocity fields. We then proceed to error analysis of MPFA and establish its convergence on rectangular hexahedral grids in the presence of full-tensor permeabilities. Optimal error estimates for MPFA are provided and confirmed by a numerical convergence study.

Chapter 5 presents application of the links between MFE and MPFA methods to streamline simulation. The problem of tracing streamlines from either MFE or FV discretizations is revisited. A streamline tracing algorithm is developed for MFE methods. Using the links between MFE and FV discretizations, we justify using the new tracing algorithm for MPFA methods. The algorithm obtained is the natural extension of Pollock's [60] tracing method for general tetrahedral or hexahedral grids.

The new method presents two major advantages over the streamline tracing algorithm developed for MPFA by Prévost [61] and Hægland *et al.* [38]. First, our algorithm provides more accurate streamlines and second, our approach does not require an expensive flux postprocessing, such as that used by the other methods. Numerical experiments are performed to test the accuracy and robustness of the streamline tracing algorithm.

Chapter 2

Mixed finite element methods

This chapter serves as an introduction to mixed finite element methods. Although this content is not new, it is reminded for the sake of completeness since the concepts introduced here will be heavily used in the following chapters.

We start by describing the mixed variational formulation of the elliptic pressure equation. We then present the mixed finite element discretization and the solution of its system. We finish the chapter by a review of known velocity spaces compatible with a piecewise constant pressure space.

2.1 The mixed variational formulation

Mixed finite element (MFE) methods represent a finite-element approach to the discretization of the flow problem. The term *mixed* indicates that MFE methods solve simultaneously for both the pressure and velocity fields.

MFE methods discretize the mixed variational form of the elliptic pressure equations of (1.5) or (1.14). The problem is written in mixed form as

$$\mathbf{k}^{-1}\mathbf{u} + \nabla p = 0 \quad \text{in } \Omega \subset \mathbb{R}^d, \quad (2.1)$$

$$\nabla \cdot \mathbf{u} = f \quad \text{in } \Omega \subset \mathbb{R}^d, \quad (2.2)$$

where $d = 2, 3$ is the space dimension. (2.1) and (2.2) represent Darcy's law and the mass balance equation, respectively. Once again, \mathbf{u} is the volumetric velocity, p is the pressure, f is a source term, and \mathbf{k} is the permeability tensor. We here recall that the permeability tensor must be symmetric positive definite, which ensures the existence of \mathbf{k}^{-1} . Its components must be bounded but may be highly discontinuous and display large anisotropy ratios. The governing equations are supplemented with the following boundary conditions:

$$p = \bar{p} \quad \text{on } \Gamma_D, \quad (2.3)$$

$$\mathbf{u} \cdot \mathbf{n} = 0 \quad \text{on } \Gamma_N, \quad (2.4)$$

where Γ_D and Γ_N are respectively the Dirichlet and Neumann partitions of the domain boundary $\partial\Omega$ such that $\Gamma_D \cap \Gamma_N = \emptyset$, $\Gamma_D \cup \Gamma_N = \partial\Omega$. \mathbf{n} is the outward unit normal to $\partial\Omega$.

Let $W \equiv L^2(\Omega)$ be the Sobolev space of square integrable functions in $\Omega \subset \mathbb{R}^d$, with the usual inner product (\cdot, \cdot) and norm $\|\cdot\|_{L^2(\Omega)} = (\cdot, \cdot)^{1/2}$. We introduce the space

$$\mathbf{V} \equiv \mathbf{H}_{0,N}(\text{div}, \Omega) = \{\mathbf{v} : \mathbf{v} \in \mathbf{H}(\text{div}, \Omega), \mathbf{v} \cdot \mathbf{n} = 0 \text{ on } \Gamma_N\} \quad (2.5)$$

of functions in $\mathbf{H}(\text{div}, \Omega)$ with null normal trace on the Neumann boundary Γ_N ,

where the space

$$\mathbf{H}(\operatorname{div}, \Omega) = \{ \mathbf{v} : \mathbf{v} \in (L^2(\Omega))^d, \nabla \cdot \mathbf{v} \in L^2(\Omega) \} \quad (2.6)$$

is equipped with the norm:

$$\| \mathbf{v} \|_{\mathbf{H}(\operatorname{div}, \Omega)} = (\| \mathbf{v} \|^2 + \| \nabla \cdot \mathbf{v} \|^2)^{1/2}. \quad (2.7)$$

The space $\mathbf{H}(\operatorname{div}, \Omega)$ is defined such that a vector \mathbf{v} belonging to this space admits a well-defined normal trace on $\partial\Omega$ [17]:

$$\bar{v} \equiv \mathbf{v} \cdot \mathbf{n} \in H^{-1/2}(\partial\Omega). \quad (2.8)$$

Denoting by $H^{1/2}(\Gamma)$ the dual space of $H^{-1/2}(\Gamma)$ for $\Gamma \subset \partial\Omega$, we also define the duality product:

$$\langle \bar{u}, \bar{p} \rangle_{\Gamma} = \int_{\Gamma} \bar{u} \bar{p} \, d\Gamma, \quad \bar{u} \in H^{-1/2}(\Gamma), \bar{p} \in H^{1/2}(\Gamma). \quad (2.9)$$

Making use of the functional spaces defined above, we can express the problem given by Equations (2.1)–(2.2) with boundary conditions (2.3)–(2.4) in its mixed variational form:

Find $(\mathbf{u}, p) \in \mathbf{V} \times W$ *such that*

$$(\mathbf{v}, \mathbf{k}^{-1} \mathbf{u}) - (\nabla \cdot \mathbf{v}, p) = -\langle \mathbf{v} \cdot \mathbf{n}, \bar{p} \rangle_{\Gamma_D} \quad \forall \mathbf{v} \in \mathbf{V}, \quad (2.10)$$

$$(q, \nabla \cdot \mathbf{u}) = (q, f) \quad \forall q \in W. \quad (2.11)$$

It is well known that this problem has a unique solution [17].

2.2 Discretization

The mixed variational formulation provides the basis for the mixed finite element method. MFE methods approximate the pressure and velocity fields simultaneously. Let $\mathbf{V}_h \subset \mathbf{V}$, and $W_h \subset W$ be finite dimensional subspaces of the corresponding continuum spaces, the mixed finite element approximation of (2.10)–(2.11) reads:

Find $(\mathbf{u}_h, p_h) \in \mathbf{V}_h \times W_h$ such that

$$(\mathbf{v}_h, \mathbf{k}^{-1}\mathbf{u}_h) - (\nabla \cdot \mathbf{v}_h, p_h) = -\langle \mathbf{v}_h \cdot \mathbf{n}, \bar{p} \rangle_{\Gamma_D} \quad \forall \mathbf{v}_h \in \mathbf{V}_h, \quad (2.12)$$

$$(q_h, \nabla \cdot \mathbf{u}_h) = (q_h, f) \quad \forall q_h \in W_h. \quad (2.13)$$

For the MFE method to be consistent and convergent, the spaces \mathbf{V}_h and W_h cannot be chosen independently; they must satisfy a standard coercivity condition and the discrete inf-sup condition [11; 13; 14; 17].

The global spaces \mathbf{V}_h and W_h are constructed by means of: (1) a partition \mathcal{T}_h of the domain Ω into nonoverlapping elements $\{K\}$ (in this thesis, we restrict our attention to triangular, quadrilateral, tetrahedral or hexahedral elements); and (2) polynomial spaces defined locally, on a reference element \hat{K} . Examples of successful mixed finite element spaces are those of Raviart–Thomas [63] or Brezzi–Douglas–Marini [16] on 2D triangular and quadrilateral elements and those of Nedelec [58], and Brezzi–Douglas–Duran–Fortin [15] on 3D tetrahedral or hexahedral grids.

Let $\mathbf{N}_1^u, \dots, \mathbf{N}_{n_u}^u$ and $N_1^p, \dots, N_{n_p}^p$ form two bases for the velocity and pressure spaces \mathbf{V}_h and W_h , respectively. The velocity and pressure solutions to the mixed finite element problem of (2.12)–(2.13) are expressed as linear combinations of basis

functions, \mathbf{N}_i^u , N_j^p and corresponding velocity and pressure components U_i , P_j :

$$\mathbf{u}_h = \sum_{i=1}^{n_u} U_i \mathbf{N}_i^u, \quad (2.14)$$

$$p_h = \sum_{j=1}^{n_p} P_j N_j^p. \quad (2.15)$$

The velocity unknowns U_i are defined as fluxes across element edges (2D) or faces (3D). The pressure unknowns P_j are defined as element pressures. The above discretization yields an indefinite linear system of the form

$$\begin{pmatrix} \mathbf{A} & -\mathbf{B}^t \\ \mathbf{B} & \mathbf{0} \end{pmatrix} \begin{pmatrix} \mathbf{u} \\ \mathbf{p} \end{pmatrix} = \begin{pmatrix} \mathbf{R}^u \\ \mathbf{R}^p \end{pmatrix} \quad (2.16)$$

where \mathbf{u} and \mathbf{p} are the vectors of flux and pressure unknowns, \mathbf{A} is a square matrix of size $n_u \times n_u$ and \mathbf{B} is a matrix of size $n_p \times n_u$:

$$A_{il} = (\mathbf{N}_i^u, \mathbf{k}^{-1} \mathbf{N}_l^u), \quad (2.17)$$

$$B_{jl} = (N_j^p, \nabla \cdot \mathbf{N}_l^u), \quad (2.18)$$

and \mathbf{R}^u and \mathbf{R}^p are the right-hand side vectors of the Darcy and mass balance equations:

$$R_i^u = -\langle \mathbf{N}_i^u \cdot \mathbf{n}, \bar{p} \rangle_{\Gamma_D}, \quad (2.19)$$

$$R_j^p = (N_j^p, f). \quad (2.20)$$

2.3 Numerical integration

The construction of the MFE matrix requires evaluation of the integrals of (2.17)–(2.18). The integrals are usually evaluated numerically by quadrature rules [39] because an analytical integration is often challenging and sometimes impossible.

A quadrature rule is a set of n_{integ} weights w_k and points \mathbf{x}_k ($k = 1, \dots, n_{\text{integ}}$) defining a numerical approximation of an integral:

$$\int_{\Omega} h(\mathbf{x}) d\Omega = \sum_{k=1}^{n_{\text{integ}}} w_k h(\mathbf{x}_k) + R \approx \sum_{k=1}^{n_{\text{integ}}} w_k h(\mathbf{x}_k) \quad (2.21)$$

where R is the remainder, or error, committed by the quadrature rule in its approximation of the integral. This error depends on the number and location of the points involved in the quadrature and on the complexity of the integrand $h(\mathbf{x})$.

Sometimes, the numerical quadrature used for the integration of the MFE system is not exact. This *reduced integration* approach can have two known effects on the MFE system: localization [52; 53; 70] and stabilization [50].

2.4 Solution of the MFE system

The MFE system of (2.16) is nonsingular under the inf-sup condition, but its indefinite character requires special numerical solution techniques [22]. We use an augmented Lagrangian method, known as Uzawa’s algorithm [22; 35] to solve the system (2.16). Alternatively, one may hybridize the system and solve a symmetric, positive definite system for the traces of the pressure at the element edges [17]. A third option is to eliminate the velocity unknowns from the MFE system. Because MFE methods are locally conservative at the element level, each element can be viewed as a control volume on which a mass balance condition is enforced. The MFE system of Equation

(2.16) is thus rewritten as a finite volume method:

$$\mathbf{C} \mathbf{p} = \mathbf{R}, \quad (2.22)$$

where \mathbf{C} is a matrix of size $n_p \times n_p$ given by

$$\mathbf{C} = \mathbf{B} \mathbf{A}^{-1} \mathbf{B}^t, \quad (2.23)$$

and \mathbf{R} is the right-hand side vector:

$$\mathbf{R} = \mathbf{R}^p - (\mathbf{B} \mathbf{A}^{-1}) \mathbf{R}^u. \quad (2.24)$$

In general, the matrix \mathbf{C} is a *full* matrix. This means that the pressure of a given element depends on all pressure nodes of the grid.

In some cases, a reduced integration approach can be used to *localize* the MFE stencil and yield a sparse finite-volume system. The inexact quadrature restricts the interactions between velocity degrees of freedom, which leads to a sparse matrix \mathbf{A} . In some cases, reviewed in Section 3.1, this gives sparse matrices \mathbf{A}^{-1} and \mathbf{C} .

2.5 The reference element

2.5.1 Coordinate mapping

In mixed finite element methods, the global spaces \mathbf{V}_h and W_h are constructed from spaces defined locally, on a reference element \hat{K} . The reference element \hat{K} is linked to any given element K in the physical space by a mapping, or change of coordinates φ

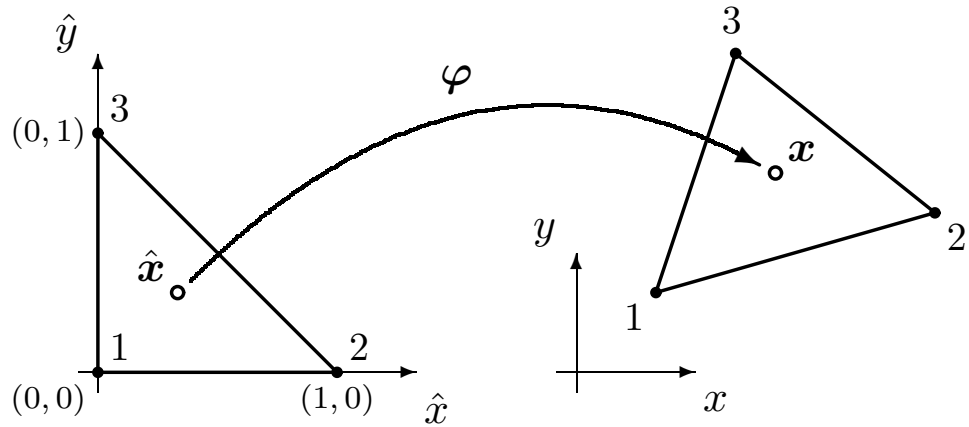


Figure 2.1. Mapping of triangular elements.

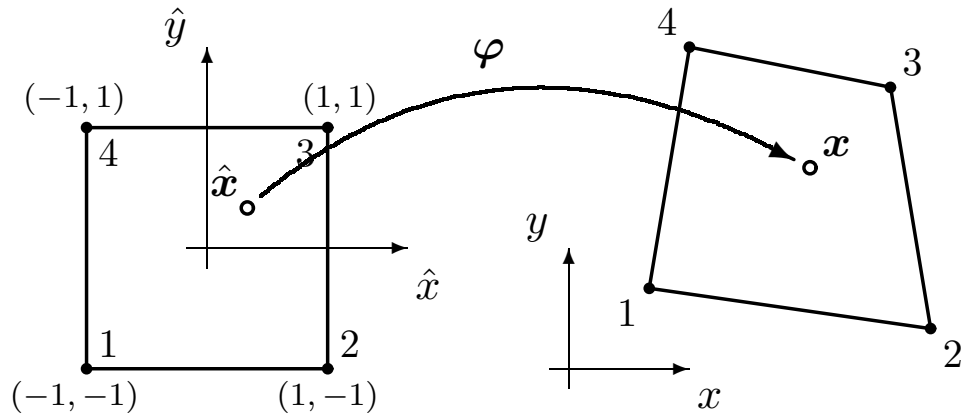


Figure 2.2. Mapping of quadrilateral elements.

defined by:

$$\begin{aligned} \varphi : \mathbb{R}^d &\longrightarrow \mathbb{R}^d \\ \hat{\mathbf{x}} \in \hat{K} &\mapsto \mathbf{x} = \varphi(\hat{\mathbf{x}}) \in K. \end{aligned} \tag{2.25}$$

This mapping must be smooth and invertible for all elements. This ensures that, for any $\hat{\mathbf{x}} \in \hat{K}$, the Jacobian matrix $\mathbf{D}(\hat{\mathbf{x}}) = \partial\varphi/\partial\hat{\mathbf{x}}$ of the transformation is invertible, and that its determinant $J(\hat{\mathbf{x}}) = \det \mathbf{D}(\hat{\mathbf{x}})$ is bounded away from zero.

The map φ from the reference triangle, square, tetrahedron and cube to the

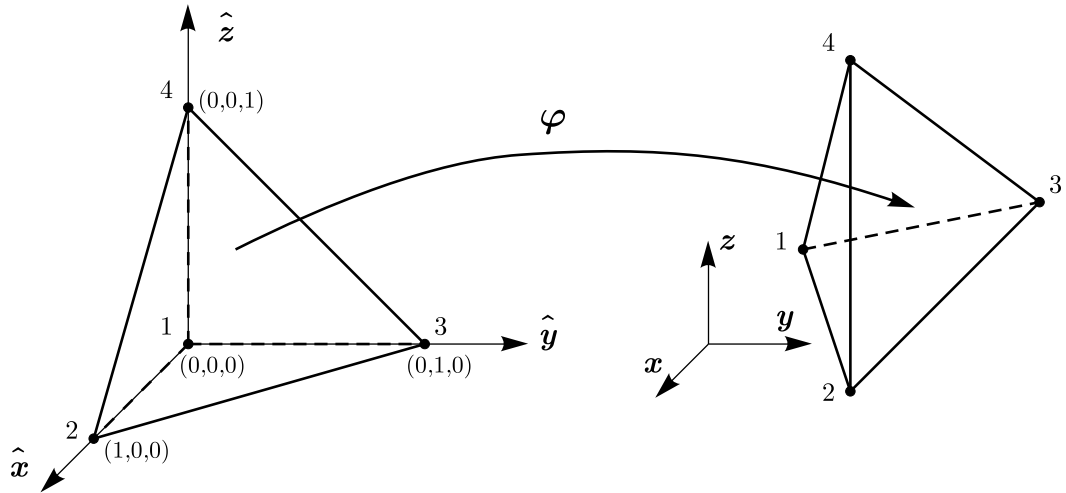


Figure 2.3. Mapping of tetrahedral elements.

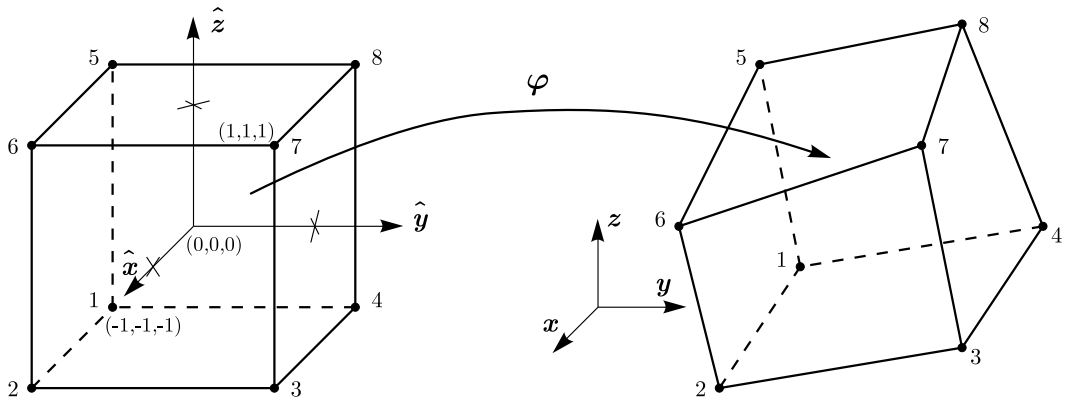


Figure 2.4. Mapping of hexahedral elements.

physical space is shown respectively in **Figures 2.1–2.4**. The mapping φ is given by:

$$\mathbf{x} = \varphi(\hat{\mathbf{x}}) = \sum_{a=1}^{n_{\text{node}}} N_a(\hat{\mathbf{x}}) \mathbf{x}_a, \quad (2.26)$$

where \mathbf{x}_a are the nodal coordinates of the element in physical space, and N_a are the usual finite element hat functions in reference space [39].

2.5.2 The Piola transform

In addition to the mapping of the coordinates $\boldsymbol{\varphi}$, we use $\mathbf{D}(\hat{\boldsymbol{x}})$ and its determinant $J(\hat{\boldsymbol{x}})$, to define the Piola transform as the mapping of the velocity field from the reference space to the physical space [17; 48; 66]:

$$\mathbf{v}(\boldsymbol{x}) = \mathcal{P}(\hat{\mathbf{v}})(\boldsymbol{x}) = \frac{1}{J(\hat{\boldsymbol{x}})} \mathbf{D}(\hat{\boldsymbol{x}}) \hat{\mathbf{v}}(\hat{\boldsymbol{x}}), \quad (2.27)$$

with $\boldsymbol{x} = \boldsymbol{\varphi}(\hat{\boldsymbol{x}})$. The essential property of the mapping \mathcal{P} is that it preserves the normal trace of the vector field. In our context, this means that the fluxes through element faces in the reference and physical spaces are equal.

2.6 Velocity spaces

2.6.1 Compatible mixed finite elements

One of the essential features of the mixed finite element discretization described above is that the pressure and velocity spaces cannot be chosen independently of each other. To render a consistent approximation, they must satisfy two conditions [13; 17]: a standard coercivity condition, and the discrete inf-sup condition [11; 14].

To provide a link to finite-volume methods, we restrict our attention to discretizations involving a single pressure unknown per element. Thus, the pressure is constant over each control volume, and the corresponding basis function is simply equal to one inside an element, and zero elsewhere. The unknowns are the cell-centered pressures and, clearly, the number of pressure unknowns is equal to the number of elements ($n_p = n_{\text{elem}}$).

The Babuška–Brezzi condition [11; 14] limits the choice of velocity spaces compatible with a piecewise constant pressure field severely. In particular, the inf-sup condition

requires that the divergence of the discrete velocity field belongs to the pressure space. For our purpose, this means that only velocity fields of constant divergence can be used. Two known velocity spaces verify this necessary condition: the lowest-order Raviart–Thomas–Nédélec space and the first order Brezzi–Douglas–Marini space.

2.6.2 The lowest-order Raviart–Thomas–Nédélec space

The simplest polynomial subspace conforming in $H(\text{div}, \hat{K})$ is the lowest-order Raviart–Thomas–Nédélec space, RTN_0 developed in two dimensions by Raviart and Thomas [63] and later extended to three dimensional elements by Nédélec [58]. Velocity fields in RTN_0 are described by a constant normal trace on element faces. Knowledge of the fluxes across each faces of an element is therefore sufficient to fully describe the RTN_0 velocity field. Thus, three degrees of freedom are needed to fully characterize RTN_0 on triangles, four on quadrilaterals and tetrahedra, and six on hexahedra.

To describe an RTN_0 velocity field, a single shape function per face is needed. The velocity shape function associated with a face is a vector field that has a unit outward flux across that face and a normal trace identically equal to zero on all other faces. **Figures 2.5–2.6** present respectively the two-dimensional and three-dimensional RTN_0 shape function associated with one of the faces of each reference element.

We now recall the form of the RTN_0 velocity fields on the various reference elements. On *simplices*, which are triangular and tetrahedral elements, the RTN_0 velocity field is characterized by a constant component in each direction plus a constant divergence term. This gives

$$\hat{\mathbf{u}}(\hat{\mathbf{x}}) = \begin{pmatrix} a_1 + b\hat{x} \\ a_2 + b\hat{y} \end{pmatrix}, \quad (a_1, a_2, b) \in \mathbb{R}^3, \quad (2.28)$$

for triangles and

$$\hat{\mathbf{u}}(\hat{\mathbf{x}}) = \begin{pmatrix} a_1 + b\hat{x} \\ a_2 + b\hat{y} \\ a_3 + b\hat{z} \end{pmatrix}, \quad (a_1, a_2, a_3, b) \in \mathbb{R}^4 \quad (2.29)$$

on tetrahedra.

On *bilinear* and *trilinear* elements, (quadrilaterals and hexahedra), each velocity component varies linearly with respect to its own coordinate. In two dimensions,

$$\hat{\mathbf{u}}(\hat{\mathbf{x}}) = \begin{pmatrix} a_1 + b_1\hat{x} \\ a_2 + b_2\hat{y} \end{pmatrix}, \quad (a_1, a_2, b_1, b_2) \in \mathbb{R}^4, \quad (2.30)$$

for quadrilaterals and on three-dimensional hexahedra,

$$\hat{\mathbf{u}}(\hat{\mathbf{x}}) = \begin{pmatrix} a_1 + b_1\hat{x} \\ a_2 + b_2\hat{y} \\ a_3 + b_3\hat{z} \end{pmatrix}, \quad (a_1, a_2, a_3, b_1, b_2, b_3) \in \mathbb{R}^6. \quad (2.31)$$

2.6.3 The first-order Brezzi–Douglas–Marini space

The Brezzi–Douglas–Marini space of order one, $\text{BDM}_1(\hat{K})$, defines a velocity field with normal traces varying linearly on each element face. The space was created for two-dimensional elements by Brezzi, Douglas and Marini [16] and later extended to three-dimensional elements by [15]. $\text{BDM}_1(\hat{K})$ is of higher order than $\text{RTN}_0(\hat{K})$, but it is constructed in such a way that it remains compatible with a piecewise constant pressure field and it is conforming in $H(\text{div}, \Omega)$.

In two dimensions, two degrees of freedom per edge are necessary to fully describe a BDM_1 velocity field. This leads to a space of dimension six for triangles and eight for

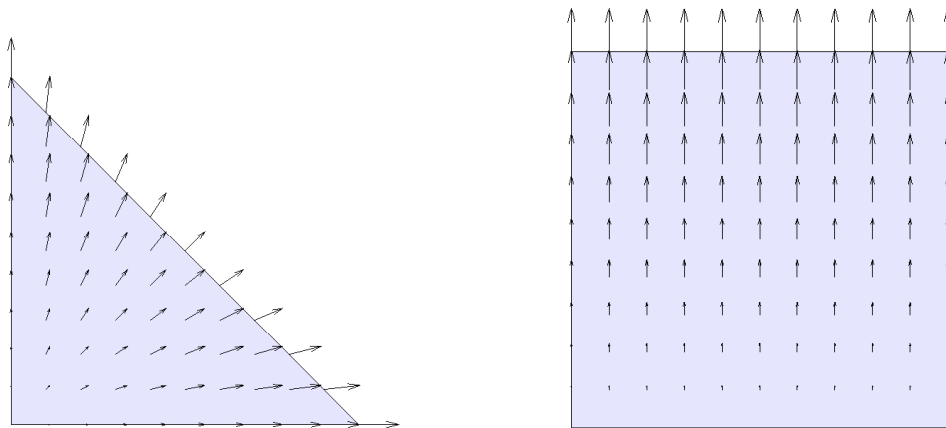


Figure 2.5. Two-dimensional RTN_0 shape functions for the top edge of the reference triangle (left) and quadrilateral (right).

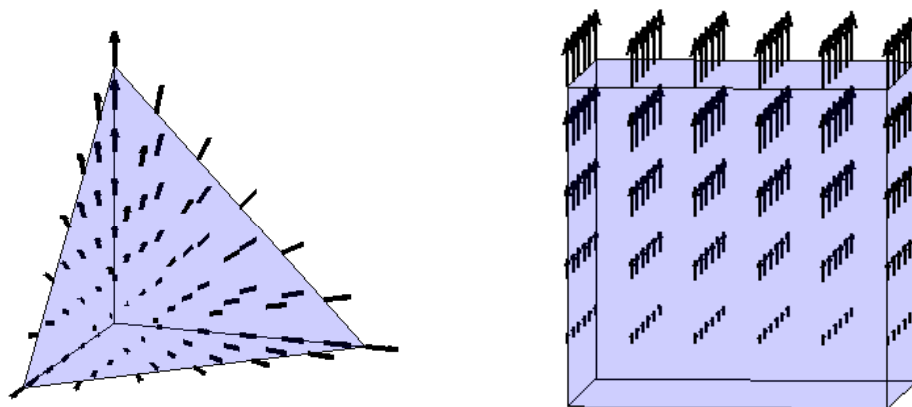


Figure 2.6. Three-dimensional RTN_0 shape functions for the top face of the reference tetrahedron (left) and hexahedron (right).

quadrilaterals. In three dimensions, three degrees of freedom per face are necessary and the dimensionality reaches 12 for tetrahedra and 18 for hexahedra.

On simplices, BDM_1 is simply the space of linear polynomials in d -dimensions:

$$\text{BDM}_1 = (P_1(\hat{K}))^d, \quad (2.32)$$

such that on triangles,

$$\hat{\mathbf{u}}(\hat{\mathbf{x}}) = \begin{pmatrix} a_1 + b_1\hat{x} + c_1\hat{y} \\ a_2 + b_2\hat{x} + c_2\hat{y} \end{pmatrix}, \quad (2.33)$$

with $(a_1, \dots, c_2) \in \mathbb{R}^6$, and on tetrahedra,

$$\hat{\mathbf{u}}(\hat{\mathbf{x}}) = \begin{pmatrix} a_1 + b_1\hat{x} + c_1\hat{y} + d_1\hat{z} \\ a_2 + b_2\hat{x} + c_2\hat{y} + d_2\hat{z} \\ a_3 + b_3\hat{x} + c_3\hat{y} + d_3\hat{z} \end{pmatrix}, \quad (2.34)$$

with $(a_1, \dots, d_3) \in \mathbb{R}^{12}$.

On the reference quadrilateral, the space is defined through

$$\text{BDM}_1(\hat{K}) = (P_1(\hat{K}))^2 + r \mathbf{curl}(\hat{x}^2\hat{y}) + s \mathbf{curl}(\hat{x}\hat{y}^2), \quad (2.35)$$

which gives velocity fields of the form:

$$\hat{\mathbf{u}}(\hat{\mathbf{x}}) = \begin{pmatrix} a_1 + b_1\hat{x} + c_1\hat{y} - r\hat{x}^2 - 2s\hat{x}\hat{y} \\ a_2 + b_2\hat{x} + c_2\hat{y} + 2r\hat{x}\hat{y} + s\hat{y}^2 \end{pmatrix}, \quad (2.36)$$

with the parameters $(a_1, \dots, s) \in \mathbb{R}^8$.

On the reference hexahedron, $\text{BDM}_1(\hat{K})$ is defined through:

$$\text{BDM}_1(\hat{K}) = (P_1(\hat{K}))^3 + \left\{ \sum_{i=1}^6 r_i \mathbf{curl}(\boldsymbol{\chi}_i) \right\}, \quad (2.37)$$

where $(r_1, \dots, r_6) \in \mathbb{R}^6$. The vector functions $\boldsymbol{\chi}_i$ are given by

$$\begin{aligned} \boldsymbol{\chi}_1 &= \begin{pmatrix} 0 \\ 0 \\ \hat{x}\hat{y}\hat{z} \\ \hat{y}\hat{z}^2 \\ 0 \\ 0 \end{pmatrix}, & \boldsymbol{\chi}_2 &= \begin{pmatrix} 0 \\ 0 \\ \hat{x}\hat{y}^2 \\ 0 \\ \hat{x}\hat{y}\hat{z} \\ 0 \end{pmatrix}, & \boldsymbol{\chi}_3 &= \begin{pmatrix} \hat{x}\hat{y}\hat{z} \\ 0 \\ 0 \\ 0 \\ \hat{x}^2\hat{z} \\ 0 \end{pmatrix}, \\ \boldsymbol{\chi}_4 &= \begin{pmatrix} 0 \\ 0 \\ \hat{x}\hat{y}\hat{z} \\ \hat{y}\hat{z}^2 \\ 0 \\ 0 \end{pmatrix}, & \boldsymbol{\chi}_5 &= \begin{pmatrix} 0 \\ 0 \\ \hat{x}\hat{y}^2 \\ 0 \\ \hat{x}\hat{y}\hat{z} \\ 0 \end{pmatrix}, & \boldsymbol{\chi}_6 &= \begin{pmatrix} \hat{x}\hat{y}\hat{z} \\ 0 \\ 0 \\ 0 \\ \hat{x}^2\hat{z} \\ 0 \end{pmatrix}, \end{aligned} \quad (2.38)$$

so that BDM_1 velocity fields take the form

$$\hat{\mathbf{u}}(\hat{\mathbf{x}}) = \begin{pmatrix} a_1 + b_1\hat{x} + c_1\hat{y} + d_1\hat{z} + (2r_2 - r_5)\hat{x}\hat{y} + r_1\hat{x}\hat{z} - r_6\hat{x}^2 \\ a_2 + b_2\hat{x} + c_2\hat{y} + d_2\hat{z} + (2r_4 - r_1)\hat{y}\hat{z} + r_3\hat{x}\hat{y} - r_2\hat{y}^2 \\ a_3 + b_3\hat{x} + c_3\hat{y} + d_3\hat{z} + (2r_6 - r_3)\hat{x}\hat{z} + r_5\hat{y}\hat{z} - r_4\hat{z}^2 \end{pmatrix}, \quad (2.39)$$

with the parameters $(a_1, \dots, r_6) \in \mathbb{R}^{18}$.

On quadrilaterals and hexahedra, the BDM_1 spaces have more degrees of freedom than the space of first-order polynomials. A naive construction of these spaces using higher-order polynomials leads to velocity fields with non-constant divergence. The MFE so-defined does not verify the inf-sup condition [11; 14] (see for example, the attempt by Nédélec [59]). As presented in (2.35) or (2.37), BDM_1 velocities are based on the space of linear polynomials enriched by \mathbf{curl} terms. These terms add linearly varying normal components on each face, while maintaining a constant velocity divergence. This enriches the velocity space with higher order terms, while maintaining

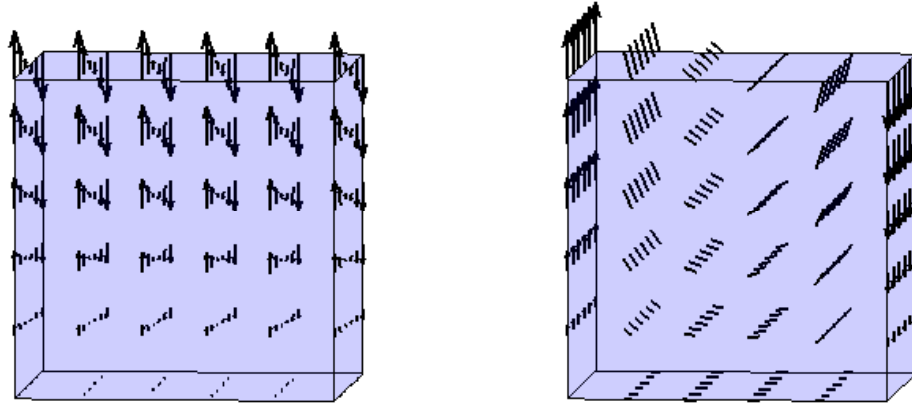


Figure 2.7. The two BDM_1 recirculation shape functions for the top face of the reference hexahedron.

its compatibility with a constant pressure space.

The degrees of freedom of BDM_1 are the moments of order zero and one on each face. We use the RTN_0 shape functions to describe the net fluxes through the element faces, that is, the moments of order zero. *Recirculation* shape functions are then added to the set of RTN_0 shape functions to describe the linear variation of the normal components across faces.

Thus, one recirculation shape function is associated with each face in two dimensions and two per face in three dimensions. They have a zero net flux through any of the faces, but describe a linearly varying normal trace along one of the main directions of the face. As an illustration, **Figure 2.7** shows plots of the RTN_0 and the two recirculation shape functions associated with the top face of the reference hexahedral element.

Chapter 3

MPFA as a new MFE method

In this chapter, we introduce MJT, a new velocity space on hexahedra. This space is defined by four flux degrees of freedom per face. Postponing the analysis of the induced MFE method to the next chapter, we introduce the trapezoidal quadrature rule that localizes the MFE method into an MPFA finite volume discretization. The various discretizations are tested at the end of the chapter by challenging numerical experiments.

3.1 Relationship between FV and MFE methods

Despite the wide use of MPFA methods in the oil industry, their analysis is still relatively limited by the mathematical framework on which they rely. The study of finite volume discretizations is often easier in the context of finite element methods. Therefore, much research has been devoted to establishing relationships between finite volume and finite element methods [7; 42–44; 68; 71].

In their seminal work, Russell and Wheeler [64] established the equivalence between traditional finite differences and certain mixed finite elements (the lowest order Raviart–Thomas space, RT_0 [63]) with quadrature (a midpoint-trapezoidal rule).

Analysis of the method, including superconvergence results, followed in [69]. Arbogast et al. [8; 9] extended that work to full-tensor coefficients in 3D. They used an expanded mixed method (also based on the lowest-order Raviart–Thomas–Nedelec space, RTN_0 [58; 63]), where they discretized the scalar, its gradient, and the vector variable. This approach leads to a 9-point stencil in 2D and a 19-point stencil in 3D. Unfortunately, these discretization schemes may be associated with severe loss of accuracy in the presence of discontinuous coefficients. In a recent paper, Chen and Yu [24] obtain a cell-centered finite-difference method with a 19-point stencil using the BDDF_1 space [15] and certain quadrature rules. They do not provide, however, a link to MPFA methods.

Higher-order finite-volume methods on rectangles derived from mixed finite elements with quadrature have been developed and analyzed in [19]. These high-order methods are not cell-centered schemes. Klausen and Winther [43; 44] proved convergence of the MPFA O-method in 2D by means of a broken RT_0 space.

Recently, the link between the Brezzi–Douglas–Marini mixed finite element method of order one and MPFA has been established in the context of numerical discretization [70] and streamline simulation [49; 54; 55] [55]. Wheeler and Yotov [70] used the BDM_1 space [15; 16] and numerical quadrature for proving convergence of MPFA on two-dimensional triangles and quadrilaterals and three-dimensional tetrahedra. Three-dimensional hexahedral elements were not considered.

The underlying reason for the difficulty in extending this approach to hexahedra is obtaining a vector space conforming in $H(\text{div})$ that localizes to a finite volume method under appropriate quadrature. To localize the MFE into an MPFA, the velocity space needs to be defined by vertex-based shape functions. Therefore, the number of unknowns defining the velocity field on a face needs to be equal to the number of face vertices. On two dimensional triangular, or quadrilateral grids, an element edge is defined by two vertices. The space BDM_1 , defined by two shape functions

per edge, can thus be localized into an MPFA. On three dimensional tetrahedra, three vertices are necessary to define the triangular faces. The extension of BDM_1 to three dimensions [15] is defined using three degrees of freedom per face, which allows the corresponding MFE method to be reduced to an MPFA by the trapezoidal quadrature.

BDM_1 cannot, however, be localized by this approach on hexahedra. In this chapter, we present a new vector space, MJT, defined on the reference hexahedron that is conforming in $H(\text{div})$, and that has four degrees of freedom per face [52; 53]. The construction of the new space is similar to that of the BDM class of spaces [15; 16] (enrichment of the space of linear polynomials by divergence-free polynomials of higher degree), but *does not* contain the space BDM_1 .

This chapter is focused on the introduction of the MJT space and on the presentation of its localization into an MPFA discretization. The consistency and convergence analyses of both the new MFE and the MPFA methods are given in next chapter.

3.2 A new mixed finite element

In this section, we present the new mixed finite element. The key requirement on the velocity space is that it allows for localization into a cell-centered finite volume method. For this, we need different degrees of freedom from those of existing spaces (like RTN [58; 63] or BDM [15; 16]). We design a space that is conforming in $\mathbf{H}(\text{div})$ and that has *four* degrees of freedom on each quadrilateral face of the hexahedral element.

We define our MFE on the reference hexahedron element $\hat{K} = [-1, 1]^3$. Although the velocity space can be used with general hexahedra in physical space, we restrict our analysis to grids formed of rectangular parallelepipeds K of size $h_x \times h_y \times h_z$. The mapping $\mathbf{x} = \boldsymbol{\varphi}(\hat{\mathbf{x}})$ from reference to physical space is therefore affine, with a

constant, diagonal Jacobian matrix:

$$\mathbf{D} = \frac{\partial \boldsymbol{\varphi}(\hat{\boldsymbol{x}})}{\partial \hat{\boldsymbol{x}}} = \begin{pmatrix} h_x/2 & 0 & 0 \\ 0 & h_y/2 & 0 \\ 0 & 0 & h_z/2 \end{pmatrix}, \quad \det \mathbf{D} = \frac{h_x h_y h_z}{8}. \quad (3.1)$$

The mapping of a scalar field is simply:

$$q(\boldsymbol{x}) = \hat{q}(\hat{\boldsymbol{x}}). \quad (3.2)$$

A vector function $\hat{\boldsymbol{v}}(\hat{\boldsymbol{x}}) \in (L^2(\hat{K}))^3$ is mapped according to the Piola transform [17]:

$$\boldsymbol{v}(\boldsymbol{x}) = \frac{1}{\det \mathbf{D}(\hat{\boldsymbol{x}})} \mathbf{D}(\hat{\boldsymbol{x}}) \hat{\boldsymbol{v}}(\hat{\boldsymbol{x}}). \quad (3.3)$$

In our case, since $\mathbf{D}(\hat{\boldsymbol{x}}) = \text{const}$, a vector field is transformed by simple stretching of the individual components.

In the remainder of this section, we work in the reference configuration exclusively. Therefore, we drop the hat notation although we still denote quantities on the reference element.

3.2.1 Velocity space

We introduce the MJT space

$$\mathbf{V}(K) = \mathbf{P}_1(K) + \text{Span}\{\mathbf{curl} \boldsymbol{\chi}_i, i = 1, \dots, 12\}, \quad (3.4)$$

where

$$\begin{aligned}
\boldsymbol{\chi}_1 &= \begin{pmatrix} 0 \\ 0 \\ xy^2 \end{pmatrix}; & \boldsymbol{\chi}_2 &= \begin{pmatrix} 0 \\ xz^2 \\ 0 \end{pmatrix}; & \boldsymbol{\chi}_3 &= \begin{pmatrix} 0 \\ yz^2 \\ 0 \end{pmatrix}; & \boldsymbol{\chi}_4 &= \begin{pmatrix} 0 \\ 0 \\ xy^2z \end{pmatrix}; \\
\boldsymbol{\chi}_5 &= \begin{pmatrix} 0 \\ 0 \\ x^2y \end{pmatrix}; & \boldsymbol{\chi}_6 &= \begin{pmatrix} 0 \\ 0 \\ x^2z \end{pmatrix}; & \boldsymbol{\chi}_7 &= \begin{pmatrix} yz^2 \\ 0 \\ 0 \end{pmatrix}; & \boldsymbol{\chi}_8 &= \begin{pmatrix} xyz^2 \\ 0 \\ 0 \end{pmatrix}; \\
\boldsymbol{\chi}_9 &= \begin{pmatrix} xy^2 \\ 0 \\ 0 \end{pmatrix}; & \boldsymbol{\chi}_{10} &= \begin{pmatrix} 0 \\ x^2z \\ 0 \end{pmatrix}; & \boldsymbol{\chi}_{11} &= \begin{pmatrix} y^2z \\ 0 \\ 0 \end{pmatrix}; & \boldsymbol{\chi}_{12} &= \begin{pmatrix} 0 \\ x^2yz \\ 0 \end{pmatrix}.
\end{aligned}$$

The components v_x, v_y, v_z of a vector field $\mathbf{v} \in \mathbf{V}(K)$ take the form:

$$\begin{aligned}
v_x &= a_0 + a_1x + a_2y + a_3z + 2r_1xy - 2r_2xz \\
&\quad - 2r_3yz + 2r_4xyz + (r_5 - r_{10})x^2 - r_{12}x^2y,
\end{aligned} \tag{3.5}$$

$$\begin{aligned}
v_y &= b_0 + b_1x + b_2y + b_3z - 2r_5xy - 2r_6xz \\
&\quad + 2r_7yz + 2r_8xyz + (r_{11} - r_1)y^2 - r_4y^2z,
\end{aligned} \tag{3.6}$$

$$\begin{aligned}
v_z &= c_0 + c_1x + c_2y + c_3z - 2r_9xy + 2r_{10}xz \\
&\quad - 2r_{11}yz + 2r_{12}xyz + (r_2 - r_7)z^2 - r_8xz^2.
\end{aligned} \tag{3.7}$$

The essential observation is that a vector field $\mathbf{v} \in \mathbf{V}(K)$ has a bilinear normal component on every face of the reference hexahedron.

Lemma 3.2.1. $\dim \mathbf{V}(K) = 24$.

Proof. It suffices to show that the twelve polynomial vectors added to $\mathbf{P}_1(K)$ through $\mathbf{curl} \boldsymbol{\chi}_i, i = 1, \dots, 12$ are independent. Let $\mathbf{v} \in \text{Span}\{\mathbf{curl} \boldsymbol{\chi}_i, i = 1, \dots, 12\}$ with

$\mathbf{v} = \mathbf{0}$. The conditions $v_x = v_y = v_z = 0$ yield:

$$\begin{aligned} 2r_1xy - 2r_2xz - 2r_3yz + 2r_4xyz + (r_5 - r_{10})x^2 - r_{12}x^2y &= 0, \\ -2r_5xy - 2r_6xz + 2r_7yz + 2r_8xyz + (r_{11} - r_1)y^2 - r_4y^2z &= 0, \\ -2r_9xy + 2r_{10}xz - 2r_{11}yz + 2r_{12}xyz + (r_2 - r_7)z^2 - r_8xz^2 &= 0. \end{aligned} \quad (3.8)$$

The first component shows that

$$r_1 = r_2 = r_3 = r_4 = r_{12} = 0, \quad r_5 = r_{10}. \quad (3.9)$$

The second component implies that

$$r_5 = r_6 = r_7 = r_8 = 0, \quad r_{11} = r_1. \quad (3.10)$$

From Equations (3.9)–(3.10) we have that $r_{10} = r_{11} = 0$. The third component yields $r_9 = 0$. \square

We define the projection operator $\mathbf{\Pi}_K : \mathbf{H}^1(K) \rightarrow \mathbf{V}(K)$ as follows:

$$\langle (\mathbf{v} - \mathbf{\Pi}_K \mathbf{v}) \cdot \mathbf{n}_f, q \rangle_f = 0, \quad \forall q \in Q_1(f), \quad (3.11)$$

where f represents a face, and \mathbf{n}_f its outward unit normal. $Q_1(f)$ is the space of bilinear functions on f . The number of degrees of freedom defining the projection operator is $6 \times \dim Q_1(f) = 24$, and is therefore equal to the dimension of $\mathbf{V}(K)$. (We will later see that we associate the degrees of freedom with the component of the vector field normal to each face at the vertices of that face.)

Theorem 3.2.2.

1. The degrees of freedom defining $\mathbf{\Pi}_K$ determine $\mathbf{V}(K)$.
2. The global space \mathbf{V}_h induced by $\mathbf{V}(K)$ is conforming in $\mathbf{H}(\text{div})$.

Proof. Since the number of degrees of freedom defining $\mathbf{\Pi}_K$ is equal to the dimension of $\mathbf{V}(K)$, it suffices to establish unisolvence to prove the first assertion. We must show that for $\mathbf{\Pi}_K \mathbf{v} \in \mathbf{V}(K)$, if all the degrees of freedom $\langle \mathbf{\Pi}_K \mathbf{v} \cdot \mathbf{n}_f, q \rangle_f$, $\forall q \in Q_1(f)$ vanish, then $\mathbf{\Pi}_K \mathbf{v} \equiv \mathbf{0}$. From the form of the vector field (3.5)–(3.7), we have the following expressions for $\mathbf{\Pi}_K \mathbf{v} \cdot \mathbf{n}_f$ on the faces $x = \mp 1$, $y = \mp 1$, $z = \mp 1$, respectively:

$$\begin{aligned} \mathbf{\Pi}_K \mathbf{v} \cdot \mathbf{n}_{x=\mp 1} &= (a_0 \mp a_1 + (r_5 - r_{10})) + (a_2 \mp 2r_1 - r_{12})y \\ &\quad + (a_3 \pm 2r_2)z + (-2r_3 \mp 2r_4)yz, \end{aligned} \quad (3.12)$$

$$\begin{aligned} \mathbf{\Pi}_K \mathbf{v} \cdot \mathbf{n}_{y=\mp 1} &= (b_0 \mp b_2 + (r_{11} - r_1)) + (b_1 \pm 2r_5)x \\ &\quad + (b_3 \pm 2r_6 - r_4)z + (-2r_6 \mp 2r_8)xz, \end{aligned} \quad (3.13)$$

$$\begin{aligned} \mathbf{\Pi}_K \mathbf{v} \cdot \mathbf{n}_{z=\mp 1} &= (c_0 \mp c_3 + (r_2 - r_7)) + (c_1 \mp 2r_{10} - r_8)x \\ &\quad + (c_2 \pm 2r_{11})y + (-2r_9 \mp 2r_{12})xy. \end{aligned} \quad (3.14)$$

Because $\mathbf{\Pi}_K \mathbf{v} \cdot \mathbf{n}_f \in Q_1(f)$, vanishing degrees of freedom imply that the coefficients of the monomials in Equations (3.12)–(3.14) vanish. This yields 24 conditions on the coefficients of the vector field, which we write as a 24×24 linear system of equations:

$$\mathbf{M}\boldsymbol{\xi} = \mathbf{0}, \quad (3.15)$$

where $\boldsymbol{\xi} = [a_0, \dots, a_3, b_0, \dots, b_3, c_0, \dots, c_3, r_1, \dots, r_{12}]^T$. It can be checked that \mathbf{M} has full rank, so $\boldsymbol{\xi} = \mathbf{0}$ and the first assertion follows.

To prove the second assertion, we must show that if the degrees of freedom on a face f vanish, then the normal component $\mathbf{\Pi}_K \mathbf{v} \cdot \mathbf{n}_f \equiv 0$ on f . This immediately follows from the fact that $\mathbf{\Pi}_K \mathbf{v} \cdot \mathbf{n}_f \in Q_1(f)$ for all faces. \square

3.2.2 Pressure space

We define the space for the scalar variable on the reference element K as

$$W(K) = P_0(K), \quad (3.16)$$

and the associated projection operator $P_K : L^2(K) \rightarrow W(K)$ through

$$(p - P_K p, q)_K = 0, \quad \forall q \in W(K). \quad (3.17)$$

Remark 3.2.3. Our choice of velocity and pressure spaces satisfies that

$$\operatorname{div} \mathbf{V}(K) = W(K). \quad (3.18)$$

3.2.3 The new mixed finite element

We define our finite element in the sense of Ciarlet [25] as the following triplet $(K, \mathbf{M}(K), \mathcal{N}(K))$:

Definition 3.2.4.

1. The reference domain $K = [-1, 1]^3$.
2. The finite-dimensional space of functions on K :

$$\mathbf{M}(K) = \mathbf{V}(K) \times W(K). \quad (3.19)$$

3. The set of degrees of freedom for the velocity and pressure, respectively:

$$\langle \mathbf{\Pi}_K \mathbf{v} \cdot \mathbf{n}_f, q \rangle_f, \quad \forall q \in Q_1(f), \quad (3.20)$$

$$(P_K p, q)_K, \quad \forall q \in W(K). \quad (3.21)$$

Lemma 3.2.5. *The local projection operators $\mathbf{\Pi}_K$ and P_K satisfy the following commutativity property:*

$$\operatorname{div}\mathbf{\Pi}_K\mathbf{v} = P_K\operatorname{div}\mathbf{v} \quad \forall \mathbf{v} \in \mathbf{H}^1(K). \quad (3.22)$$

Proof. Let $\mathbf{v} \in \mathbf{H}^1(K)$ and let $q \in W(K)$. Using the Green formula for \mathbf{v} and its projection $\mathbf{\Pi}_K\mathbf{v} \in \mathbf{V}(K)$, we have

$$(\operatorname{div}(\mathbf{v} - \mathbf{\Pi}_K\mathbf{v}), q)_K = -(\mathbf{v} - \mathbf{\Pi}_K\mathbf{v}, \operatorname{grad}q)_K + \langle (\mathbf{v} - \mathbf{\Pi}_K\mathbf{v}) \cdot \mathbf{n}, q \rangle_{\partial K}. \quad (3.23)$$

Since $q \in W(K) \equiv P_0(K)$, the first term on the right hand side of Equation (3.23) vanishes. Also, from the definition of $\mathbf{\Pi}_K$, the second term is identically equal to zero. Equation (3.23) reduces to

$$(\operatorname{div}\mathbf{\Pi}_K\mathbf{v}, q)_K = (\operatorname{div}\mathbf{v}, q)_K \quad (3.24)$$

or, equivalently,

$$P_K\operatorname{div}\mathbf{\Pi}_K\mathbf{v} = P_K\operatorname{div}\mathbf{v}. \quad (3.25)$$

Since $W(K) = \operatorname{div}\mathbf{V}(K)$, then $\operatorname{div}\mathbf{\Pi}_K\mathbf{v} \in \operatorname{Im}P_K$ and the lemma follows. \square

Remark 3.2.6. Property (3.22) is often expressed by stating that the following diagram commutes:

$$\begin{array}{ccc} \mathbf{H}^1(K) & \xrightarrow{\operatorname{div}} & L^2(K) \\ \mathbf{\Pi}_K \downarrow & & \downarrow P_K \\ \mathbf{V}(K) & \xrightarrow{\operatorname{div}} & W(K). \end{array} \quad (3.26)$$

3.3 Trapezoidal quadrature

For $\hat{\mathbf{v}}, \hat{\mathbf{u}} \in \hat{\mathbf{V}}(\hat{K})$, we introduce the trapezoidal quadrature on the reference element \hat{K} :

$$(\hat{\mathbf{v}}, \hat{\mathbf{k}}^{-1} \hat{\mathbf{u}})_{\hat{Q}, \hat{K}} := \sum_{i=1}^8 \hat{\mathbf{v}}(\hat{\mathbf{x}}_i) \cdot \hat{\mathbf{k}}^{-1}(\hat{\mathbf{x}}_i) \hat{\mathbf{u}}(\hat{\mathbf{x}}_i), \quad (3.27)$$

where $\hat{\mathbf{x}}_i$ refers to the coordinates of the i^{th} vertex of the reference element. Using the coordinate mapping and the Piola transform, we have, for element K in physical space:

$$\begin{aligned} (\mathbf{v}, \mathbf{k}^{-1} \mathbf{u})_K &= \left(\frac{1}{\det \mathbf{D}(\hat{\mathbf{x}})} \mathbf{D}(\hat{\mathbf{x}}) \hat{\mathbf{v}}(\hat{\mathbf{x}}), \mathbf{k}^{-1} \frac{1}{\det \mathbf{D}(\hat{\mathbf{x}})} \mathbf{D}(\hat{\mathbf{x}}) \hat{\mathbf{u}}(\hat{\mathbf{x}}) \det \mathbf{D}(\hat{\mathbf{x}}) \right)_{\hat{K}} \\ &= (\hat{\mathbf{v}}, \hat{\mathbf{k}}^{-1} \hat{\mathbf{u}})_{\hat{K}}, \end{aligned} \quad (3.28)$$

where $\hat{\mathbf{k}} = \det \mathbf{D} \mathbf{D}^{-1} \mathbf{k} \mathbf{D}^{-t}$ is the pull-back of the permeability tensor [48]. The quadrature rule on element K is then defined as:

$$(\mathbf{v}, \mathbf{k}^{-1} \mathbf{u})_{Q, K} := (\hat{\mathbf{v}}, \hat{\mathbf{k}}^{-1} \hat{\mathbf{u}})_{\hat{Q}, \hat{K}}. \quad (3.29)$$

We extend this definition to functions $\mathbf{v}, \mathbf{u} \in \mathbf{V}_h$ by defining the global quadrature

$$(\mathbf{v}, \mathbf{k}^{-1} \mathbf{u})_Q = \sum_{K \in \mathcal{T}_h} (\mathbf{v}, \mathbf{k}^{-1} \mathbf{u})_{Q, K}. \quad (3.30)$$

Lemma 3.3.1. *The form $(\cdot, \mathbf{k}^{-1} \cdot)_Q$ is an inner product in \mathbf{V}_h and $(\cdot, \mathbf{k}^{-1} \cdot)_Q^{1/2}$ is a norm on \mathbf{V}_h equivalent to $\|\cdot\|_{L^2(\Omega)}$.*

Proof. Because the linearity and symmetry are trivial, it suffices to verify positiveness to prove that $(\cdot, \mathbf{k}^{-1} \cdot)_Q$ is an inner product in \mathbf{V}_h . Let $\mathbf{v} \in \mathbf{V}_h$. On any element K , we can express $\mathbf{v}|_K$ as a linear combination of the shape functions \mathbf{N}_i describing $\mathbf{V}(K)$. From Equations (2.14) and (3.29), and because \mathbf{k} is a uniformly positive, bounded

tensor, we have

$$c_0 \|\mathbf{v}|_K\|_{L^2(K)}^2 \leq (\mathbf{v}|_K, \mathbf{k}^{-1} \mathbf{v}|_K)_{Q,K} \leq c_1 \|\mathbf{v}|_K\|_{L^2(K)}^2. \quad (3.31)$$

From Equation (3.30), we have, globally,

$$C_0 \|\mathbf{v}\|_{L^2(\Omega)}^2 \leq (\mathbf{v}, \mathbf{k}^{-1} \mathbf{v})_Q \leq C_1 \|\mathbf{v}\|_{L^2(\Omega)}^2. \quad (3.32)$$

The lower bound of Equation (3.32) proves the positivity of $(\cdot, \mathbf{k}^{-1} \cdot)_Q$. The upper bound of Equation (3.32) proves that $(\cdot, \mathbf{k}^{-1} \cdot)_Q^{1/2}$ is a norm equivalent to $\|\cdot\|_{L^2(\Omega)}$. \square

Let us now consider the mixed finite element method perturbed by the application of the quadrature (3.30): we seek $(\tilde{\mathbf{u}}_h, \tilde{p}_h) \in \mathbf{M}_h$ such that

$$(\mathbf{v}_h, \mathbf{k}^{-1} \tilde{\mathbf{u}}_h)_Q - (\operatorname{div} \mathbf{v}_h, \tilde{p}_h) = -\langle \mathbf{v}_h \cdot \mathbf{n}, \bar{p} \rangle_{\Gamma_D} \quad \forall \mathbf{v}_h \in \mathbf{V}_h, \quad (3.33)$$

$$(q_h, \operatorname{div} \tilde{\mathbf{u}}_h) = (q_h, f) \quad \forall q_h \in W_h. \quad (3.34)$$

The tilde indicates the perturbation due to the numerical quadrature.

3.4 Localization into MPFA

In the MFE system (2.16), the elements A_{ij} of the matrix \mathbf{A} represent the interaction between the i th and j th velocity unknowns:

$$A_{ij} = (\mathbf{N}_i^u, \mathbf{k}^{-1} \mathbf{N}_j^u)_Q. \quad (3.35)$$

The new velocity space is designed so that each velocity shape function vanishes at all, but one vertex (**Figures 3.1–3.2**). Since the trapezoidal quadrature only involves the grid vertices, the elements A_{ij} can be nonzero only when they involve two unknowns

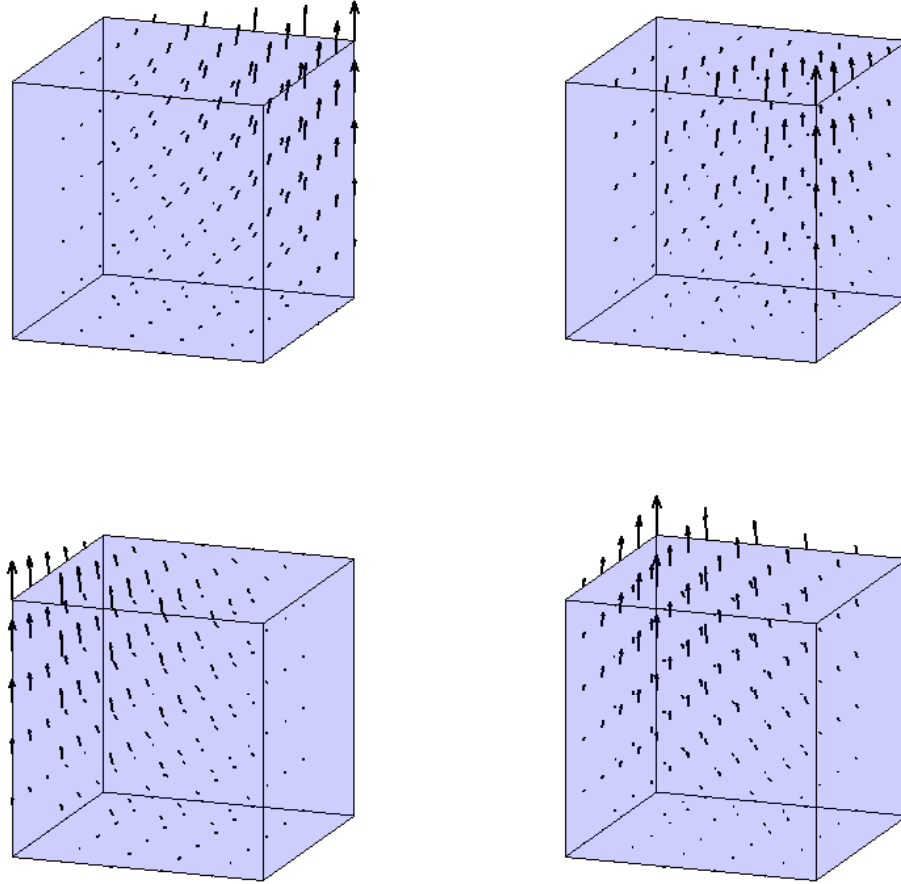


Figure 3.1. The four vertex-based MJT shape functions for the top face of the reference hexahedron.

representing velocity components on the same vertex.

Around a given vertex v , a local system can thus be formed, which involves only the twelve velocity unknowns U_i (four in each direction, see **Figure 3.3**) located at that vertex, and the cell-centered pressures P_j of the eight elements sharing that vertex:

$$\mathbf{A}_v \mathbf{u}_v = \mathbf{B}_v^t \mathbf{p}_v, \quad (3.36)$$

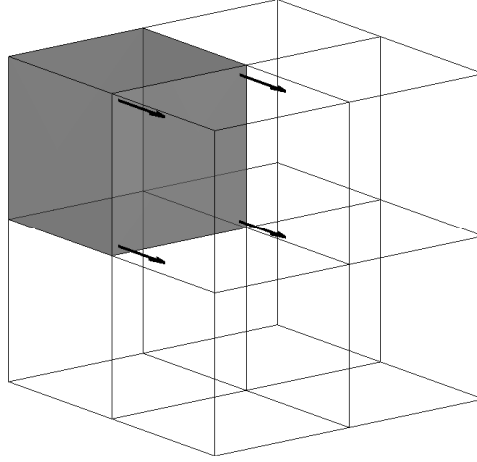


Figure 3.2. Representation of the four vertex-based MJT velocity degrees of freedom associated with a face of a three-dimensional Cartesian grid.

with $\mathbf{u}_v = [U_1 \ U_2 \ \dots \ U_{12}]^t$, $\mathbf{p}_v = [P_1 \ P_2 \ \dots \ P_8]^t$, and \mathbf{A}_v and \mathbf{B}_v^t the restrictions of \mathbf{A} and \mathbf{B}^t to the local system. \mathbf{A}_v is symmetric positive definite and can be inverted to give the velocity unknowns as a function of the pressure unknowns:

$$\mathbf{u}_v = \mathbf{M}\mathbf{u}_v, \text{ with } \mathbf{M} = \mathbf{A}_v^{-1}\mathbf{B}_v^t. \quad (3.37)$$

In multipoint flux approximation methods, each face is divided into four subfaces, over which the flux is approximated (see, e.g. [1]). An interaction region is formed around each vertex to determine the fluxes through the twelve subfaces involved from the eight neighboring cell-centered pressures:

$$\mathbf{f}_{\text{subfaces}} = \mathbf{M}_{\text{MPFA}}\mathbf{p}_v, \quad (3.38)$$

where $\mathbf{f}_{\text{subfaces}} = [f_1, \dots, f_{12}]^t$ is the vector of unknown fluxes through the subfaces and \mathbf{M}_{MPFA} is a local transmissibility matrix. **Figure 3.3** represents the eight elements and twelve subfaces involved in an MPFA interaction region for a three-dimensional rectangular grid.

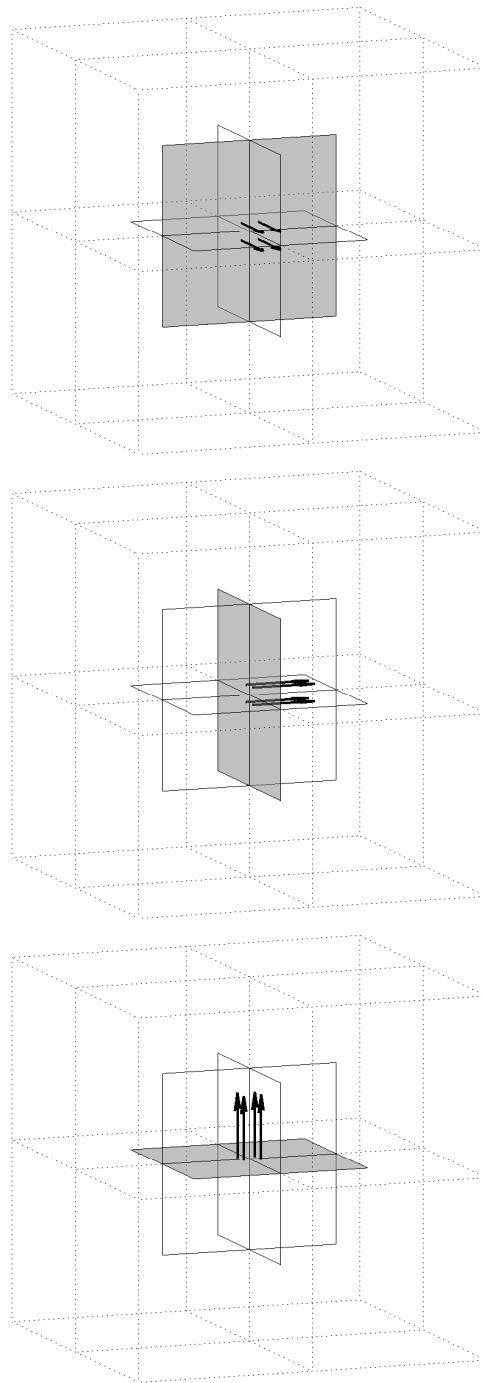


Figure 3.3. The eight elements (dotted line) and twelve subfaces (solid lines) of an MPFA interaction region and their associated twelve MJT velocity degrees of freedom (arrows) for a three-dimensional Cartesian grid.

Although the elements of the matrices \mathbf{M} and \mathbf{M}_{MPFA} are too complex to be reported here, it can be checked analytically that,

$$\mathbf{M} = \mathbf{M}_{\text{MPFA}}. \quad (3.39)$$

Therefore, the degrees of freedom of the new velocity space correspond exactly to the subfluxes of the MPFA O-method. The new mixed finite element method with the trapezoidal quadrature is nothing else than the MPFA O-method for rectangular hexahedral grids (REFERENCES).

To visualize the localizing effect of the trapezoidal quadrature, let us re-write (2.16) as (2.22):

$$\mathbf{C} \mathbf{p} = \mathbf{R}.$$

When the mixed finite element system is fully integrated, \mathbf{A}^{-1} is a full matrix, which leads to a full matrix \mathbf{C} . However, sub-integration by trapezoidal quadrature renders a block-diagonal matrix \mathbf{A} and, in turn, a block-diagonal inverse \mathbf{A}^{-1} (12×12 blocks). Matrix \mathbf{C} becomes sparse and the MPFA O-method is recovered. **Figure 3.4** represents the matrix \mathbf{C} obtained on a $3 \times 3 \times 3$ grid (27 elements) with the MJT space for the following three cases:

1. *Full integration.* \mathbf{C} is full.
2. *Trapezoidal quadrature and diagonal permeability tensor.* The classical 7-point stencil of the finite difference or TPFA method is recovered.
3. *Trapezoidal quadrature and full permeability tensor.* The discretization leads to a 27-point stencil that is equivalent to the MPFA-O method.

Figure 3.5 shows the sparse finite volume system with a 27-point stencil obtained for a $5 \times 5 \times 5$ Cartesian grid populated with a full-tensor permeability.

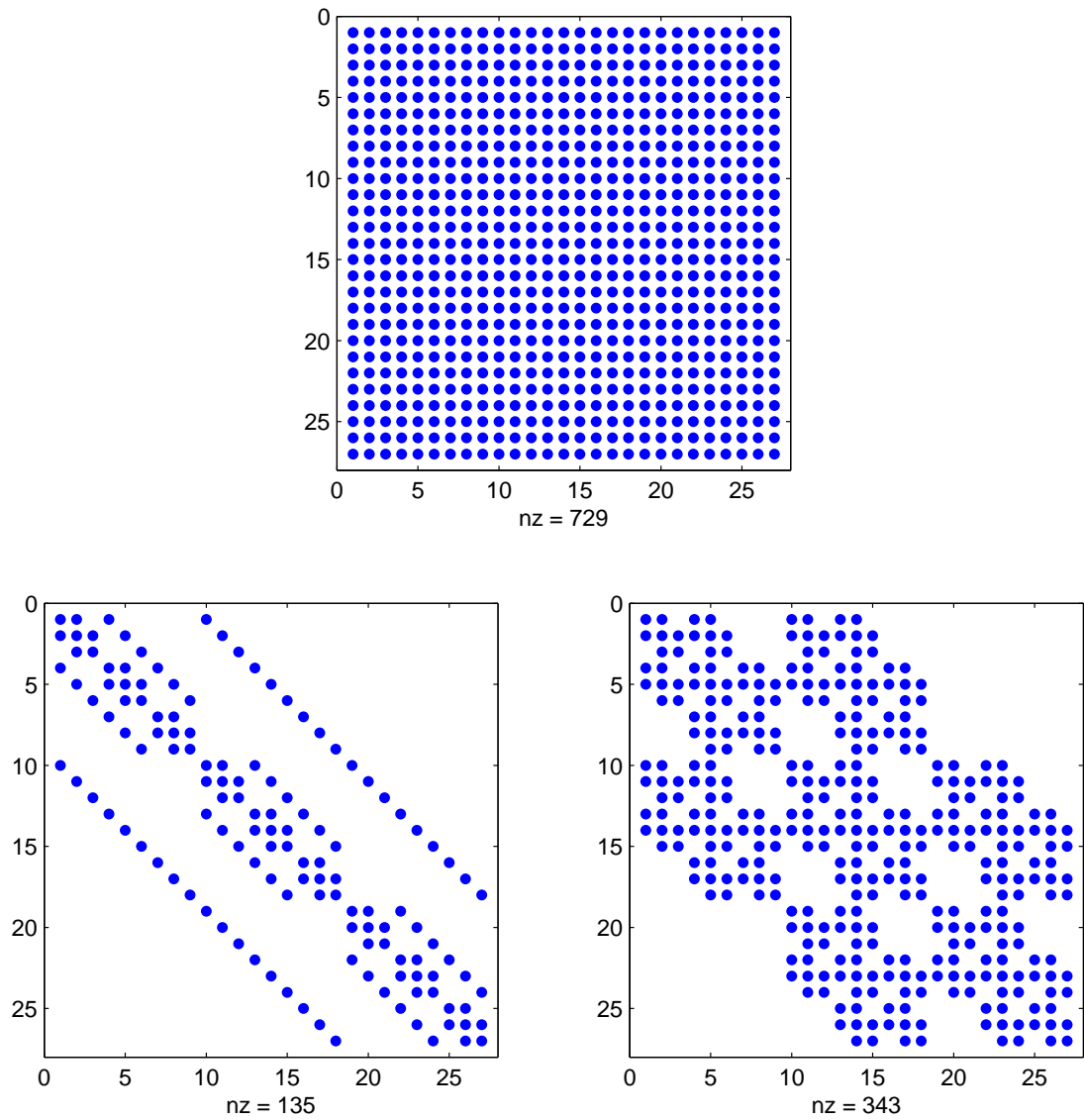


Figure 3.4. Stencils of the fully-integrated (top) and localized new mixed finite element method in the case of diagonal (bottom-left) and full-tensor (bottom-right) permeability coefficients.

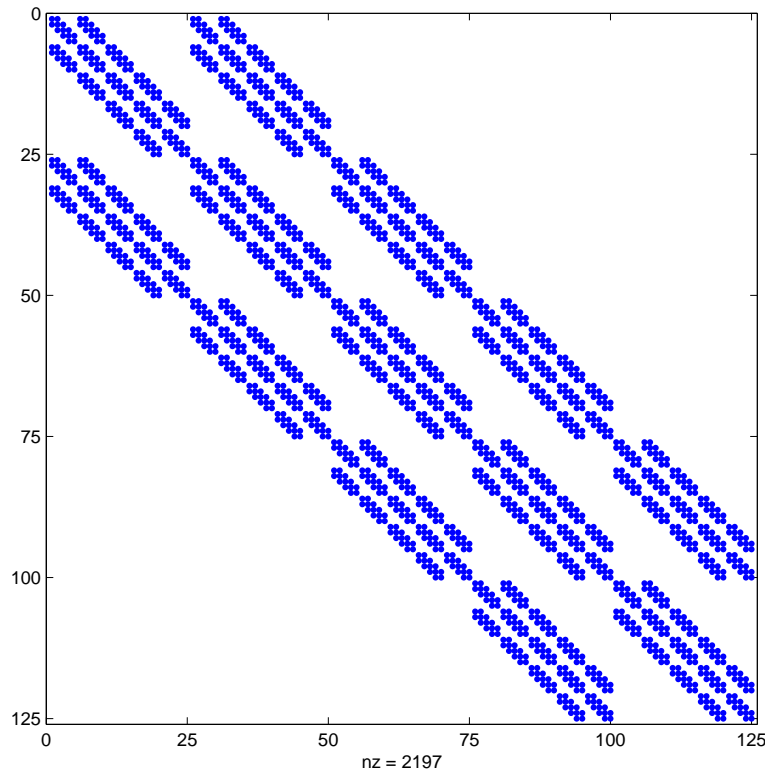


Figure 3.5. Matrix of the localized M -based MFE for a $5 \times 5 \times 5$ grid, reproducing the well-known structure of the 27-point stencil.

3.5 Numerical experiments

3.5.1 Patch tests

In this section, we test the ability of the various discretizations presented in this thesis to reproduce a constant velocity field on general hexahedral grids. The RT_0 -based MFE method is known to fail such a test, even when the element faces are planar [57]. The performance of higher-order mixed finite element methods is, however, unpublished. BDM_1 and MJT will, in general, not reproduce the exact solution for distorted hexahedral grids, whereas the MPFA O-method is designed to satisfy this test.

The uniform-flow test case is set up in a domain of unit dimensions. The faces located at $x = 0$ and $x = 1$ are assigned Dirichlet boundary conditions with a pressure

Table 3.1. Average time-of-flight error of the various discretizations on the three patch tests.

Test case	RT ₀	BDM ₁	MJT	MPFA
1	2.03 %	0 %	0 %	0 %
2	8.91 %	0 %	0 %	0 %
3	1.9 %	0.003 %	0.001 %	1.25 %

of one and zero, respectively. All other boundaries are impermeable. The porous medium is isotropic and of unit permeability. The exact solution to this problem consists of a linear pressure variation and a constant velocity field in the x -direction.

Three grids were used to assess the behavior of the various discretizations when handling general hexahedra:

1. *Pyramid*: A $3 \times 3 \times 3$ grid consisting of elements that make up the shape of truncated pyramids. All faces of this grid are planar.
2. *Twisted face*: The grid is formed by two elements stacked in the vertical direction. The face shared by the two elements has a saddle shape. It is twisted in such a way that there is no net flow through it, even though it is not aligned with the flow direction.
3. *General hexahedra*: A $4 \times 4 \times 4$ grid, shown in **Figure 3.8**, which consists of general hexahedra with curved faces.

The first two grids are inspired by the test cases of Naff *et al.* [57]

To assess the quality of the velocity discretization on these grids, we used the algorithm presented in Chapter 5 to trace the *exact* streamlines corresponding to the flow field. We compare the numerical travel time necessary to completely cross the domain to its theoretical unit value. The errors of each method for the three grids are reported in **Table 3.1**.

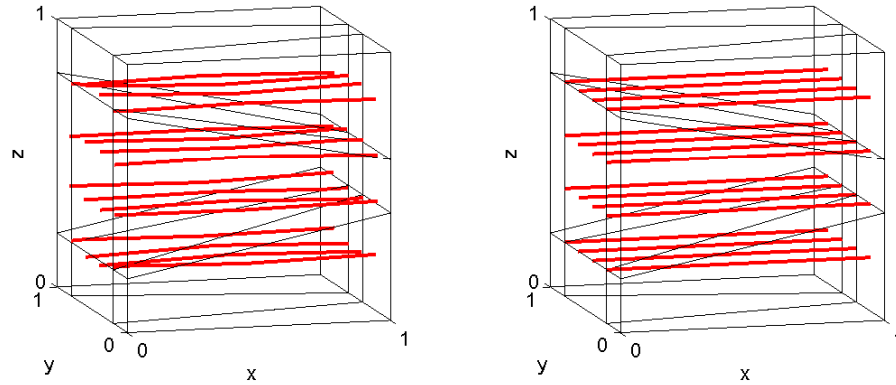


Figure 3.6. RT_0 (left) failing and BDM_1 (right) passing the first patch test involving elements in shape of truncated pyramids.

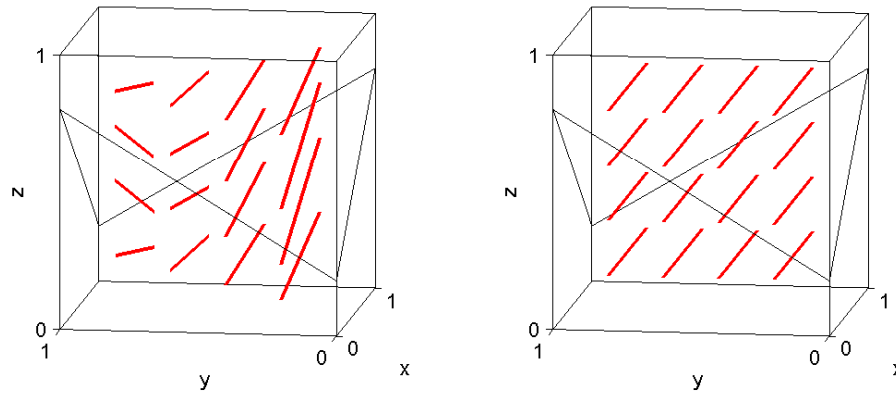


Figure 3.7. RT_0 (left) failing and BDM_1 (right) passing the second patch test involving a nonplanar face.

It is clear that for the first two test cases, RT_0 does not produce the exact solution, while BDM_1 does. **Figure 3.6** (pyramid grid) and **Figure 3.7** (twisted grid) show sixteen streamlines obtained with the RT_0 and BDM_1 mixed finite element methods. For these two cases, the fully-integrated and reduced-integrated MJT-based mixed finite element method yield exact streamlines, which therefore overlap with those from BDM_1 .

High-order mixed finite element methods, however, are not guaranteed to represent

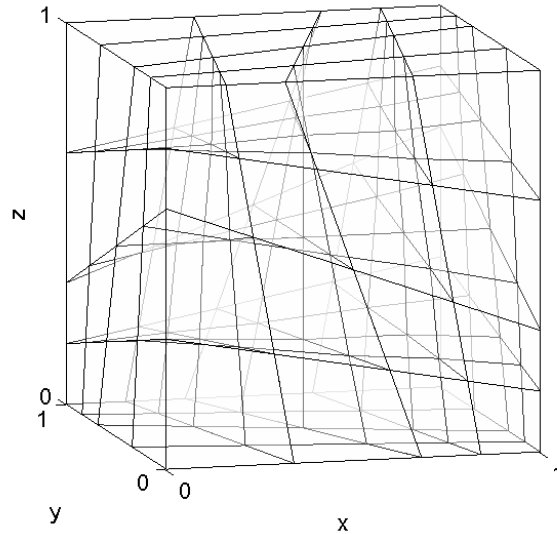


Figure 3.8. $4 \times 4 \times 4$ grid of general hexahedra used for the third patch test.

a constant velocity field exactly on general hexahedral grids. The reason behind this behavior is the highly nonlinear dependence of the determinant of the Jacobian J on the geometry in the Piola transform of the velocity. **Figure 3.9** shows the streamlines for the third test case (the distorted hexahedral grid of **Figure 3.8**). In this case, even though very accurate, the higher order mixed methods do not represent the uniform flow test case exactly. It is also apparent that, in this case, reduced integration degrades the global accuracy of the MJT-based mixed finite element method.

3.5.2 Monotonicity properties

Exact solutions of the elliptic pressure equation must satisfy the maximum principle: in the absence of sources or sinks, the pressure inside the domain cannot be above (below) the maximum (minimum) value at the boundary. This property is violated by most discretization methods, when the permeability anisotropy is large and misaligned with the simulation grid. In this section, we test the monotonicity of the various

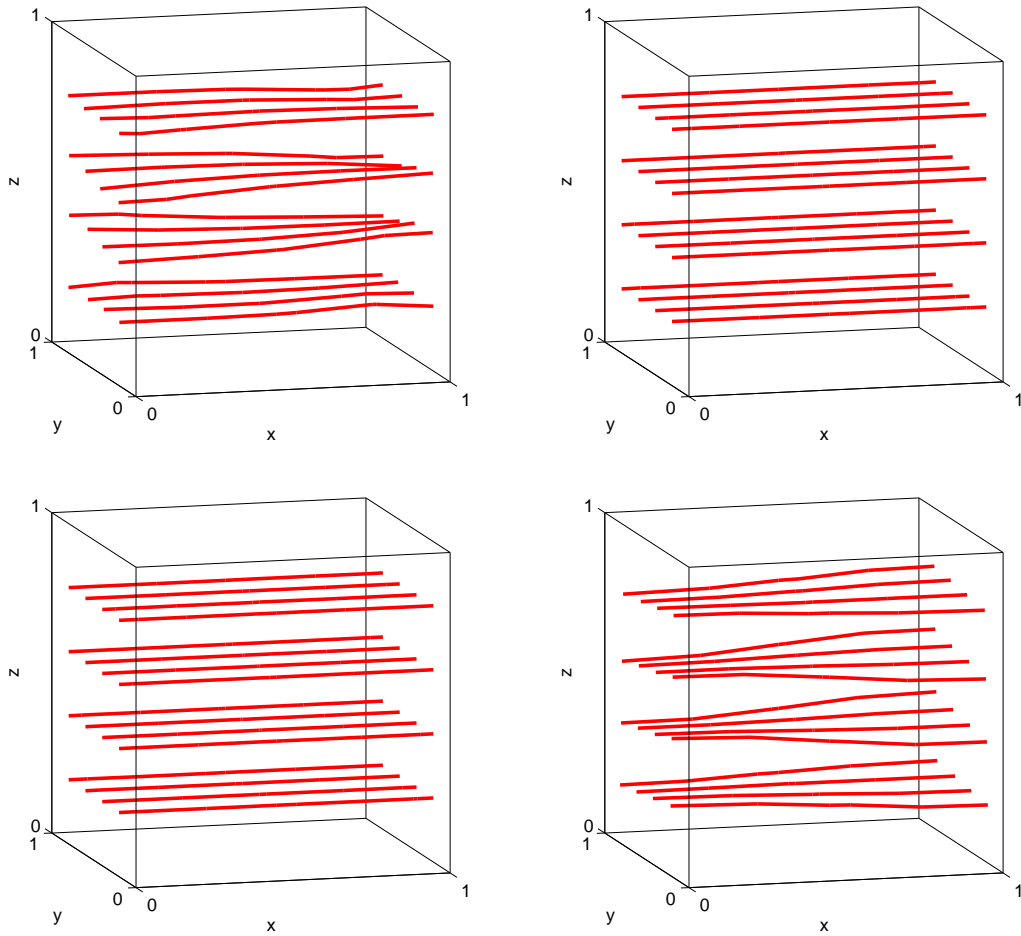


Figure 3.9. Streamlines obtained by RT_0 (top-left), fully integrated BDM_1 (top-right), fully integrated MJT (bottom-left) and localized MJT (bottom-right) for the third patch test.

discretizations presented in this paper.

The test problem is defined on a domain of unit dimensions discretized with a $9 \times 9 \times 9$ Cartesian grid. The boundaries of the domain are set to a zero pressure and the center gridcell is fixed at unit pressure. The permeability is homogeneous, but highly anisotropic. The principal values of the permeability tensor are $(100, 1, 1)$. The principal direction associated with the largest permeability is in the horizontal (x, y) -plane, and forms an angle θ with the x -axis.

In view of the maximum principle, the pressure should be nonnegative. The magnitude of the negative values obtained with a numerical method can, therefore, be considered as a measure of the severity of non-monotonicity. In **Figure 3.10**, we plot the minimum value of the pressure computed with the different methods, as a function of the rotation angle θ of the permeability tensor. The first observation is that for such a high permeability anisotropy, all methods considered here (RT_0 , BDM_1 , MJT and localized-MJT) produce non-monotonic solutions for some range of the rotation angle θ . Not all methods, however, produce equally unsatisfactory results. The RT_0 discretization is the worst, yielding non-monotonic solutions for all θ , with minimum pressures around $p_{\min} \approx -0.18$ for $\theta \in [20^\circ, 45^\circ]$. The mixed finite element discretizations based on the BDM_1 space and the new MJT space produce much better (and similar) results: minimum pressures around $p_{\min} \approx -0.03$, and monotonic solutions when θ approaches 45° . This monotonic behavior in the limit $\theta \rightarrow 0^\circ$ and $\theta \rightarrow 45^\circ$ is preserved by the localized version of the MJT method. For intermediate values of θ , however, the quality of the solution degrades substantially ($p_{\min} \approx -0.15$).

3.6 Summary

In this chapter, we introduced a new mixed finite element method for general hexahedral elements. The method is based on a new velocity space defined by the components of the velocity field at the face *vertices*, which generates a bilinear velocity approximation on each face. The new velocity space induces the commutativity property (3.22), which is used to show the consistency proof presented in the next chapter.

The vertex-based trapezoidal quadrature was then introduced. It was shown to form an inner product in \mathbf{V}_h but does not integrate the MFE system exactly. Because the MJT velocity shape functions are vertex-based, the trapezoidal quadrature

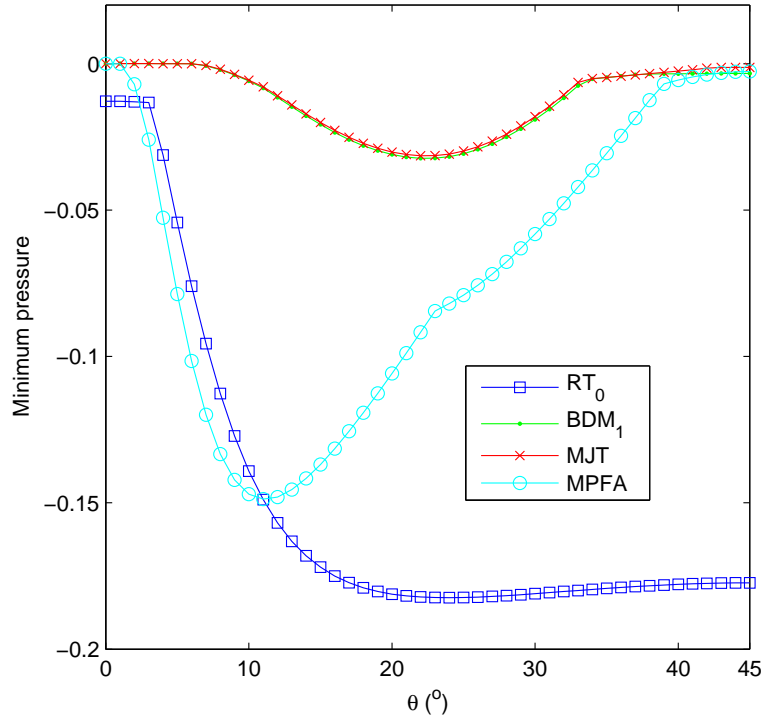


Figure 3.10. Monotonicity test of the various discretization methods for a rotating permeability tensor with 100/1 anisotropy ratio.

localizes the interactions between the velocity degrees of freedom. The velocity unknowns can be eliminated through the solution of local systems that correspond to the MPFA systems formed within the interaction regions. This shows that the localized MJT method is, in fact, the sparse (local support) MPFA O-method.

Finally, we compared via numerical experiments the performance of classical (RT_0 and BDM_1) MFE methods to the MJT-based discretization, and to MPFA. The MJT-based method was found to be the most robust discretization, in terms of sensitivity to grid distortion and permeability anisotropy.

Chapter 4

Convergence analysis

This chapter contains the mathematical analysis of the MJT-based MFE method. MJT is shown to verify the Babuška-Brezzi condition, which establishes the consistency of the induced MFE method. The error analysis of the BDM spaces can be carried out without modifications for the MJT space, which is thus proved convergent and optimal error estimates are provided.

The influence of the localizing trapezoidal quadrature on the consistency and convergence of the MFE method is then investigated. An error analysis shows that although the convergence is affected by the inexact quadrature, the MPFA method induced by the inexact integration of *MJT* remains convergent.

4.1 Consistency and convergence of the new MFE

Let $\hat{\mathbf{V}}(\hat{K})$ and $\hat{W}(\hat{K})$ be, respectively, the velocity and pressure spaces on the reference element, as defined above. Let $\mathbf{V}(K)$ and $W(K)$ be their equivalent on physical space, defined via the transformations (3.3) and (3.2), respectively. Now, let $\mathbf{\Pi}_K$ and P_K be the local projection operators (in physical space) associated with $\mathbf{V}(K)$ and $W(K)$. Also, let $h_K = \text{diam}(K) = \max\{h_x, h_y, h_z\}$.

The approximation properties of the projection operators are well known [17]. Since the mapping from reference to physical space is affine, $\mathbf{V}(K) \supset \mathbf{P}_1(K)$ and $W(K) = P_0(K)$, and we have

$$\|\mathbf{v} - \mathbf{\Pi}_K \mathbf{v}\|_{L^2(K)} \leq C \|\mathbf{v}\|_{H^r(K)} h_K^r, \quad 1 \leq r \leq 2. \quad (4.1)$$

$$\|\operatorname{div}(\mathbf{v} - \mathbf{\Pi}_K \mathbf{v})\|_{L^2(K)} \leq C \|\operatorname{div} \mathbf{v}\|_{H^r(K)} h_K^r, \quad 0 \leq r \leq 1. \quad (4.2)$$

$$\|q - P_K q\|_{L^2(K)} \leq C \|q\|_{H^r(K)} h_K^r, \quad 0 \leq r \leq 1. \quad (4.3)$$

We have the local properties of our mixed finite element. In order to construct the global spaces, let \mathcal{T}_h be a partition of the domain Ω into rectangular parallelepipeds $\{K\}$. We define the global spaces

$$\mathbf{V}_h \equiv \mathbf{V}(\mathcal{T}_h) := \{\mathbf{v} \in \mathbf{H}_{0,N}(\operatorname{div}, \Omega) : \mathbf{v}|_K \in \mathbf{V}(K) \forall K \in \mathcal{T}_h\}, \quad (4.4)$$

$$W_h \equiv W(\mathcal{T}_h) := \{q \in L^2(\Omega) : q|_K \in W(K) \forall K \in \mathcal{T}_h\}, \quad (4.5)$$

$$\mathbf{M}_h := \mathbf{V}_h \times W_h. \quad (4.6)$$

We extend the projections $\mathbf{\Pi}_K$ and P_K to $\mathbf{H}^1(\Omega)$ and $L^2(\Omega)$, respectively, in the classical way:

$$\mathbf{\Pi}_h : \mathbf{H}^1(\Omega) \rightarrow \mathbf{V}_h \quad \text{with } \mathbf{\Pi}_h|_{H^1(K)} = \mathbf{\Pi}_K, \quad (4.7)$$

$$P_h : L^2(\Omega) \rightarrow W_h \quad \text{with } P_h|_{L^2(K)} = P_K. \quad (4.8)$$

The global commutativity property

$$\begin{array}{ccc} \mathbf{H}^1(\Omega) & \xrightarrow{\operatorname{div}} & L^2(\Omega) \\ \mathbf{\Pi}_h \downarrow & & \downarrow P_h \\ \mathbf{V}_h & \xrightarrow{\operatorname{div}} & W_h, \end{array} \quad (4.9)$$

and global approximation properties

$$\|\mathbf{v} - \mathbf{\Pi}_h \mathbf{v}\|_{L^2(\Omega)} \leq C \|\mathbf{v}\|_{H^r(\Omega)} h^r, \quad 1 \leq r \leq 2. \quad (4.10)$$

$$\|\operatorname{div}(\mathbf{v} - \mathbf{\Pi}_h \mathbf{v})\|_{L^2(\Omega)} \leq C \|\operatorname{div} \mathbf{v}\|_{H^r(\Omega)} h^r, \quad 0 \leq r \leq 1. \quad (4.11)$$

$$\|q - P_h q\|_{L^2(\Omega)} \leq C \|q\|_{H^r(\Omega)} h^r, \quad 0 \leq r \leq 1. \quad (4.12)$$

follow immediately from the local properties [17].

Theorem 4.1.1. *There exists a unique solution $(\mathbf{u}_h, p_h) \in \mathbf{M}_h$ to the discrete problem (2.12)–(2.13). Let $(\mathbf{u}, p) \in \mathbf{V} \times W \equiv \mathbf{H}_{0,N}(\operatorname{div}, \Omega) \times L^2(\Omega)$ be the solution to the continuous problem (2.10)–(2.11). Then we have the following error estimates:*

$$\|\mathbf{u} - \mathbf{u}_h\|_{L^2(\Omega)} \leq Ch^r \|\mathbf{u}\|_{H^r(\Omega)}, \quad 1 \leq r \leq 2. \quad (4.13)$$

$$\|\operatorname{div}(\mathbf{u} - \mathbf{u}_h)\|_{L^2(\Omega)} \leq Ch^s \|\operatorname{div} \mathbf{u}\|_{H^s(\Omega)}, \quad 0 \leq s \leq 1. \quad (4.14)$$

$$\|p - p_h\|_{L^2(\Omega)} \leq Ch (\|p\|_{H^1(\Omega)} + \|\mathbf{u}\|_{H(\operatorname{div}, \Omega)}). \quad (4.15)$$

Proof. We define

$$\mathbf{Z}_h = \{\mathbf{v} \in \mathbf{V}_h : (\operatorname{div} \mathbf{v}, q) = 0 \quad \forall q \in W_h\}. \quad (4.16)$$

It is well known [17] that a unique solution $(\mathbf{u}_h, p_h) \in \mathbf{V}_h \times W_h$ exists if the pair (\mathbf{V}_h, W_h) is such that the following conditions are satisfied:

$$(\mathbf{v}, \mathbf{k}^{-1} \mathbf{v}) \geq c \|\mathbf{v}\|_{H(\operatorname{div}, \Omega)}^2 \quad \forall \mathbf{v} \in \mathbf{Z}_h, \quad (4.17)$$

$$\sup_{\mathbf{v} \in \mathbf{V}_h} \frac{(\operatorname{div} \mathbf{v}, q)}{\|\mathbf{v}\|_{H(\operatorname{div}, \Omega)}} \geq c \|q\|_{L^2(\Omega)} \quad \forall q \in W_h. \quad (4.18)$$

Let $\mathbf{v} \in \mathbf{Z}_h$, we have $\operatorname{div} \mathbf{v} \in \operatorname{div} \mathbf{V}_h = W_h$ and since $\operatorname{div} \mathbf{Z}_h \perp W_h$, we have $\|\operatorname{div} \mathbf{v}\|_{L^2(\Omega)}^2 = 0$, so that

$$\|\mathbf{v}\|_{H(\operatorname{div}, \Omega)}^2 = \|\mathbf{v}\|_{L^2(\Omega)}^2. \quad (4.19)$$

Now, from the ellipticity of the bilinear form $(\cdot, \mathbf{k}^{-1}\cdot)$ we have

$$(\mathbf{v}, \mathbf{k}^{-1}\mathbf{v}) \geq c\|\mathbf{v}\|_{L^2(\Omega)}^2 \quad (4.20)$$

The coercivity condition (4.17) follows immediately from (4.19)–(4.20).

Since the commutativity property (4.9) holds, the inf-sup condition (4.18) is equivalent to continuity of the velocity projection operator $\mathbf{\Pi}_h$ [13], that is:

$$\|\mathbf{\Pi}_h\mathbf{v}\|_{H(\text{div},\Omega)} \leq C\|\mathbf{v}\|_{H(\text{div},\Omega)}. \quad (4.21)$$

To show (4.21), we use the global approximation results (4.10) and the classical inverse estimates [25]:

$$\|\mathbf{v}\|_{H^1(\Omega)} \leq Ch^{-1}\|\mathbf{v}\|_{L^2(\Omega)}, \quad (4.22)$$

$$\|\text{div}\mathbf{v}\|_{H^1(\Omega)} \leq Ch^{-1}\|\text{div}\mathbf{v}\|_{L^2(\Omega)}. \quad (4.23)$$

Indeed,

$$\begin{aligned} \|\mathbf{\Pi}_h\mathbf{v}\|_{H(\text{div},\Omega)} &\leq \|\mathbf{\Pi}_h\mathbf{v} - \mathbf{v}\|_{L^2(\Omega)} + \|\mathbf{v}\|_{L^2(\Omega)} \\ &\quad + \|\text{div}(\mathbf{\Pi}_h\mathbf{v} - \mathbf{v})\|_{L^2(\Omega)} + \|\text{div}\mathbf{v}\|_{L^2(\Omega)} \\ &\leq Ch \left(\|\mathbf{v}\|_{H^1(\Omega)} + \|\text{div}\mathbf{v}\|_{H^1(\Omega)} \right) + \|\mathbf{v}\|_{H(\text{div},\Omega)} \\ &\leq C \left(\|\mathbf{v}\|_{L^2(\Omega)} + \|\text{div}\mathbf{v}\|_{L^2(\Omega)} \right) + \|\mathbf{v}\|_{H(\text{div},\Omega)}. \end{aligned} \quad (4.24)$$

The error estimates (4.13)–(4.15) follow directly from the analysis in Brezzi et al. [16] since the derivation of the estimates depends only on the approximation properties of $\mathbf{\Pi}_h$ and P_h . \square

4.2 Consistency and convergence of MPFA

In this section, we evaluate the influence of the inexact numerical quadrature used to localize the mixed finite element method on the convergence of the cell-centered finite difference method. The structure of the proof follows that of Wheeler and Yotov [70], but is simplified as we restrict the study to rectangular grids.

4.2.1 Consistency

Theorem 4.2.1. *The perturbed mixed finite element problem (3.33)–(3.34) admits a unique solution $(\tilde{\mathbf{u}}_h, \tilde{p}_h) \in \mathbf{M}_h$.*

Proof. We proceed as in the proof of Theorem 4.1.1. The inf-sup condition (4.18) is not affected by the quadrature (in particular the commutativity property (4.9) holds). Therefore, it suffices to prove coercivity of $(\cdot, \mathbf{k}^{-1}\cdot)_Q$ in \mathbf{Z}_h , that is,

$$(\mathbf{v}, \mathbf{k}^{-1}\mathbf{v})_Q \geq c\|\mathbf{v}\|_{H(\text{div},\Omega)}^2 \quad \forall \mathbf{v} \in \mathbf{Z}_h, \quad (4.25)$$

which is established as in the proof of Theorem 4.1.1, simply replacing condition (4.20) by the lower bound in (3.32). \square

4.2.2 Preliminary results

First, we introduce the lowest order Raviart–Thomas–Nedelec space [58; 63] directly on a rectangular parallelepiped in physical space,

$$\mathbf{RTN}^0(K) = \mathbf{Q}_0(K) + \mathbf{x}Q_0(K), \quad (4.26)$$

and the associated projection $\mathbf{\Pi}_K^0 : \mathbf{H}^1(K) \rightarrow \mathbf{RTN}^0(K)$ such that

$$\langle (\mathbf{v} - \mathbf{\Pi}_K^0 \mathbf{v}) \cdot \mathbf{n}_f, q \rangle_f = 0, \quad \forall q \in P_0(f). \quad (4.27)$$

We naturally extend $\mathbf{RTN}^0(K)$ and $\mathbf{\Pi}_K^0$ to Ω :

$$\mathbf{RTN}_h^0 := \{ \mathbf{v} \in \mathbf{H}_{0,N}(\text{div}, \Omega) : \mathbf{v}|_K \in \mathbf{RTN}^0(K) \ \forall K \in \mathcal{T}_h \} \quad (4.28)$$

$$\mathbf{\Pi}_h^0 : \mathbf{H}^1(\Omega) \rightarrow \mathbf{RTN}_h^0 \quad \text{with } \mathbf{\Pi}_h^0|_{\mathbf{H}^1(K)} = \mathbf{\Pi}_K^0. \quad (4.29)$$

We recall the continuity of $\mathbf{\Pi}_h^0$,

$$\| \mathbf{\Pi}_h^0 \mathbf{v} \|_{L^2(\Omega)} \leq C \| \mathbf{v} \|_{L^2(\Omega)}, \quad (4.30)$$

the approximation property,

$$\| \mathbf{v} - \mathbf{\Pi}_h^0 \mathbf{v} \|_{L^2(\Omega)} \leq Ch \| \mathbf{v} \|_{\mathbf{H}^1(\Omega)}, \quad (4.31)$$

and a commutativity property, similar to that of Equation (3.24),

$$(\text{div}(\mathbf{v} - \mathbf{\Pi}_h^0 \mathbf{v}), q)_K = 0 \quad \forall q \in P_0(K). \quad (4.32)$$

We now prove several lemmas that will be used in the next subsection to establish convergence of the cell-centered finite difference method.

Lemma 4.2.2. $(\mathbf{v} - \mathbf{\Pi}_K^0 \mathbf{v}, \mathbf{v}_0)_{Q,K} = 0, \quad \forall \mathbf{v} \in \mathbf{V}(K), \ \forall \mathbf{v}_0 \in \mathbf{P}_0(K).$

Proof. It suffices to prove the assertion for $\mathbf{v}_0 = (1, 0, 0)^t$ on the reference element,

and the lemma will follow by symmetry. Let $\mathbf{v}_0 = (1, 0, 0)^t$, we have

$$\begin{aligned} (\mathbf{v} - \mathbf{\Pi}_K^0 \mathbf{v}, \mathbf{v}_0)_{Q,K} &= \langle (\mathbf{v} - \mathbf{\Pi}_K^0 \mathbf{v}) \cdot \mathbf{n}_{x=-1}, -1 \rangle_{x=-1} \\ &\quad + \langle (\mathbf{v} - \mathbf{\Pi}_K^0 \mathbf{v}) \cdot \mathbf{n}_{x=1}, 1 \rangle_{x=1} \end{aligned} \quad (4.33)$$

since \mathbf{v}_0 is normal to all but the two faces $x = -1$ and $x = 1$. Both face integrals on the right hand side of (4.33) vanish from the definition of $\mathbf{\Pi}_K^0$ in (4.27). \square

Lemma 4.2.3. $\|\mathbf{\Pi}_K \mathbf{v}\|_{H^1(K)} \leq C \|\mathbf{v}\|_{H^1(K)}, \quad \forall \mathbf{v} \in \mathbf{H}^1(K).$

Proof. We introduce $\bar{\mathbf{v}}$, the projection of \mathbf{v} onto the space of constant vectors $\mathbf{P}_0(K)$.

We have

$$\begin{aligned} |\mathbf{\Pi}_K \mathbf{v}|_{H^1(K)} &= |\mathbf{\Pi}_K \mathbf{v} - \bar{\mathbf{v}}|_{H^1(K)} \\ &\leq \|\mathbf{\Pi}_K \mathbf{v} - \bar{\mathbf{v}}\|_{H^1(K)} \\ &\leq Ch^{-1} \|\mathbf{\Pi}_K \mathbf{v} - \bar{\mathbf{v}}\|_{L^2(K)} \quad (\text{inverse inequality}) \\ &\leq Ch^{-1} (\|\mathbf{\Pi}_K \mathbf{v} - \mathbf{v}\|_{L^2(K)} + \|\mathbf{v} - \bar{\mathbf{v}}\|_{L^2(K)}) \\ &\leq C \|\mathbf{v}\|_{H^1(K)} \quad (\text{approximation property}) \end{aligned} \quad (4.34)$$

where we have used the inverse estimate (4.22) and the approximation property (4.1).

We now finish the proof:

$$\begin{aligned} \|\mathbf{\Pi}_K \mathbf{v}\|_{H^1(K)} &\leq \|\mathbf{\Pi}_K \mathbf{v}\|_{L^2(K)} + |\mathbf{\Pi}_K \mathbf{v}|_{H^1(K)} \\ &\leq \|\mathbf{\Pi}_K \mathbf{v} - \mathbf{v}\|_{L^2(K)} + \|\mathbf{v}\|_{L^2(K)} + |\mathbf{\Pi}_K \mathbf{v}|_{H^1(K)} \\ &\leq C \|\mathbf{v}\|_{H^1(K)}, \end{aligned} \quad (4.35)$$

where we have used the approximation property (4.1) and the bound (4.34) in the last inequality. \square

Lemma 4.2.4. *Assume that $\mathbf{k}^{-1} \in W_\infty^1(\mathcal{T}_h)$, that is, $\mathbf{k}^{-1} \in W_\infty^1(K)$ in each element K . Then*

$$|(\mathbf{v} - \mathbf{\Pi}_h^0 \mathbf{v}, \mathbf{k}^{-1} \mathbf{\Pi}_h \mathbf{u})_Q| \leq Ch \|\mathbf{u}\|_{H^1(\Omega)} \|\mathbf{v}\|_{L^2(\Omega)} \quad \forall \mathbf{v} \in \mathbf{V}_h. \quad (4.36)$$

Proof. On any element K , we express:

$$\begin{aligned} (\mathbf{v} - \mathbf{\Pi}_K^0 \mathbf{v}, \mathbf{k}^{-1} \mathbf{\Pi}_K \mathbf{u})_{Q,K} &= (\mathbf{v} - \mathbf{\Pi}_K^0 \mathbf{v}, (\mathbf{k}^{-1} - \overline{\mathbf{k}^{-1}}) \mathbf{\Pi}_K \mathbf{u})_{Q,K} \\ &\quad + (\mathbf{v} - \mathbf{\Pi}_K^0 \mathbf{v}, \overline{\mathbf{k}^{-1}} \mathbf{\Pi}_K \mathbf{u})_{Q,K}. \end{aligned} \quad (4.37)$$

The first term on the right-hand-side of (4.37) can be bounded using Taylor expansion and the equivalence of $(\cdot, \mathbf{k}^{-1} \cdot)_{Q,K}^{1/2}$ and $\|\cdot\|_{L^2(K)}$:

$$\begin{aligned} &(\mathbf{v} - \mathbf{\Pi}_K^0 \mathbf{v}, (\mathbf{k}^{-1} - \overline{\mathbf{k}^{-1}}) \mathbf{\Pi}_K \mathbf{u})_{Q,K} \\ &\leq Ch \|\mathbf{k}^{-1}\|_{W_\infty^1(K)} \|\mathbf{\Pi}_K \mathbf{u}\|_{L^2(K)} \|\mathbf{v} - \mathbf{\Pi}_K^0 \mathbf{v}\|_{L^2(K)} \\ &\leq Ch \|\mathbf{k}^{-1}\|_{W_\infty^1(K)} \|\mathbf{u}\|_{L^2(K)} \|\mathbf{v} - \mathbf{\Pi}_K^0 \mathbf{v}\|_{L^2(K)} \quad (\text{continuity of } \mathbf{\Pi}_K) \\ &\leq Ch^2 \|\mathbf{k}^{-1}\|_{W_\infty^1(K)} \|\mathbf{u}\|_{L^2(K)} \|\mathbf{v}\|_{H^1(K)} \quad (\text{approximation property}) \\ &\leq Ch \|\mathbf{k}^{-1}\|_{W_\infty^1(K)} \|\mathbf{u}\|_{L^2(K)} \|\mathbf{v}\|_{L^2(K)} \quad (\text{inverse estimate}). \end{aligned} \quad (4.38)$$

From Lemma 4.2.2, the last term of (4.37) is:

$$\begin{aligned} &(\mathbf{v} - \mathbf{\Pi}_K^0 \mathbf{v}, \mathbf{k}^{-1} \mathbf{\Pi}_K \mathbf{u})_{Q,K} \\ &= (\mathbf{v} - \mathbf{\Pi}_K^0 \mathbf{v}, \mathbf{k}^{-1} (\mathbf{\Pi}_K \mathbf{u} - \overline{\mathbf{\Pi}_K \mathbf{u}}))_{Q,K} \\ &\leq Ch \|\mathbf{k}^{-1}\|_{W_\infty^0(K)} \|\mathbf{\Pi}_K \mathbf{u} - \overline{\mathbf{\Pi}_K \mathbf{u}}\|_{L^2(K)} \|\mathbf{v} - \mathbf{\Pi}_K^0 \mathbf{v}\|_{L^2(K)} \\ &\leq Ch^2 \|\mathbf{k}^{-1}\|_{W_\infty^0(K)} \|\mathbf{\Pi}_K \mathbf{u}\|_{H^1(K)} \|\mathbf{v}\|_{H^1(K)} \quad (\text{approximation property}) \\ &\leq Ch^2 \|\mathbf{k}^{-1}\|_{W_\infty^0(K)} \|\mathbf{u}\|_{H^1(K)} \|\mathbf{v}\|_{H^1(K)} \quad (\text{Lemma 4.2.3}) \\ &\leq Ch \|\mathbf{k}^{-1}\|_{W_\infty^0(K)} \|\mathbf{u}\|_{H^1(K)} \|\mathbf{v}\|_{L^2(K)} \quad (\text{inverse estimate}). \end{aligned} \quad (4.39)$$

Combining (4.38) and (4.39), and summing over all elements, leads to the global bound in the lemma. \square

Definition 4.2.5. The global quadrature error for the bilinear form $(\cdot, \mathbf{k}^{-1}\cdot)$ is:

$$\begin{aligned} E_Q(\mathbf{v}, \mathbf{k}^{-1}\mathbf{u}) &= \sum_{K \in \mathcal{T}_h} E_{Q,K}(\mathbf{v}, \mathbf{k}^{-1}\mathbf{u}) \\ &= \sum_{K \in \mathcal{T}_h} ((\mathbf{v}, \mathbf{k}^{-1}\mathbf{u})_K - (\mathbf{v}, \mathbf{k}^{-1}\mathbf{u})_{Q,K}). \end{aligned} \quad (4.40)$$

Lemma 4.2.6. Let $\mathbf{v} \in \mathbf{V}_h$, $\mathbf{v}_0 \in \mathbf{RTN}_h^0$, and $\mathbf{k}^{-1} \in W_\infty^1(\mathcal{T}_h)$. The error introduced by the quadrature rule is bounded:

$$|E_Q(\mathbf{v}_0, \mathbf{k}^{-1}\mathbf{v})| \leq Ch \|\mathbf{v}\|_{H^1(\Omega)} \|\mathbf{v}_0\|_{L^2(\Omega)}. \quad (4.41)$$

Proof. The trapezoidal quadrature is a Newton–Cotes type quadrature, well-known to be exact for functions in $Q_1(K)$. Let $\bar{\mathbf{v}}$ be the projection of \mathbf{v} onto $\mathbf{P}_0(K)$, the space of constant vectors on each element. Similarly, let $\overline{\mathbf{k}^{-1}}$ be the cell-wise average of \mathbf{k}^{-1} . On any element K , we express the quadrature error as:

$$\begin{aligned} E_{Q,K}(\mathbf{v}, \mathbf{k}^{-1}\mathbf{u}) &= E_{Q,K}(\mathbf{v}, (\mathbf{k}^{-1} - \overline{\mathbf{k}^{-1}})\mathbf{u}) \\ &\quad + E_{Q,K}(\mathbf{v}, \overline{\mathbf{k}^{-1}}(\mathbf{u} - \bar{\mathbf{u}})) + E_{Q,K}(\mathbf{v}, \overline{\mathbf{k}^{-1}}\bar{\mathbf{u}}). \end{aligned} \quad (4.42)$$

The last term in (4.42) is identically zero, because the trapezoidal rule is exact for linear functions. Using Taylor expansion, we bound the first term on the right-hand-side of (4.42):

$$|E_{Q,K}(\mathbf{v}, (\mathbf{k}^{-1} - \overline{\mathbf{k}^{-1}})\mathbf{u})| \leq Ch |\mathbf{k}^{-1}|_{W_\infty^1(K)} \|\mathbf{v}\|_{L^2(K)} \|\mathbf{v}_0\|_{L^2(K)}. \quad (4.43)$$

An application of the Bramble–Hilbert lemma [13; 31] allows us to bound the second

term:

$$|E_{Q,K}(\mathbf{v}, \overline{\mathbf{k}^{-1}}(\mathbf{u} - \bar{\mathbf{u}}))| \leq Ch \|\mathbf{k}^{-1}\|_{W_\infty^0(K)} \|\mathbf{v}\|_{H^1(K)} \|\mathbf{v}_0\|_{L^2(K)}. \quad (4.44)$$

Combining (4.43) and (4.44) we obtain

$$|E_{Q,K}(\mathbf{v}, \mathbf{k}^{-1}\mathbf{u})| \leq Ch \|\mathbf{k}^{-1}\|_{W_\infty^1(K)} \|\mathbf{v}\|_{H^1(K)} \|\mathbf{v}_0\|_{L^2(K)}. \quad (4.45)$$

Summing over all elements completes the proof. \square

4.2.3 Velocity error analysis

From the variational formulation of the continuous problem of Equations (2.10)–(2.11) and the localized mixed finite element method of Equations (3.33)–(3.34), we obtain the system of error equations:

$$(\mathbf{v}, \mathbf{k}^{-1}\mathbf{u}) - (\mathbf{v}, \mathbf{k}^{-1}\tilde{\mathbf{u}}_h)_Q = (\operatorname{div}\mathbf{v}, p - \tilde{p}_h) \quad \forall \mathbf{v} \in \mathbf{V}_h, \quad (4.46)$$

$$(q, \operatorname{div}(\mathbf{u} - \tilde{\mathbf{u}}_h)) = 0 \quad \forall q \in W_h. \quad (4.47)$$

We can simplify (4.47) using Equation (3.24) to obtain

$$(q, \operatorname{div}(\mathbf{\Pi}_h\mathbf{u} - \tilde{\mathbf{u}}_h)) = 0 \quad \forall q \in W_h. \quad (4.48)$$

Since $(\mathbf{\Pi}_h\mathbf{u} - \tilde{\mathbf{u}}_h) \in \mathbf{V}_h$ and $\operatorname{div}\mathbf{V}_h = W_h$, we take $q = \operatorname{div}(\mathbf{\Pi}_h\mathbf{u} - \tilde{\mathbf{u}}_h)$ in (4.48), which yields

$$\operatorname{div}(\mathbf{\Pi}_h\mathbf{u} - \tilde{\mathbf{u}}_h) = 0. \quad (4.49)$$

We now rewrite (4.46) by introducing $\mathbf{\Pi}_h \mathbf{u}$ and $P_h p$, the projections of the continuous solution onto the subspaces \mathbf{V}_h and W_h ,

$$\begin{aligned} (\mathbf{v}, \mathbf{k}^{-1}(\mathbf{\Pi}_h \mathbf{u} - \tilde{\mathbf{u}}_h))_Q &= (\mathbf{v}, \mathbf{k}^{-1} \mathbf{\Pi}_h \mathbf{u})_Q - (\mathbf{v}, \mathbf{k}^{-1} \mathbf{u}) \\ &\quad + (\operatorname{div} \mathbf{v}, P_h p - \tilde{p}_h), \end{aligned} \quad (4.50)$$

where we have also used the fundamental property of the projection P_h in Equation (3.17). We expand the first two terms of the right-hand-side of (4.50) using the projection operator onto \mathbf{RTN}_h^0 :

$$\begin{aligned} &(\mathbf{v}, \mathbf{k}^{-1} \mathbf{\Pi}_h \mathbf{u})_Q - (\mathbf{v}, \mathbf{k}^{-1} \mathbf{u}) \\ &= (\mathbf{v} - \mathbf{\Pi}_h^0 \mathbf{v}, \mathbf{k}^{-1} \mathbf{\Pi}_h \mathbf{u})_Q + (\mathbf{\Pi}_h^0 \mathbf{v}, \mathbf{k}^{-1} \mathbf{\Pi}_h \mathbf{u})_Q - (\mathbf{\Pi}_h^0 \mathbf{v}, \mathbf{k}^{-1} \mathbf{\Pi}_h \mathbf{u}) \\ &\quad - (\mathbf{v} - \mathbf{\Pi}_h^0 \mathbf{v}, \mathbf{k}^{-1} \mathbf{u}) - (\mathbf{\Pi}_h^0 \mathbf{v}, \mathbf{k}^{-1} (\mathbf{u} - \mathbf{\Pi}_h \mathbf{u})). \end{aligned} \quad (4.51)$$

The first term on the right-hand-side of (4.51) is bounded by Lemma 4.2.4. The second and third terms were bounded in Lemma 4.2.6. Using $\mathbf{v} - \mathbf{\Pi}_h^0 \mathbf{v}$ as the test function in the continuous variational Equation (2.10), we rewrite the third term on the right-hand-side of (4.51) as

$$(\mathbf{v} - \mathbf{\Pi}_h^0 \mathbf{v}, \mathbf{k}^{-1} \mathbf{u}) = (\operatorname{div}(\mathbf{v} - \mathbf{\Pi}_h^0 \mathbf{v}), p) - \langle (\mathbf{v} - \mathbf{\Pi}_h^0 \mathbf{v}) \cdot \mathbf{n}, \bar{p} \rangle_{\Gamma_D}. \quad (4.52)$$

The first term on the right-hand-side of (4.52) vanishes by (4.32). Assuming smooth enough boundary conditions \bar{p} , the last term of (4.52) is zero by definition of the \mathbf{RTN}_0 degrees of freedom (Equation (4.27)), yielding

$$(\mathbf{v} - \mathbf{\Pi}_h^0 \mathbf{v}, \mathbf{k}^{-1} \mathbf{u}) = 0. \quad (4.53)$$

The last term on the right-hand-side of (4.51) is bounded by

$$\begin{aligned}
& |(\mathbf{\Pi}_h^0 \mathbf{v}, \mathbf{k}^{-1}(\mathbf{u} - \mathbf{\Pi}_h \mathbf{u}))| \\
& \leq \|\mathbf{k}^{-1}\|_{W_\infty^0(\mathcal{T}_h)} \|\mathbf{\Pi}_h^0 \mathbf{v}\|_{L^2(\Omega)} \|(\mathbf{u} - \mathbf{\Pi}_h \mathbf{u})\|_{L^2(\Omega)} \\
& \leq C \|\mathbf{k}^{-1}\|_{W_\infty^0(\mathcal{T}_h)} \|\mathbf{v}\|_{L^2(\Omega)} \|\mathbf{u} - \mathbf{\Pi}_h \mathbf{u}\|_{L^2(\Omega)} \\
& \leq Ch \|\mathbf{k}^{-1}\|_{W_\infty^0(\mathcal{T}_h)} \|\mathbf{v}\|_{L^2(\Omega)} \|\mathbf{u}\|_{H^1(\Omega)},
\end{aligned} \tag{4.54}$$

where we have used the fact that \mathbf{k} is uniformly bounded, the continuity of $\mathbf{\Pi}_h^0$ as expressed in (4.30), and the approximation property (4.10). Combining Equations (4.52)–(4.54), we bound (4.51) by

$$|(\mathbf{v}, \mathbf{k}^{-1} \mathbf{\Pi}_h \mathbf{u})_Q - (\mathbf{v}, \mathbf{k}^{-1} \mathbf{u})| \leq Ch \|\mathbf{v}\|_{L^2(\Omega)} \|\mathbf{u}\|_{H^1(\Omega)}. \tag{4.55}$$

We now take $\mathbf{v} = \mathbf{\Pi}_h \mathbf{u} - \tilde{\mathbf{u}}_h$ as a test function and bound (4.50) using (4.55) and (4.49):

$$|(\mathbf{\Pi}_h \mathbf{u} - \tilde{\mathbf{u}}_h, \mathbf{k}^{-1}(\mathbf{\Pi}_h \mathbf{u} - \tilde{\mathbf{u}}_h))_Q| \leq Ch \|\mathbf{\Pi}_h \mathbf{u} - \tilde{\mathbf{u}}_h\|_{L^2(\Omega)} \|\mathbf{u}\|_{H^1(\Omega)}. \tag{4.56}$$

The equivalence between the two norms $(\cdot, \mathbf{k}^{-1} \cdot)_Q^{1/2}$ and $\|\cdot\|_{L^2(\Omega)}$ yields

$$\|\mathbf{\Pi}_h \mathbf{u} - \tilde{\mathbf{u}}_h\|_{L^2(\Omega)} \leq Ch \|\mathbf{u}\|_{H^1(\Omega)}. \tag{4.57}$$

We can now establish error bounds on the velocity and its divergence for the cell-centered finite difference method.

Theorem 4.2.7. *The cell-centered finite difference method, equivalent to the MPFA*

O-method, admits a first order convergence for the velocity and its divergence:

$$\|\mathbf{u} - \tilde{\mathbf{u}}_h\|_{L^2(\Omega)} \leq Ch\|\mathbf{u}\|_{H^1(\Omega)}, \quad (4.58)$$

$$\|\operatorname{div}(\mathbf{u} - \tilde{\mathbf{u}}_h)\|_{L^2(\Omega)} \leq Ch\|\operatorname{div}\mathbf{u}\|_{H^1(\Omega)}. \quad (4.59)$$

Proof. The approximation property (4.10) and the bound (4.57) yields immediately (4.58).

The property (4.49), combined with the approximation property (4.11), proves (4.59). \square

4.2.4 Pressure error analysis

Theorem 4.2.8. *The cell-centered finite difference method, equivalent to the MPFA O-method, admits a first order convergence for the pressure:*

$$\|p - \tilde{p}_h\|_{L^2(\Omega)} \leq Ch(\|\mathbf{u}\|_{H^1(\Omega)} + \|p\|_{H^1(\Omega)}). \quad (4.60)$$

Proof. It is well-known that the Raviart–Thomas–Nedelec space satisfies the inf-sup condition (4.18) [17; 58]. Taking $q = P_h p - \tilde{p}_h$ in Equation (4.18), we obtain

$$\|P_h p - \tilde{p}_h\|_{L^2(\Omega)} \leq C \sup_{\mathbf{v} \in \mathbf{RTN}_h^0} \frac{(\operatorname{div}\mathbf{v}, P_h p - \tilde{p}_h)}{\|\mathbf{v}\|_{H(\operatorname{div}, \Omega)}}. \quad (4.61)$$

From Equation (4.50) we can write

$$\begin{aligned} (\operatorname{div}\mathbf{v}, P_h p - \tilde{p}_h) &= (\mathbf{v}, \mathbf{k}^{-1}(\mathbf{\Pi}_h \mathbf{u} - \tilde{\mathbf{u}}_h))_Q - (\mathbf{v}, \mathbf{k}^{-1} \mathbf{\Pi}_h \mathbf{u})_Q \\ &\quad + (\mathbf{v}, \mathbf{k}^{-1} \mathbf{u}) \end{aligned} \quad (4.62)$$

$$\begin{aligned} &= (\mathbf{v}, \mathbf{k}^{-1}(\mathbf{\Pi}_h \mathbf{u} - \tilde{\mathbf{u}}_h))_Q - (\mathbf{v}, \mathbf{k}^{-1} \mathbf{\Pi}_h \mathbf{u})_Q \\ &\quad + (\mathbf{v}, \mathbf{k}^{-1} \mathbf{\Pi}_h \mathbf{u}) + (\mathbf{v}, \mathbf{k}^{-1}(\mathbf{u} - \mathbf{\Pi}_h \mathbf{u})). \end{aligned} \quad (4.63)$$

We now use Lemma 4.2.6 to bound the second and third terms on the right-hand-side

of (4.63). The first term is bounded by (4.57) and the last term by (4.10), to obtain

$$\|P_h p - \tilde{p}_h\|_{L^2(\Omega)} \leq Ch \|\mathbf{u}\|_{H^1(\Omega)}. \quad (4.64)$$

Using the approximation property (4.12) and the triangle inequality in (4.64) concludes the proof. \square

4.3 Numerical experiments

We now confirm numerically the error estimates of the previous sections. Let $\Omega = [0, 1] \times [0, 1] \times [0, 1]$. We introduce the diagonal tensors

$$\mathbf{k}_1^\perp = \begin{pmatrix} 3 & 0 & 0 \\ 0 & 2 & 0 \\ 0 & 0 & 1 \end{pmatrix}, \quad (4.65)$$

$$\mathbf{k}_2^\perp = \begin{pmatrix} 3x+1 & 0 & 0 \\ 0 & 2y+1 & 0 \\ 0 & 0 & z+1 \end{pmatrix}, \quad (4.66)$$

and the full-tensor permeability fields \mathbf{k}_1 and \mathbf{k}_2 defined as the rotations of \mathbf{k}_1^\perp and \mathbf{k}_2^\perp by 15° , 30° and 45° around the x -, y - and z -axis, respectively. To fix ideas, we have

$$\mathbf{k}_1 \approx \begin{pmatrix} 2.0999 & 0.2919 & -0.7450 \\ 0.2919 & 2.3499 & -0.4388 \\ -0.7450 & -0.4388 & 1.5502 \end{pmatrix}. \quad (4.67)$$

We define two test cases by associating the permeability fields \mathbf{k}_1 and \mathbf{k}_2 to the

two pressure solutions p_1 and p_2 , with

$$p_1(x, y, z) = (x - x^2)(y - y^2)(z - z^2), \quad (4.68)$$

$$p_2(x, y, z) = \sin(\pi x) \sin(\pi y) \sin(\pi z). \quad (4.69)$$

We partition the domain Ω into Cartesian grids with different levels of refinement (from a $2 \times 2 \times 2$ grid to a $16 \times 16 \times 16$ grid). We impose Dirichlet boundary conditions on $\partial\Omega$, with prescribed pressures from the true solutions (4.68) and (4.69). We analyze convergence of the mixed finite element method based on the new velocity space MJT, as well as its localization into the MPFA O-method using the trapezoidal quadrature. For comparison, we also provide the numerical convergence results for the mixed finite element method with the RTN_0 and BDM_1 spaces. The numerical errors and convergence rates for the pressure, velocity and velocity divergence in the $L^2(\Omega)$ norm are reported in Tables 4.1 and 4.2 for test case 1 and 2, respectively. Clearly, the numerical experiments confirm the theoretical estimates.

Remark 4.3.1. The numerical error for the divergence of the velocity is the same for all the discretization methods considered. Equation (2.13) implies

$$\operatorname{div} \mathbf{u}_h = P_h f. \quad (4.70)$$

We also have, for the continuous solution,

$$\operatorname{div} \mathbf{u} = f. \quad (4.71)$$

Therefore

$$\|\operatorname{div}(\mathbf{u}_h - \mathbf{u})\|_{L^2(\Omega)} = \|P_h f - f\|_{L^2(\Omega)}, \quad (4.72)$$

which is the same for all four discretizations considered, since they have the same

Table 4.1. Error values and convergence rates for the first example.

Method	$1/h$	$\ p - p_h\ _{L^2}$	$\ \mathbf{u} - \mathbf{u}_h\ _{L^2}$	$\ \operatorname{div}(\mathbf{u} - \mathbf{u}_h)\ _{L^2}$	$ p - p_h $
RTN ₀	2	3.977E-03	4.061E-02	1.947E-01	1.827E-03
	4	2.293E-03	2.261E-02	1.080E-01	4.558E-04
	8	1.188E-03	1.159E-02	5.535E-02	1.151E-04
	16	5.996E-04	5.833E-03	2.785E-02	2.889E-05
	rate	0.987	0.991	0.991	1.995
BDM ₁	2	4.094E-03	2.741E-02	1.947E-01	3.031E-03
	4	2.343E-03	8.729E-03	1.080E-01	9.933E-04
	8	1.197E-03	2.325E-03	5.535E-02	2.709E-04
	16	6.008E-04	5.907E-04	2.785E-02	6.931E-05
	rate	0.995	1.977	0.991	1.967
MJT	2	4.111E-03	2.640E-02	1.947E-01	3.095E-03
	4	2.346E-03	8.118E-03	1.080E-01	1.006E-03
	8	1.197E-03	2.138E-03	5.535E-02	2.720E-04
	16	6.008E-04	5.416E-04	2.785E-02	6.938E-05
	rate	0.995	1.981	0.991	1.971
MPFA	2	4.688E-03	3.853E-02	1.947E-01	1.068E-03
	4	2.423E-03	2.096E-02	1.080E-01	4.559E-04
	8	1.208E-03	1.049E-02	5.535E-02	1.363E-04
	16	6.021E-04	5.226E-03	2.785E-02	3.587E-05
	rate	1.004	1.005	0.991	1.926

pressure space W_h .

Remark 4.3.2. The numerical results indicate superconvergence of the pressure. This is well known for the RTN₀ and BDM₁ spaces [15], and here we show that it is true for the new mixed finite element space and for its localized cell-centered version. We define the norm $|||\cdot|||$ based on the difference between the analytical solution and the numerical solution at the center of each element. To be precise:

$$|||p - p_h||| = \left(\sum_{K \in \mathcal{T}_h} |K| (p(\mathbf{x}_{0,K}) - p_h(K))^2 \right)^{1/2}, \quad (4.73)$$

where $\mathbf{x}_{0,K}$ is the center of element K . In Tables 4.1 and 4.2 we show that the convergence rate for $|||p - p_h|||$ is of $O(h^2)$.

Table 4.2. Error values and convergence rates for the second example.

Method	$1/h$	$\ p - p_h\ _{L^2}$	$\ \mathbf{u} - \mathbf{u}_h\ _{L^2}$	$\ \operatorname{div}(\mathbf{u} - \mathbf{u}_h)\ _{L^2}$	$\ p - p_h\ $
RTN ₀	2	2.450E-01	2.540E+00	1.533E+01	1.316E-01
	4	1.348E-01	1.325E+00	8.549E+00	4.016E-02
	8	6.893E-02	6.665E-01	4.398E+00	1.054E-02
	16	3.465E-02	3.336E-01	2.215E+00	2.669E-03
	rate	0.992	0.998	0.990	1.982
BDM ₁	2	2.590E-01	2.129E+00	1.533E+01	1.884E-01
	4	1.410E-01	6.859E-01	8.549E+00	7.019E-02
	8	6.998E-02	1.832E-01	4.398E+00	1.956E-02
	16	3.479E-02	4.658E-02	2.215E+00	5.026E-03
	rate	1.008	1.976	0.990	1.960
MJT	2	2.601E-01	2.105E+00	1.533E+01	1.913E-01
	4	1.412E-01	6.642E-01	8.549E+00	7.088E-02
	8	6.999E-02	1.760E-01	4.398E+00	1.961E-02
	16	3.479E-02	4.466E-02	2.215E+00	5.030E-03
	rate	1.008	1.979	0.990	1.963
MPFA	2	2.538E-01	2.495E+00	1.533E+01	5.223E-02
	4	1.364E-01	1.254E+00	8.549E+00	1.841E-02
	8	6.913E-02	6.179E-01	4.398E+00	5.103E-03
	16	3.468E-02	3.072E-01	2.215E+00	1.319E-03
	rate	0.995	1.008	0.990	1.952

Chapter 5

A new framework for streamline tracing

In this chapter, we exploit the MFE framework to propose a new streamline tracing algorithm for general triangular, quadrilateral, tetrahedral and hexahedral grids populated with tensor permeability coefficients. MFE methods provide a natural tracing algorithm: the streamlines are integrated from the velocity field which is reconstructed by interpolation of the flux degrees of freedom with the velocity shape functions.

For FV discretizations, we make use of the established links with MFE methods. The velocity field is thus reconstructed by interpolation of the FV fluxes with the MFE velocity shape functions. This new approach provides a natural way of reconstructing velocity fields from TPFA or MPFA fluxes. We thereby justify mathematically the current tracing methods in use for finite difference [60] or TPFA [26] discretizations. For MPFA, the new algorithm generates more accurate streamlines than existing methods and avoids the flux post-processing techniques on which they rely [38; 62].

5.1 Streamline tracing for MFE discretizations

5.1.1 General strategy

Our streamline tracing algorithm is based on a particle-tracking concept. A streamline is traced by following the movement of a fluid particle in time. Since the mixed finite element method provides a velocity field defined elementwise and not globally, it is therefore natural to trace streamlines by segments, each segment corresponding to an underlying element of the simulation grid. The streamline tracing procedure may be summarized as follows [51]:

- Start at a *launching* point (\mathbf{x}_0, t_0) in the simulation domain Ω . This defines the location (in space and time) of the fluid particle that will be followed to trace the streamline.
- Determine in what element the launching point lies. The tracing will start within this element.
- Trace the streamline downstream towards a sink. The fluid particle is followed forward in time. In each element crossed by the streamline:
 - Trace the streamline downstream from the point of entry in the element.
 - Store the exit point and corresponding time-of-flight.
 - Move on to the next downstream element until a sink (element with a production well) or an outflow boundary is reached.
- Trace the streamline upstream, towards a source. The fluid particle is followed backwards in time. In each element crossed:
 - Trace the streamline upstream from the entry point in the element.
 - Store the exit point and time-of-flight.

- Move on to the next upstream element until a source (element with an injection well) or an inflow boundary is reached.

5.1.2 Tracing in the reference space

Most streamline tracing methods share the particle tracking approach described above. They usually differ in the procedure chosen to integrate the streamline within each element. For example, for low-order accurate methods on general triangular or rectangular elements, an analytical integration of the streamline path is possible [26; 60]. When rectangular elements are distorted into general quadrilaterals, the Jacobian of the coordinate mapping is not constant over the element and the analytical integration of the streamline is not possible in physical space. Moreover, in the case of higher-order discretizations, the enrichment of the velocity fields prevents the decoupling between the x - and y -components of the velocity used by Pollock to obtain an analytical integration [60].

Because we are interested in tracing streamlines on distorted grids, we propose to perform the tracing in the reference space and then map the solution to the physical space. Two main reasons drive this choice. First, the velocity field and stream function are known analytically on the reference element. Second, working on the reference element permits a more elegant and efficient implementation of the tracing algorithm.

To trace streamlines in the reference element, we recall that two mappings need to be used: the isoparametric mapping of (2.26) for the coordinates, and the Piola transform of (2.27) for the velocity. The general procedure to trace a streamline within an element starts with the mapping of the entry point from the physical space to the reference space. Then, the streamline is integrated and the exit point found in the reference space. The exit point is finally mapped back to the physical space and stored.

Two approaches are possible to obtain the exit point of a streamline in an element: an algebraic formulation using the stream function, and a numerical integration using a Runge-Kutta-type method.

5.1.3 Integration of the streamline path

Stream function approach

In two dimensions, we can use the stream functions derived in [41] for the RTN_0 and BDM_1 spaces. Using the fundamental property that the stream function is constant along a streamline, we can write the path of the streamline that passes through a point (\hat{x}_0, \hat{y}_0) :

$$\Psi(\hat{x}, \hat{y}) = \Psi(\hat{x}_0, \hat{y}_0), \quad \forall (\hat{x}, \hat{y}) \in \text{streamline}. \quad (5.1)$$

This approach simplifies the tracing from the solution of an ordinary differential equation to that of an algebraic equation. Since the stream function has an analytical expression, the streamline path is known analytically and an efficient Newton method can be used to solve the algebraic equation for the exit point up to machine precision.

Depending on the functional form of the stream function, (5.1) may lead to multiple solutions on the boundary of a given element. This situation cannot be encountered when using an RTN_0 discretization, but it is not uncommon for BDM_1 velocity fields. This situation occurs when a streamline enters and exit an element several times. To find the real exit point among the solutions of the streamline equation, the time-of-flight is computed for each potential exit location. The correct exit point is the solution that yields the smallest positive time-of-flight.

Numerical integration approach

A more general approach to obtain the streamline path is to use numerical integration in time. This approach is valid in two and three dimensions. Because the velocity

field is known analytically, an efficient numerical integration is possible by solving an initial value problem for the streamline location $\hat{\mathbf{x}}$ on the reference element:

$$\frac{d\hat{\mathbf{x}}}{d\hat{t}} = \hat{\mathbf{u}}(\hat{\mathbf{x}}), \quad \hat{\mathbf{x}}(\hat{t} = \hat{t}_0) = \hat{\mathbf{x}}_0. \quad (5.2)$$

In our implementation, we used an explicit Runge–Kutta method of fourth order [30], which proved to be efficient and robust.

5.1.4 Time-of-flight computation

An integral form of (1.33) provides an expression of the time-of-flight τ along a streamline \mathcal{L} as a function of the arc length s :

$$\tau := \int_{\mathcal{L}} \frac{\phi}{|\mathbf{u}(s)|} ds. \quad (5.3)$$

In two cases only, the time-of-flight variable can be computed analytically. First, for the RTN_0 discretization on simplices, the velocity field is constant over each element; therefore, the streamline is a straight line and the time-of-flight computation is trivial. The second case is that of Pollock’s method [60] (that relies on an RTN_0 velocity field) on rectangular grids and in the presence of diagonal permeability tensors, where each component of the velocity field depends exclusively on its own coordinate: $u_x(x, y, z) = u_x(x)$, $u_y(x, y, z) = u_y(y)$ and $u_z(x, y, z) = u_z(z)$. This decoupling of the coordinates permits an analytical integration of the time-of-flight.

For general quadrilateral or hexahedral grids, and for higher-order velocity approximations, a numerical integration of the time-of-flight is necessary. For consistency with the rest of the streamline tracing framework, one must be able to evaluate the integral in (5.3) on the reference space. Using the Piola transform, we can express the reference velocity in terms of the physical one and recast the time-of-flight integration

in terms of the reference coordinates only [41]:

$$\tau = \int_{\hat{\mathcal{L}}} \frac{\phi}{|\hat{\mathbf{u}}(\hat{s})|} J(\hat{x}) \, d\hat{s}. \quad (5.4)$$

It is worthwhile noting that the coordinate mapping between the reference and physical spaces is affine for triangular and rectangular elements. In this case, the Jacobian is constant over the reference element and can be taken out of the integral in (5.4). For general quadrilateral elements, however, the Jacobian varies inside the element. Prévost *et al.* [62] used the value of the Jacobian at the center of the element as an approximation. Hægland [37] showed, however, that this choice may lead to erroneous results and recommends keeping the Jacobian inside the integral. This explains why the time-of-flight cannot be integrated analytically on general quadrilaterals even when a low-order approximation is employed.

In our implementation, the time-of-flight integral of (5.4) is computed using a quadrature rule when the stream function approach is used for the integration of the streamline path. When the streamline path is integrated numerically, the time-of-flight is computed within the Runge–Kutta stepping.

5.2 Streamline tracing for FV discretizations

5.2.1 A new approach

Our strategy to reconstruct the MPFA velocity fields is to interpret the total fluxes or the subfluxes provided by MPFA as MFE degrees of freedom. This approach is justified by the established equivalence between the finite volume and the mixed finite element methods. The shape functions of the MFE velocity spaces are used to interpolate the TPFA or MPFA fluxes and yield a continuous velocity field within the

control volume that is consistent with the discrete fluxes provided by the discretizations. The velocity fields so defined are guaranteed to be divergence-free, curl-free and to yield a stream function [41].

5.2.2 Low-Order Tracing

The RTN_0 space is used to reconstruct velocity fields defined by TPFA fluxes or the total MPFA fluxes. Since the RTN_0 degrees of freedom are defined as the total fluxes through element edges, we write the reconstructed velocity in the reference space as

$$\hat{\mathbf{v}}(\hat{\mathbf{x}}) = \sum_{j=1}^{n_f} F_j \mathbf{N}_j(\hat{\mathbf{x}}), \quad (5.5)$$

with n_f the number of faces per element, F_j the TPFA flux or the total MPFA flux through face j and \mathbf{N}_j the RTN_0 shape function corresponding to face j .

On rectangular grids populated with diagonal permeability tensors, we recover Pollock's method [60]. On general quadrilateral or hexahedral grids, with the coordinate mapping of (2.26) and the Piola transform of (2.27), we obtain the extension of Pollock's method to distorted grids proposed by Cordes and Kinzelbach [26]. We hereby provide a theoretical justification for these streamline tracing methods.

5.2.3 High-Order Tracing

To reconstruct a higher-order velocity field, the MPFA subfluxes are used. On two-dimensional triangular or quadrilateral elements and on three-dimensional tetrahedral elements, the BDM_1 space is used to interpolate the MPFA subfluxes. On three-dimensional hexahedral elements, the new velocity space MJT [52; 53] presented in

Chapter 3 is used. The reconstructed velocity field is obtained through

$$\hat{\mathbf{v}}(\hat{\mathbf{x}}) = \sum_{j=1}^{n_f} \sum_{i=1}^{n_{dof}} f_{j,i} \mathbf{N}_{j,i}(\hat{\mathbf{x}}), \quad (5.6)$$

where $f_{j,i}$ ($i = 1, \dots, n_{dof}$) are the MPFA subfluxes associated with face j . n_{dof} is the number of MPFA subfluxes defined per face. For two-dimensional grids, $n_{dof} = 2$, for the triangular faces of tetrahedra, $n_{dof} = 3$ and for the quadrilateral faces of hexahedra, $n_{dof} = 4$.

The idea of using the MPFA subfluxes in the velocity reconstruction was first introduced by Prévost *et al.* [62]. To trace streamlines, Prévost *et al.* proposed to divide each control volume into subcells, defined as the regions of the control volume delimited by the MPFA interaction regions. A flux post-processing technique was used to recover fluxes through the edges of the interaction regions. The streamlines were then traced on each subcell using the extension of Pollock's algorithm to distorted grids.

On hexahedral grids, Hægland *et al.* [38] proposed a streamline tracing algorithm based on a linear interpolation of the *corner velocities*. These corner velocities are obtained by a postprocessing of the MPFA subfluxes.

Using BDM₁ or MJT to trace streamlines offers three advantages over the approaches of Prévost *et al.* and Hægland *et al.*

- BDM₁ and MJT provide a velocity field with respectively linear and bilinear normal components on control-volume edges, which is clearly more accurate than the piecewise constant approximation obtained by Prévost *et al.*
- Although the MJT-based streamline tracing and the corner velocity interpolation method of Hægland *et al.* both have bilinear normal components on the faces of the hexahedra, the MJT velocity space provides a velocity field

within an element which is divergence free, which is, as we saw in Chapter 3, a necessary condition to prove the inf-sup property. The velocity interpolation employed by Hægland *et al.* actually defines the MFE velocity space proposed by Nédélec [59]. This space was found by Nédélec not to be compatible with a constant pressure. This leads to a non-consistent and of course non-convergent mixed finite element method. We argue that the corner velocity interpolation method will lead to non-physical streamlines and errors in time-of-flight.

- The direct interpolation of the MPFA subfluxes using the MFE velocity shape functions avoids the flux postprocessing procedures used by Prévost *et al.* and Hægland *et al.*

5.3 Numerical Experiments

5.3.1 Mixed finite element discretizations

In this section, we test the performance of the proposed streamline tracing approach on cases of increasing complexity. Focusing for now on MFE discretizations, we systematically compare the behavior of low-order and high-order tracing, both in terms of accuracy and grid sensitivity. For a clearer visualization of the results, we here focus on two-dimensional examples.

Validation on a uniform flow field

This first test case is designed for validation purposes. It tests the ability of the tracing method to produce exact results for a constant velocity field. The domain considered is the unit square: $\Omega = [0, 1]^2$. The permeability is assumed to be homogeneous, isotropic and equal to 1. Fixed pressures are imposed on the left and right boundaries and they take values of 1 and 0, respectively. The top and bottom boundaries are

impermeable. In this case, the exact streamlines are horizontal straight lines and a fluid particle takes a unit time to travel through the entire domain.

To test the robustness and accuracy of the tracing algorithm on this simple problem, the domain was discretized with a variety of grids (**Figure 5.1**):

- A 10×10 *Cartesian* grid serves as the base grid for our comparisons.
- The *chevron* grid is formed by keeping the vertical lines of the Cartesian grid and reorienting the horizontal edges to obtain a chevron-like pattern.
- A random movement of the Cartesian grid nodes creates the *random* grid. The node movement is bounded to ensure element convexity.
- The *skewed* grid is obtained from a diagonal distortion of the Cartesian grid.

All four grids have 100 elements. Four triangular grids were created from these quadrilateral grids by splitting each quadrilateral into two triangles. By construction, the triangular grids have twice as many elements as the quadrilateral grids: they are all composed of 200 elements.

Ten streamlines were traced on each grid. Figure 5.1 shows the streamlines traced on the four quadrilateral grids using the low-order RTN_0 approximation. The streamlines are drawn with thick red lines, and the grid with thin black lines. The background colors represent the pressure field.

The results obtained in this first test case indicate that regardless of the type of grid used (Cartesian, chevron, random or skewed), the type of building elements (triangles or quadrilaterals), or the type of discretization (RTN_0 or BDM_1), all streamlines traced are perfect straight lines. Unit time-of-flight were invariably obtained and, therefore, the tracing algorithm produces an exact time-of-flight in this case. This is to be expected given that both RTN_0 and BDM_1 elements satisfy the patch-test [72], that is, they can reproduce constant velocity fields in two dimensions.

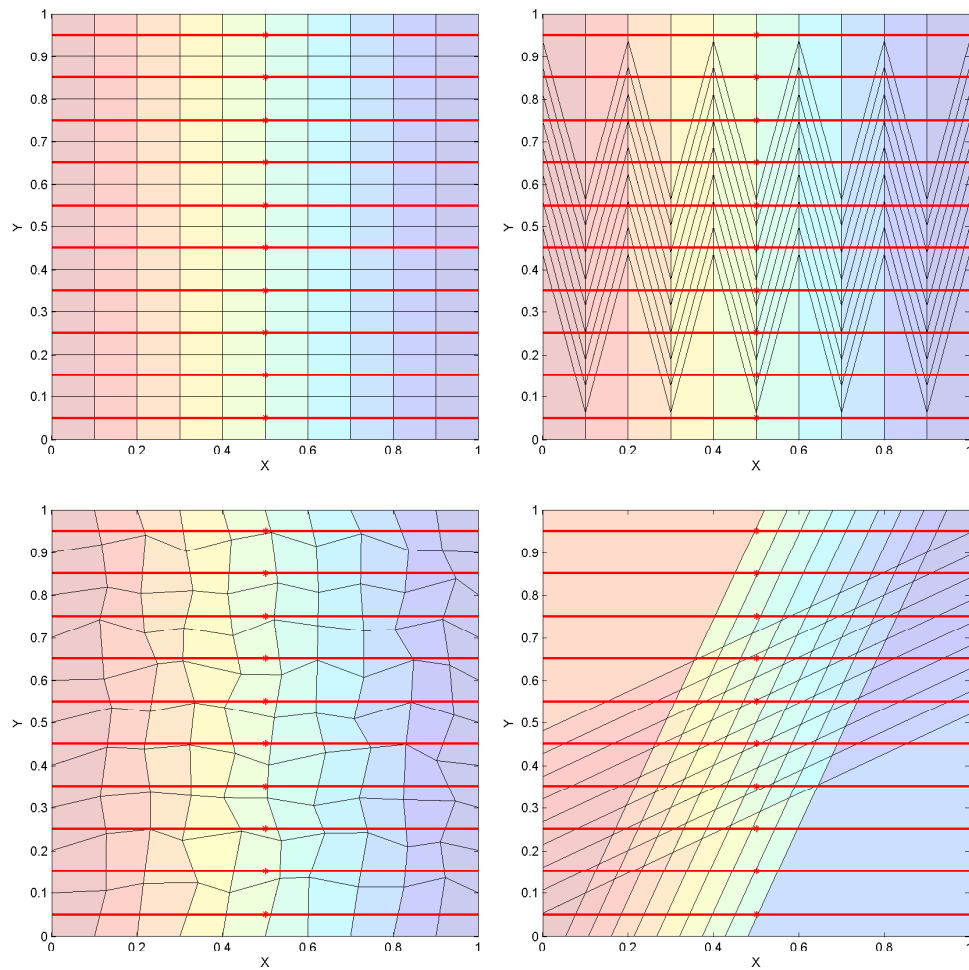


Figure 5.1. RTN_0 streamlines for the uniform flow problem on a Cartesian (top-left), chevron (top-right), random (bottom-left) and skewed (bottom-right) grids.

Robustness to grid distortion for a quarter of a five-spot problem

To quantify the robustness of the low-order and high-order versions of the streamline tracing algorithm, we study how much grid distortion affects the accuracy of the streamlines in terms of location and time-of-flight.

Using the same domain and grids as above, we now enforce pressures of 1 and 0 at the boundary edges of the bottom-left and top-right elements, respectively. The rest of the domain boundary is impermeable. The Dirichlet boundary elements are made identical regardless of the grid used to ensure comparable results.

Seven streamlines are traced on each grid and for each type of discretization. These streamlines are launched from equally spaced points along the diagonal of the domain. As an illustration, Figures 5.2 and 5.3 compare the streamlines traced using the RTN_0 and BDM_1 discretizations for the quadrilateral chevron and the triangular Cartesian grids, respectively. These two examples clearly show the strong influence of grid distortion on streamline accuracy for an RTN_0 discretization as well as the improved robustness demonstrated by BDM_1 . The higher-order method yields streamlines that are much smoother and much less sensitive to the distortion of the underlying grid. Notice, for example, the severe degree of nonsymmetry present in the streamlines computed using the low-order method on the chevron grid (**Figure 5.2**): the center streamline displays a tortuous path, when it should be a perfect straight line. This behavior improves dramatically when the higher-order approximation is used.

To quantify the apparent increased accuracy and robustness of the streamlines based on the higher-order velocity approximation, we compute the error in the time-of-flight for each of the seven streamlines. Reference values are obtained using an 80×80 Cartesian grid with a BDM_1 discretization. In Table 5.1 we report the average (arithmetic mean) time-of-flight error for each grid and type of discretization. We note the following observations:

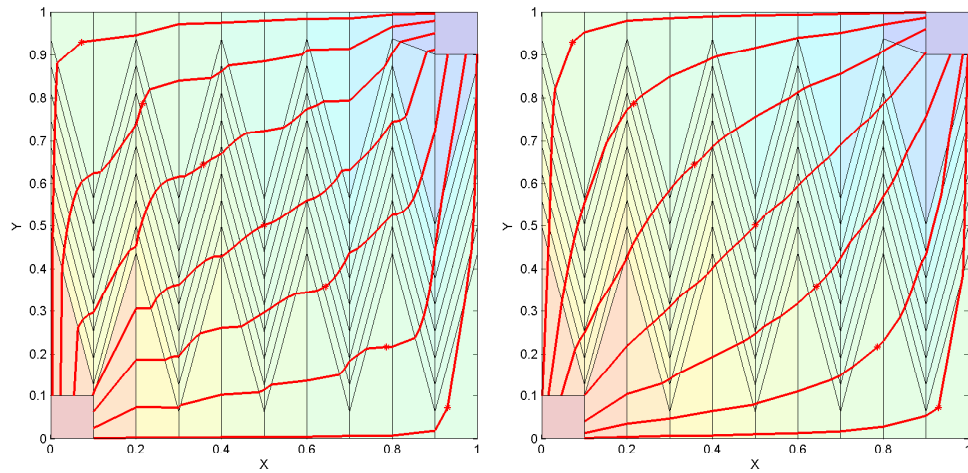


Figure 5.2. RTN_0 (left) and BDM_1 (right) streamlines on a quadrilateral chevron grid.

Table 5.1. Average time-of-flight error for the diagonal flow problem.

Element type	Discretization	Cartesian	Chevron	Random	Skewed
Triangle	RTN_0	11.39 %	16.09 %	13.05 %	9.14 %
	BDM_1	4.06 %	4.62 %	4.12 %	4.02 %
Quadrilateral	RTN_0	12.21 %	41.29 %	13.09 %	44.58 %
	BDM_1	2.45 %	5.51 %	2.13 %	2.85 %

1. For all grids, the time-of-flight error is lower —sometimes much lower— if the high-order BDM_1 approximation is used, rather than the low-order RTN_0 approximation. BDM_1 is more accurate than RTN_0 by a factor of 5 to 15 in the case of quadrilateral grids, and by a factor of 2 to 4 for triangular grids.
2. The variability of the BDM_1 time-of-flight error is much smaller than that of RTN_0 , confirming the robustness of the BDM_1 -based streamline tracing with respect to grid distortion.

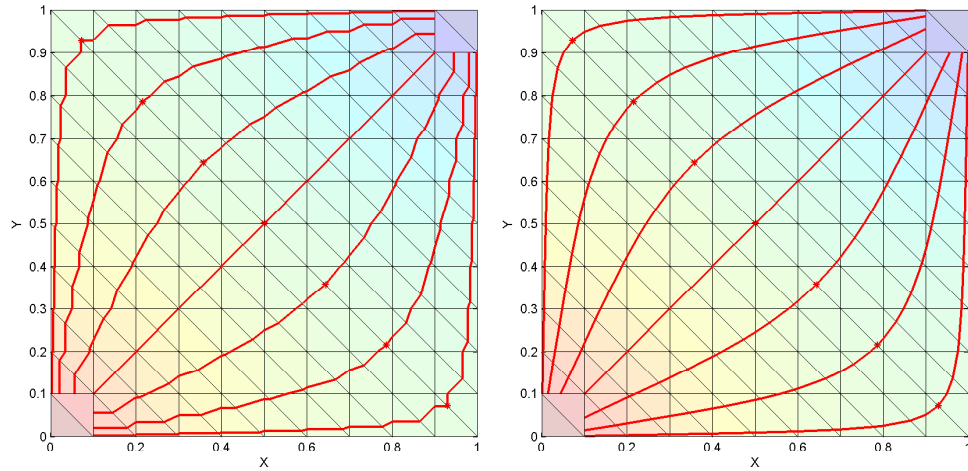


Figure 5.3. RTN_0 (left) and BDM_1 (right) streamlines on a triangular Cartesian grid.

Accuracy in the presence of heterogeneity

Heterogeneity of the medium —reflected in a discontinuous permeability field that may vary several orders of magnitude— is an essential characteristic of petroleum reservoirs. For this reason, we test the accuracy of our tracing method in heterogeneous domains. We employ a test case from an interesting study by Mosé *et al.* [56] that compares the performance of several discretization methods in the presence of heterogeneity. Four orders of magnitudes of permeability variations represent flow barriers and high-permeability streaks that force the streamlines to meander through the domain. The permeability field, shown in **Figure 5.4**, turns out to be challenging for some discretization methods, and we use it here to assess the quality of the RTN_0 and BDM_1 streamlines. In this test case, pressures of 1 and 0 are set at the top and bottom boundaries of the domain, respectively. The left and right boundaries are impermeable. A total of 19 streamlines are launched from equally spaced points located on the top boundary.

The 10×10 quadrilateral Cartesian grid that constitutes the base case shown in

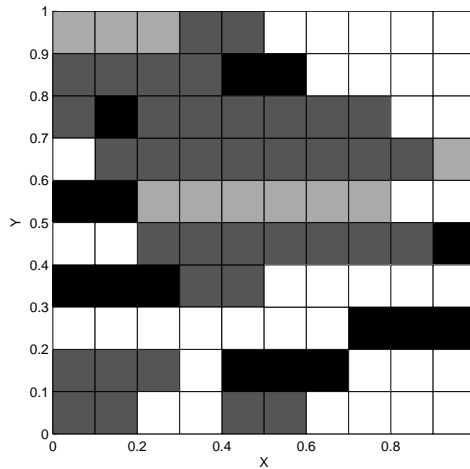


Figure 5.4. Permeability field employed, taken from a test case in [56]. Permeability values: white = 1; light gray = 10^{-1} ; dark gray = 10^{-2} ; black = 10^{-3} .

Figure 5.4 was refined into 20×20 and 40×40 Cartesian grids. Each of these grids was also transformed into a triangular grid by subdividing each quadrilateral element into two triangles.

Figures 5.5 and 5.6 compare the RTN_0 and BDM_1 streamlines on the 20×10 and 80×40 triangular grids, respectively. It is important to note that the streamlines obtained with all grids and discretizations orders are physical: they avoid entirely the low permeability regions, in agreement with the findings of Mosé *et al.* [56]. The streamlines computed with the higher-order BDM_1 discretization, however, are smoother and less sensitive to the level of refinement. We quantify these observations by computing the time-of-flight errors on the streamlines using a 80×80 Cartesian grid with a BDM_1 discretization as a reference. The results are presented in Table 5.2. As expected, the BDM_1 errors are always much lower than those of RTN_0 .

A legitimate question to ask is what is the incremental cost associated with the improved accuracy of BDM_1 . By now, we have established that for a given grid, BDM_1 streamlines are more accurate than RTN_0 ones. To obtain this accuracy, however,

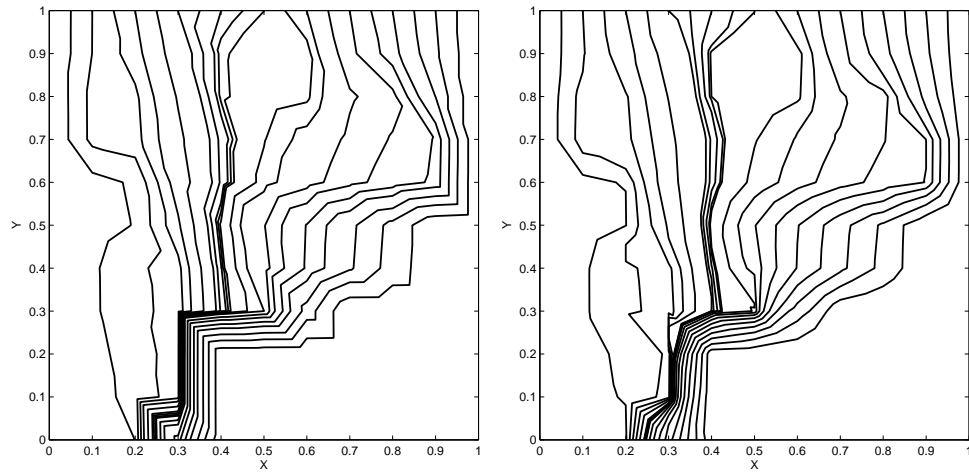


Figure 5.5. RTN_0 (left) and BDM_1 (right) streamlines for a grid of 200 triangular elements.

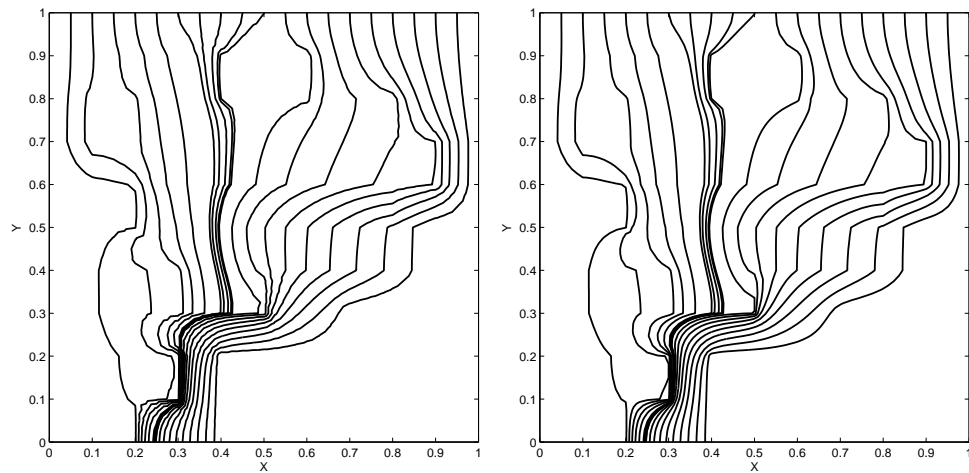


Figure 5.6. RTN_0 (left) and BDM_1 (right) streamlines for a grid of 3200 triangular elements.

Table 5.2. Average time-of-flight error in the presence of heterogeneity.

Element type	Discretization	10×10	20×20	40×40
Triangle	RTN_0	13.39 %	6.55 %	3.49 %
	BDM_1	3.57 %	1.61 %	0.23 %
Quadrilateral	RTN_0	8.58 %	4.19 %	2.20 %
	BDM_1	5.64 %	2.00 %	0.02 %

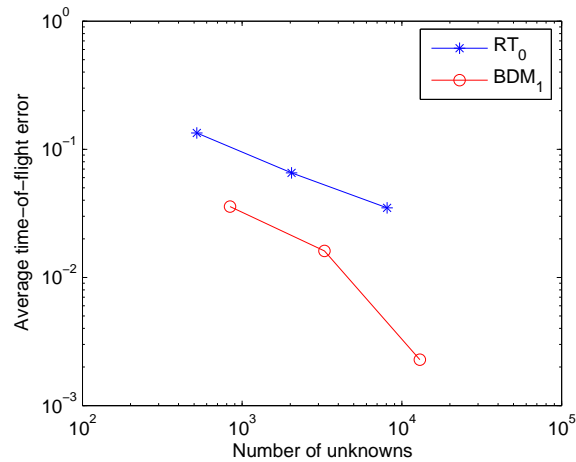


Figure 5.7. Average time-of-flight error as a function of the number of unknowns for a sequence of triangular grids.

one must solve for roughly twice as many velocity unknowns. In **Figure 5.7**, we plot the average time-of-flight errors for triangular grids as a function of the number of unknowns. Clearly, for a given number of unknowns, BDM₁ is more accurate than RTN₀. Refining the grid with an RTN₀ discretization is not as efficient as increasing the order of accuracy of the method by using the BDM₁ space. Moreover, the slopes of the two curves are different: BDM₁ seems to converge faster than RTN₀ as the number of unknowns is increased, although this could be an artifact of not having yet reached the asymptotic convergence regime.

Heterogeneous unstructured grids

Our last experiment for MFE discretizations tests the ability of the tracing method to deal with more realistic reservoir simulation grids such as unstructured grids and heterogeneous permeability fields. The domain, presented in **Figure 5.8**, is a 1×1 square of unit permeability except for two flow barriers of low (10^{-3}) permeability represented by the black elements. Once again, pressures of 1 and 0 are set at the bottom-left and top-right corners (marked by thicker boundary lines) and the rest of

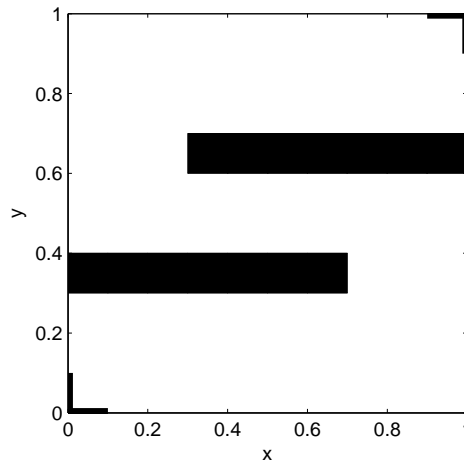


Figure 5.8. Base case for the unstructured grid discretization.

the boundaries are impermeable.

Streamlines are launched from ten points located in the center of the domain. Figure 5.9 shows a comparison of the RTN_0 and BDM_1 streamlines for this problem using the same unstructured grid of 148 triangular elements. As before, the grid is shown in thin black lines, the streamlines with thick red lines, and their launching points are marked by a red star. The streamlines computed by the low-order and high-order approximations on a refined grid of 350 elements are shown in **Figure 5.10**. In agreement with previous observations, the BDM_1 streamlines are smoother and much less sensitive to the grid refinement level.

To compute the time-of-flight errors committed on this unstructured grid, similar streamlines were traced on an 80×80 Cartesian grid with a BDM_1 discretization. Table 5.5 presents the time-of-flight errors committed for both the RTN_0 and BDM_1 discretizations on the 148-element and 350-element grids. For both grids, the BDM_1 streamlines are about five times more accurate than the RTN_0 ones.

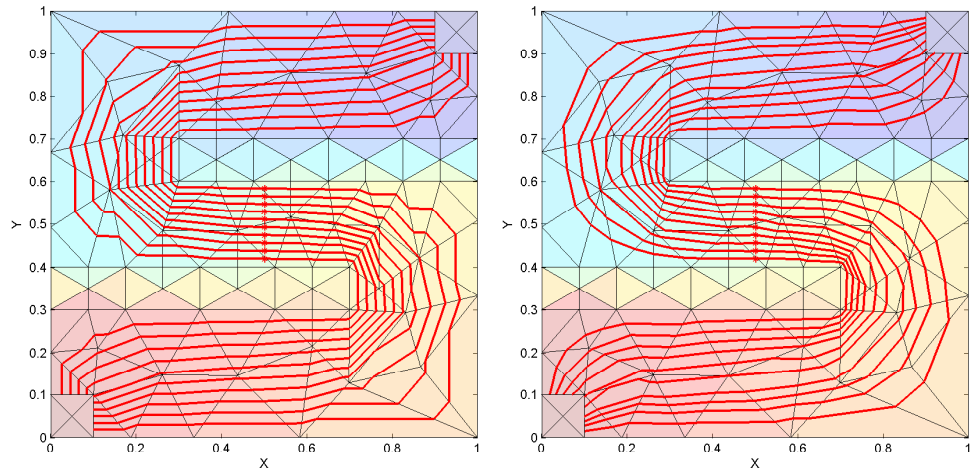


Figure 5.9. RTN_0 (left) and BDM_1 (right) streamlines for a 148-element grid.

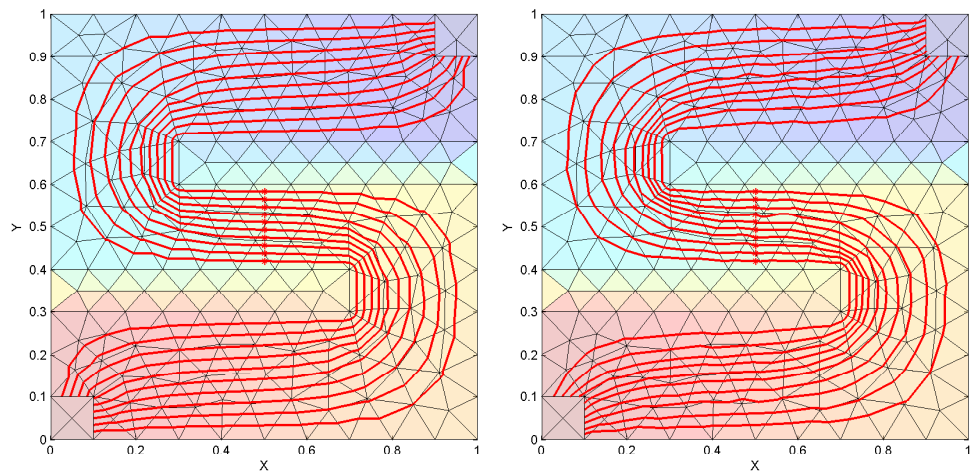


Figure 5.10. RTN_0 (left) and BDM_1 (right) streamlines for a 350-element grid.

Table 5.3. Average time-of-flight error for the heterogeneous unstructured grid test case.

Discretization	148 elements	350 elements
RTN_0	15.20 %	7.25 %
BDM_1	3.17 %	1.71 %

5.3.2 MPFA discretizations

In this section, we compare the streamlines obtained with the low-order and high-order tracing methods described above, obtained *from the same MPFA solution* of the elliptic pressure equation. The differences are due exclusively to the amount of information used for the velocity reconstruction: only the MPFA edge fluxes in the low-order RTN₀-based tracing, and the MPFA half-edge fluxes in the high-order BDM₁-based tracing. Moreover, because they emanate from the same pressure solution and since their path is known analytically, no significant or consistent difference was observed in the computational cost of both sets of streamlines. The differences in computational cost are due solely to the numerical integration of the time-of-flight, which was not found to depend strongly on the type of velocity field used. Once again, we study the sensitivity of the method to grid distortion, permeability anisotropy and heterogeneity.

Grid Distortion and Full-Tensor Permeability

A full permeability tensor is required for the description of anisotropic permeability fields with principal directions misaligned with the simulation grid.

In this example, we test the ability of our streamline tracing algorithm to enhance the velocity description and streamline quality in the presence of full tensor permeabilities. The first test case is based on a strongly distorted quadrilateral grid shown in **Figure 5.11** and formed by chevron-shaped elements exhibiting a 70° distortion angle. To test the tracing methods on a triangular grid, each quadrilateral of the chevron grid was also split in two triangles to form the grid shown in **Figure 5.13**.

The domain has impervious boundaries and quarter of a five spot pattern pressure boundary conditions are set: unit pressure is fixed at the bottom-left gridblock and zero pressure is imposed at the top-right cell.

The permeability field is homogeneous but presents a ten-to-one anisotropy ratio and is rotated by a 45° angle from the principal coordinate system:

$$\mathbf{k} = \mathbf{R}^t \begin{pmatrix} 10 & 0 \\ 0 & 1 \end{pmatrix} \mathbf{R} = \begin{pmatrix} 5.5 & 4.5 \\ 4.5 & 5.5 \end{pmatrix}, \quad (5.7)$$

with the rotation matrix \mathbf{R} defined by

$$\mathbf{R} = \begin{pmatrix} \cos(45^\circ) & \sin(45^\circ) \\ -\sin(45^\circ) & \cos(45^\circ) \end{pmatrix}. \quad (5.8)$$

The MPFA method leads to a nine-point stencil on the quadrilateral grid and, in this case, the contributions of the diagonal entries of the stencil are expected to be significant. The pressure solutions for this test case are presented in **Figure 5.11** and **Figure 5.13**.

To compare the streamlines traced with the classical and higher-order flux reconstruction techniques, we used a reference solution defined with the same boundary conditions and permeability field, but computed on a 100×100 Cartesian grid and solved with a BDM_1 mixed finite element method. The reference streamlines are shown in **Figure 5.11** and **Figure 5.13**.

Figure 5.12 and **Figure 5.14** compare the low-order (solid lines) and high-order (dotted lines) streamlines obtained on the quadrilateral and triangular grids, respectively. Table 5.4 reports the relative error in time-of-flight recorded for each streamline, with respect to the reference streamlines obtained on the refined grid with the mixed finite element method. The streamlines are numbered from the top to the bottom. The average time of flight error is also presented.

Clearly, for both the quadrilateral and the triangular grids, the streamlines obtained with the BDM_1 -based flux reconstruction technique are more accurate, both in

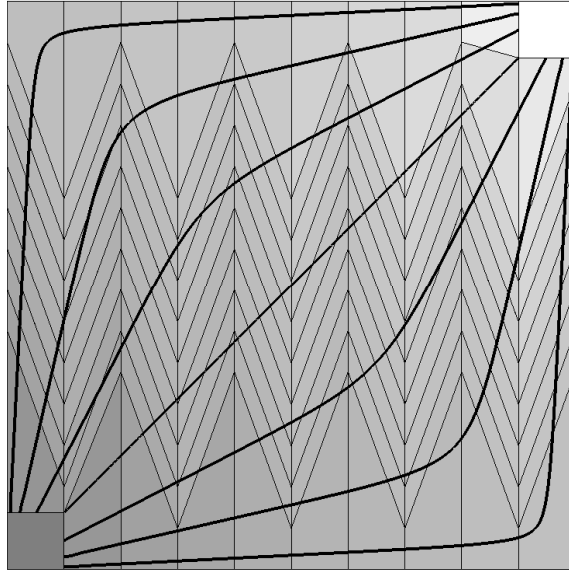


Figure 5.11. Pressure solution on the quadrilateral chevron grid and reference streamlines.

terms of actual location and time of flight. In addition, we recall that this increased accuracy of the BDM_1 -based tracing is obtained with the same computational cost and memory requirements as the RTN_0 streamlines.

To understand the importance of the time-of-flight accuracy, we focus our attention on the diagonal streamline (the fourth streamline from the top). In the simulation of an injection problem, the time-of-flight along this diagonal streamline would provide the breakthrough time of the injected fluid. We see that using the RTN_0 -based tracing, which is Pollock’s method corrected for grid distortion and full tensor permeabilities, would lead to a 11% error in the estimated breakthrough time. The use of the BDM_1 -based tracing reduces this error to under 2%.

Permeability Heterogeneity

Reservoir heterogeneity is a key component of any reservoir model. It is therefore crucial for a streamline tracing algorithm to accurately handle the discontinuities of

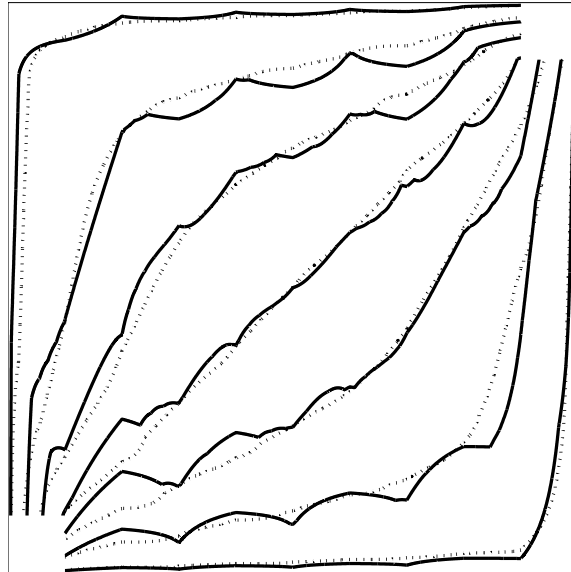


Figure 5.12. Streamlines traced on the quadrilateral chevron grid with the RTN_0 (solid lines) and BDM_1 (dotted lines) velocity fields.

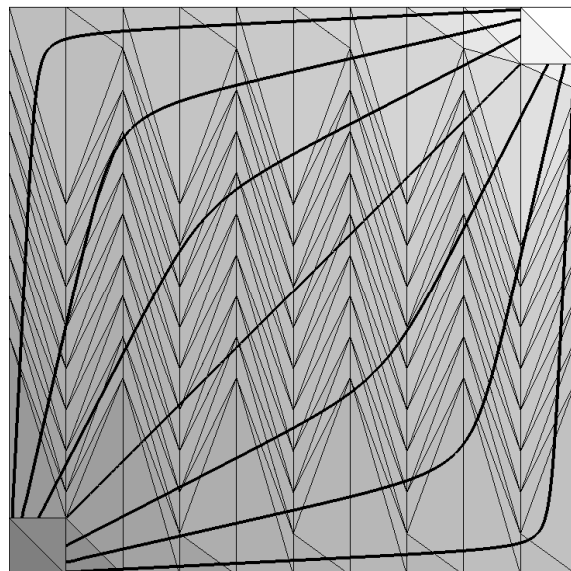


Figure 5.13. Pressure solution on the triangular chevron grid and reference streamlines.

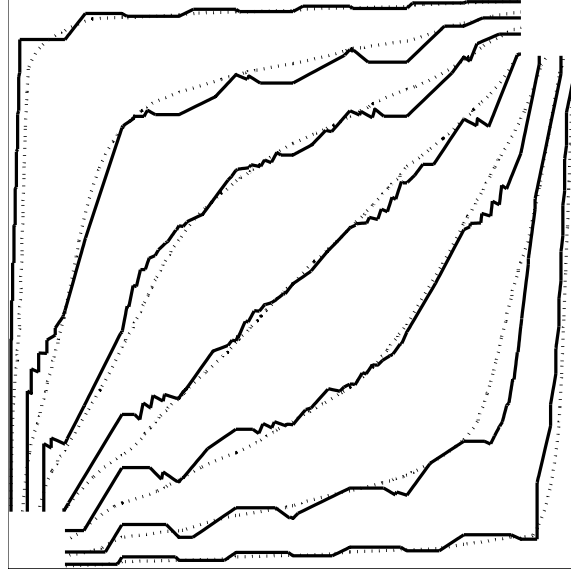


Figure 5.14. Streamlines traced on the triangular chevron grid with the RTN_0 (solid lines) and BDM_1 (dotted lines) velocity fields.

Table 5.4. Relative time of flight error for each streamline traced on the chevron grids.

SL #	Quadrilaterals		Triangles	
	RTN_0	BDM_1	RTN_0	BDM_1
1	26.50 %	7.92 %	12.99 %	6.91 %
2	5.05 %	5.04 %	2.70 %	2.62 %
3	4.07 %	1.37 %	1.92 %	1.42 %
4	11.23 %	1.61 %	12.09 %	3.44 %
5	3.66 %	1.33 %	2.70 %	0.35 %
6	4.84 %	1.21 %	2.50 %	0.95 %
7	55.56 %	5.57 %	26.95 %	6.47 %
Avg.	15.84 %	3.43 %	8.84 %	3.17%

permeability fields.

To isolate the influence of the permeability heterogeneity from that of permeability anisotropy or grid distortion, we simulate a problem on a Cartesian grid populated with heterogeneous but isotropic permeability. As in the previous section, we use the test case proposed by Mosé *et al.* [56], designed to compare the performance of various discretization methods in the presence of heterogeneity and presented in **Figure 5.4**. A unit pressure is set at the top boundary and a zero pressure at the bottom. The left and right domain boundaries are impermeable. Streamlines are launched at equidistant points located at the top of the domain.

On a Cartesian grid and with a diagonal permeability tensor, MPFA reduces to the classical 5-point stencil of the two-point flux approximation. Because the diagonal points are not included in the stencil, both subedge transmissibilities associated with a given interface are equal, which leads to a constant velocity profile through any given edge. For validation purposes, we here check that both the low- and high-order tracing algorithms recover identical streamlines. The streamlines obtained from both methods are plotted in **Figure 5.15**. A single set of streamlines is visible as they overlap exactly. As expected, both tracing methods result in identical time-of-flights as well.

Unstructured Grid

This last example represents a reservoir composed of two rock types, a base rock of relatively high permeability and a low-permeability rock forming three flow barriers. The permeability of the base rock presents a ten-to-one anisotropy ratio and its principal directions are rotated by a 15° angle from the coordinate system:

$$\mathbf{k} = \mathbf{R}^t \begin{pmatrix} 10 & 0 \\ 0 & 1 \end{pmatrix} \mathbf{R} \approx \begin{pmatrix} 9.40 & 2.25 \\ 2.25 & 1.60 \end{pmatrix}, \quad (5.9)$$

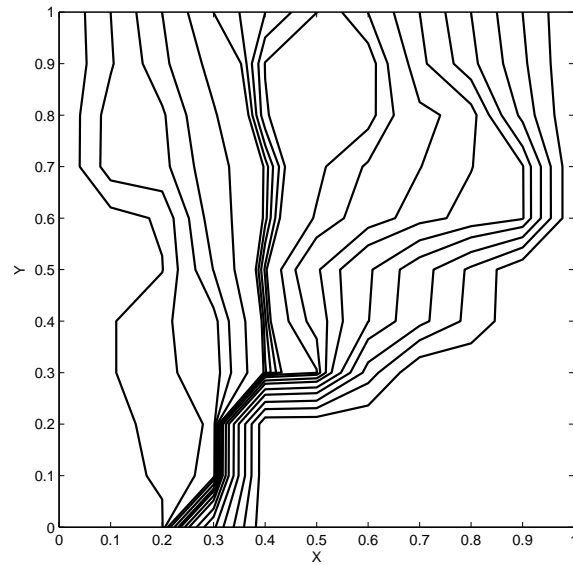


Figure 5.15. MPFA streamlines from the RTN_0 and BDM_1 -based tracing (overlapping exactly).

with the rotation matrix \mathbf{R} defined as in (5.8). The rock forming the flow barriers is isotropic and of permeability 10^{-3} .

The domain boundaries are impervious. An injector of unit pressure is placed at the bottom left of the domain and a producer of zero pressure is located in the top right corner. To describe accurately the geometry of the flow barriers and the well locations, two unstructured triangular grids are defined. The coarse, 599-element grid is shown on **Figure 5.17** and the finer 4841-element grid is presented in **Figure 5.18**.

On the coarser grid, MPFA is used to solve the flow problem and streamlines are traced using the RTN_0 and BDM_1 velocity field reconstruction. Ten streamlines are launched from the edges of the injecting well and traced all the way to the edges of the producing well. **Figure 5.16** shows the launching points of the streamlines and presents their numbering. **Figure 5.20** compares the streamlines obtained on the coarse grid with the RTN_0 - and BDM_1 -based tracing methods.

On the fine grid, a BDM_1 mixed finite element method is used to solve for the

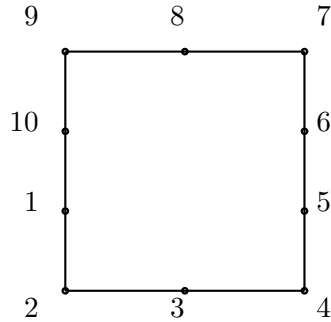


Figure 5.16. Location of the streamline launching points on the edges of the gridcell containing the injection well.

pressure and velocity fields and to trace the streamlines presented in **Figure 5.19** that we use as reference.

Table 5.5 presents the relative errors in time-of-flight for the ten streamlines traced on the coarse grid with the RTN_0 and the BDM_1 velocity fields. Once again, the results show how the BDM_1 -based tracing algorithm provides superior streamlines than the RTN_0 -based method, both in terms of location and time-of-flight. It is interesting to notice that the fifth and sixth streamlines traced with the RTN_0 velocity field present the largest time-of-flight errors. The corresponding BDM_1 -based streamlines are more than twice as accurate. Because of their central location, these streamlines have the highest velocities and shortest time-of-flight so that they carry the most flow between the two wells. Therefore, in this example, the BDM_1 tracing is expected to have a large positive impact on the overall accuracy of the streamline method.

5.3.3 Three-dimensional unstructured grids

This serves as a simple illustration of the possible use of the streamline tracing approach developed here on a synthetic, but realistic reservoir simulation model.

The reservoir is bounded by trapping structured of anticline shape. Eleven major faults are spread throughout the reservoir and are supposed to be flow barriers. At

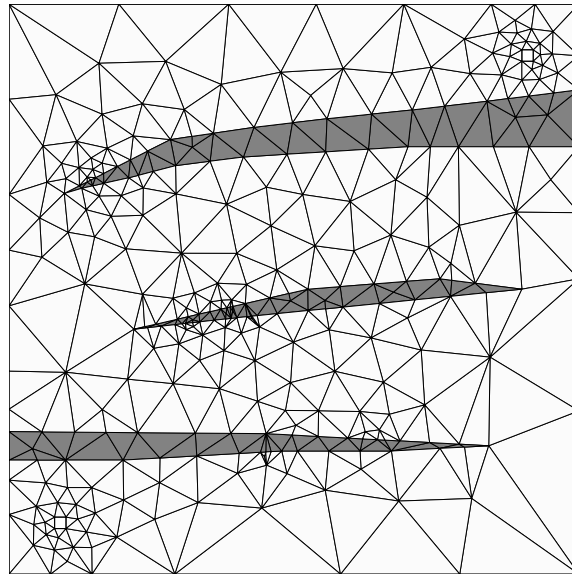


Figure 5.17. Coarse unstructured grid and permeability field.

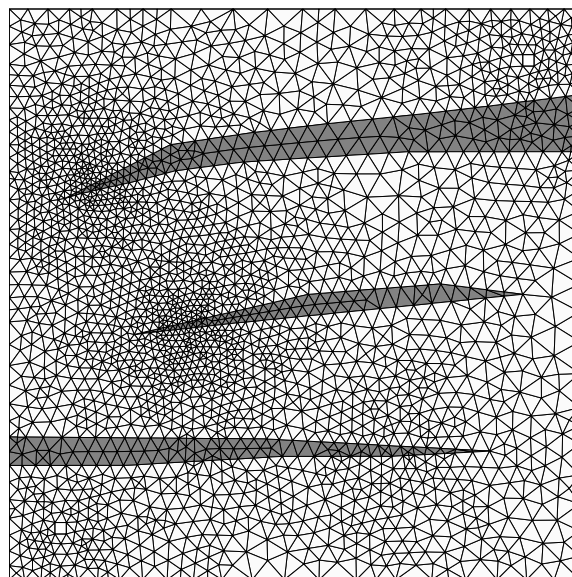


Figure 5.18. Reference unstructured grid.

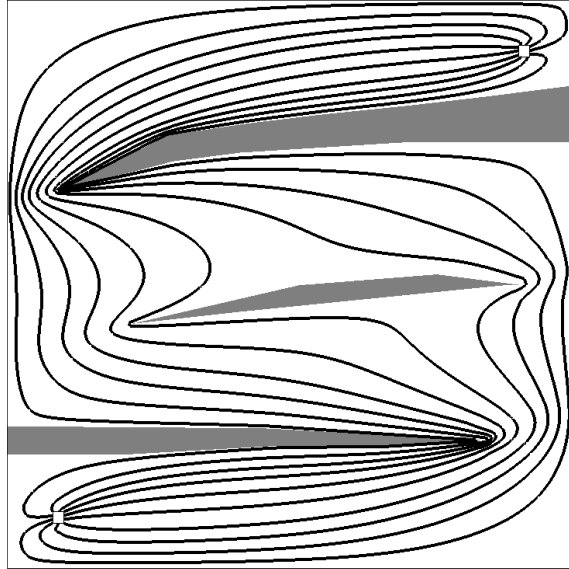


Figure 5.19. Streamlines traced on the reference unstructured grid.

Table 5.5. Relative time of flight error for the streamlines traced on the unstructured grid.

SL #	RTN ₀	BDM ₁
1	3.94 %	1.37 %
2	5.61 %	3.01 %
3	7.88 %	4.37 %
4	9.86 %	7.08 %
5	20.15 %	8.50 %
6	17.84 %	8.03 %
7	12.13 %	8.23 %
8	8.80 %	6.90 %
9	7.22 %	4.72 %
10	11.71 %	10.60 %
Avg.	10.51%	6.28%

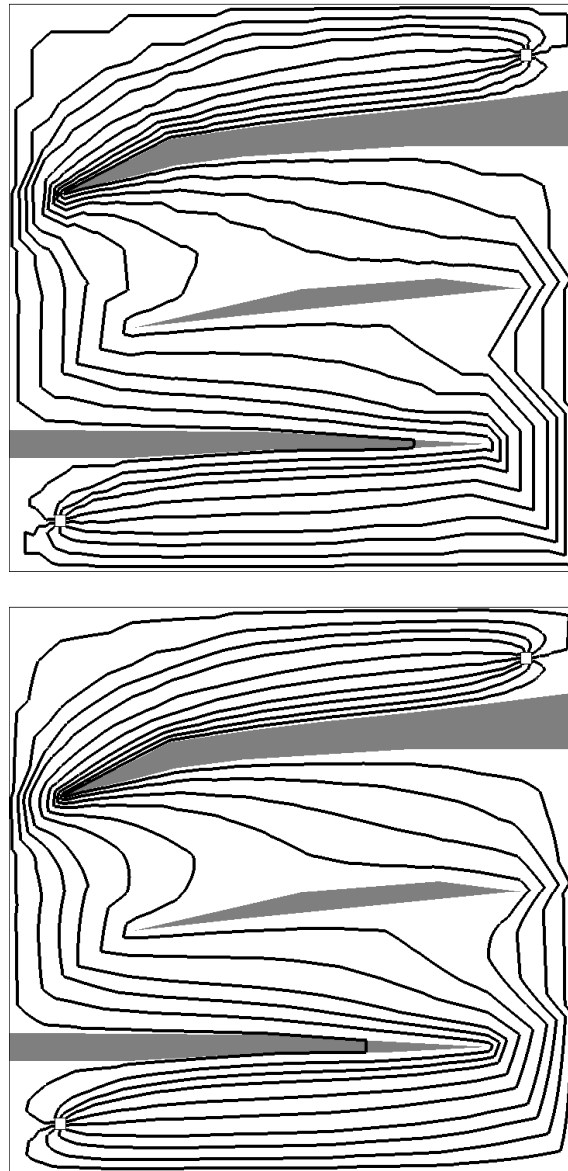


Figure 5.20. Streamlines traced on the coarse unstructured grid with the RTN_0 (top) and BDM_1 (bottom) based tracing.

this stage of the reservoir development, seven wells have been drilled in the formation. Four wells are producing hydrocarbons and three wells are injecting water as an improved recovery mechanism.

Because of the complex geometry of the reservoir, a tetrahedral grid is used to represent accurately the geology. The grid conforms to the faults and the wells as can be seen from the top view of **Figure 5.21**. The grid is also constrained to follow the depositional horizons as can be seen in a side view of the reservoir in **Figure 5.22**.

A variogram-based geostatistical method [36] has been used to populate a geo-model with permeability and porosity distribution matching the hard data available at the wells. A local-global upscaling method [21] was used to provide equivalent full-tensor permeability coefficients on the reservoir simulation grid.

The resulting grid is a fully unstructured tetrahedral grid populated with heterogeneous tensor coefficients. The pressure is maintained constant at the wells and the reservoir boundaries and faults are considered to be impervious. The MPFA method is used to properly discretize the elliptic pressure equation on this complex simulation grid.

The high-order tracing algorithm, based on the BDM_1 velocity reconstruction was used to obtain the streamlines of the flow. To perform streamline simulation with an appropriate accuracy, an extremely dense set of streamline is necessary (**Figure 5.23**). For clarity of visualization, we only represent a dozen streamlines by producing well. The streamlines are launched from the walls of the producers and are colored accordingly (**Figure 5.24**).

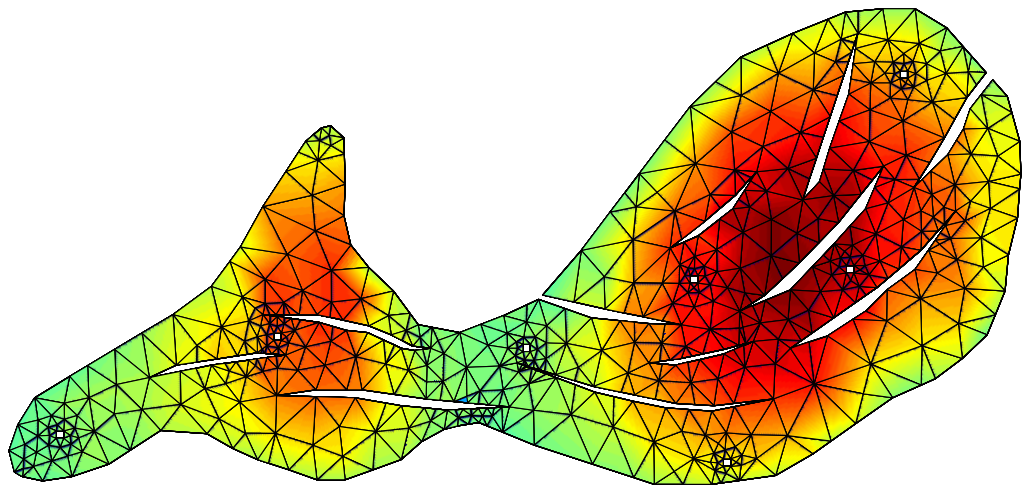


Figure 5.21. Top view of the synthetic reservoir.

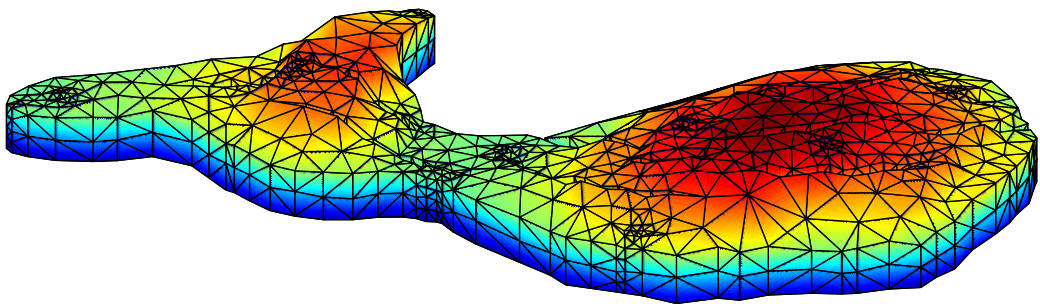


Figure 5.22. Side view of the synthetic reservoir.

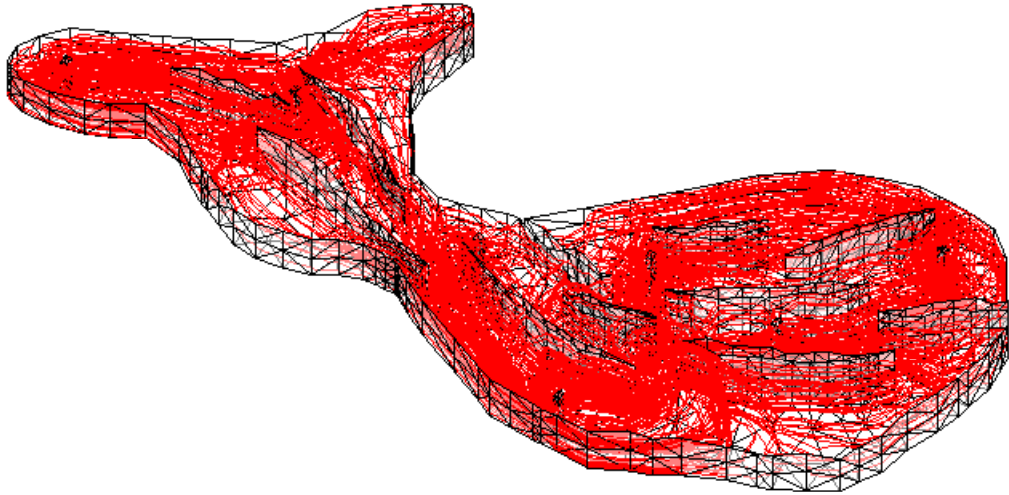


Figure 5.23. Full set of streamlines necessary to solve the transport problem

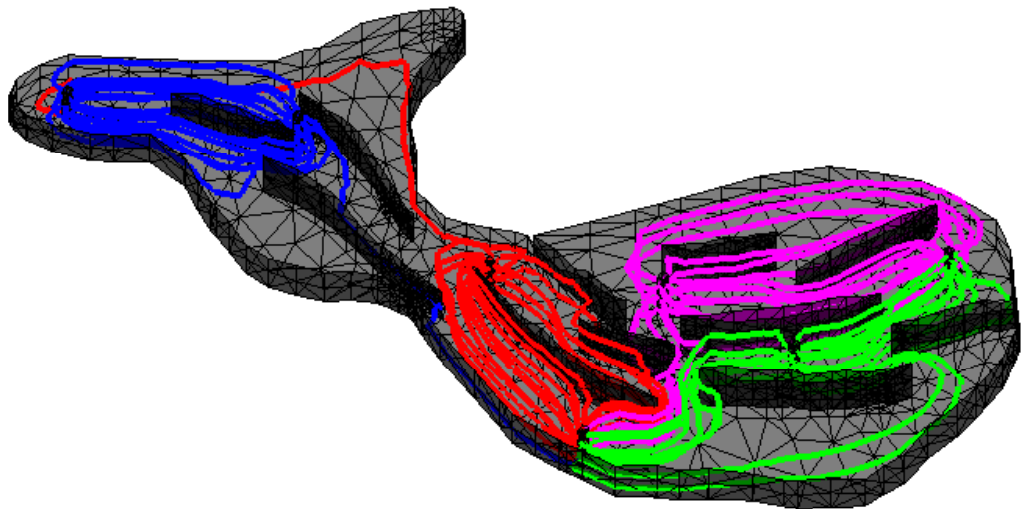


Figure 5.24. A selection of representative streamlines traced using the BDM_1 -based method

Chapter 6

Conclusions and Future Work

6.1 Conclusions

Traditional and streamline-based reservoir simulation rely on finite volume discretizations of the elliptic pressure equation. On advanced grids, involving distorted elements and full-tensor permeability coefficients, multipoint flux approximations (MPFA) are used to ensure the accuracy of the spatial discretization. Despite the wide use of MPFA methods in the industry, their mathematical properties remain mainly unknown. In this work, we study MPFA discretizations from the mathematical framework of mixed finite element (MFE) methods.

To do so, a link must be established between MPFA and MFE discretizations. On hexahedra, this requires a new MFE velocity space, which we introduce in this dissertation. The new space is defined by four degrees of freedom per face. The trace of the velocity field is thus bilinear on each face and can be defined by vertex-based shape functions. The new space is constructed to be compatible with a constant pressure space in each element. The resulting MFE method is thus consistent and an error analysis establishes its convergence. The error estimates obtained and the numerical experiments conducted show that, this new velocity space is, in fact, the

most accurate of the three velocity spaces that are known to be compatible with a piecewise constant pressure discretization –the other two spaces being the lowest-order Raviart–Thomas–Nédélec (RTN₀) and the first-order Brezzi–Douglas–Marini (BDM₁) space.

The application of the vertex-based trapezoidal quadrature to the new MFE method restricts the interactions between velocity degrees of freedom. This localization effect allows the MFE discretization to be written as a sparse finite volume method that was shown to be the MPFA O-method. We have thereby established for the first time a link between MFE and MPFA methods on hexahedra.

The trapezoidal quadrature used to reduce the new mixed finite element into MPFA induces a scalar product on the new velocity space and preserves the consistency of the discretization. An error analysis shows that the trapezoidal quadrature is accurate enough to guarantee convergence of the MPFA O-method on rectangular hexahedra.

The MFE framework of FV methods is finally used in the context of streamline simulation. In this dissertation, we proposed a new streamline tracing method for MFE and FV discretizations. In MFE methods, velocity shape functions are used to interpolate the flux degrees of freedom into a velocity field, which can be integrated to yield the streamlines. For FV discretizations, we rely on the established correspondence between MFE and FV methods to interpret the TPFA or MPFA fluxes as velocity degrees of freedom. The low-order version of the algorithm relies on an RTN₀ velocity field reconstruction and is, in fact, equivalent to the extension of Pollock’s streamline tracing method to distorted grids. The higher-order version of the algorithm that makes use of the BMD₁ space on triangles, quadrilaterals and tetrahedra and of the new velocity space on hexahedra, was shown to yield more accurate streamlines than any other existing method. In addition, the interpretation of the MPFA fluxes as MFE degrees of freedom avoids the expensive flux post-processing

techniques used by the other existing MPFA streamline tracing methods. This new approach therefore leads to a streamline tracing algorithm that is (1) accurate enough to allow the streamline method to be used on advanced grids without the $O(1)$ errors introduced by low-order tracing methods, and (2) fast enough to trace the millions of streamlines required by a full-field simulation.

6.2 Future work

In this section, we present three possible extensions of the research work presented in this dissertation.

Prism grids

A prism grid is the projection of a two-dimensional triangular grid onto the third dimension. Such grids are particularly well-suited for the description of layered petroleum reservoirs. The numerical or analytical convergence of MPFA methods, and the relationship between MPFA and MFE methods on such grids remains unpublished.

Three MFE velocity spaces are known to be compatible with a constant element pressure on prism grids [23; 59]. However, none of these velocity spaces can be defined by vertex-based degrees of freedom. Therefore, it seems challenging to relate MPFA methods with existing MFE velocity spaces on prism grids.

The approach that we developed in this dissertation for the hexahedral element can be applied for prisms in order to define a new space. The space should be defined by four degrees of freedom per quadrilateral face and three degrees of freedom per triangular face, leading to a space of dimension 18. A careful construction could ensure that the space remains compatible with a piecewise constant discretization. The application of the trapezoidal quadrature would localize such a space into an

MPFA method, providing the missing link between MPFA and MFE methods on prism grids. This link could potentially be exploited to develop a proof of convergence of MPFA and a new streamline tracing algorithm on such grids.

New class of MFE spaces

This dissertation was focused on the study of MFE methods in the context of petroleum reservoir simulation, and was therefore restricted to piecewise constant discretizations of the scalar variable. In other applications, it is possible to employ higher-order descriptions of the scalar variable. An extension of the lowest-order vector space developed in this work to a full class of vector spaces compatible with higher-order scalar variable discretizations would be a valuable contribution to the theory finite-element methods. The degrees of freedom for these spaces could be defined as those of Nédélec [59], but for compatibility, should be constructed using the Brezzi–Douglas–Marini [16] technique of enriching polynomial space by divergence-free polynomials of higher degree.

Monotonicity

Permeability anisotropy and grid distortion can represent a challenge for the monotonicity of spatial discretization methods. So far, there is no control-volume discretization method known to be both linearly exact, and monotone for all permeability tensors and grid distortion.

In [50], we presented a new approach for stabilization of MFE method in the presence of anisotropy. Numerical experiments have shown that an inexact quadrature can, in some cases, be used to improve the monotonicity of the MFE method. More work is however required to fully understand and predict the effects of this *reduced integration* approach on the MFE discretization.

Bibliography

- [1] I. Aavatsmark. An introduction to multipoint flux approximations for quadrilateral grids. *Comput. Geosci.*, 6:405–432, 2002.
- [2] I. Aavatsmark, T. Barkve, Ø. Bøe, and T. Mannseth. Discretization on non-orthogonal, quadrilateral grids for inhomogeneous, anisotropic media. *J. Comput. Phys.*, 127:2–14, 1996.
- [3] I. Aavatsmark, T. Barkve, Ø. Bøe, and T. Mannseth. Discretization on unstructured grids for inhomogeneous, anisotropic media. Part I: Derivation of the methods. *SIAM J. Sci. Comput.*, 19(5):1700–1716, 1998.
- [4] I. Aavatsmark, T. Barkve, Ø. Bøe, and T. Mannseth. Discretization on unstructured grids for inhomogeneous, anisotropic media. Part II: Discussion and numerical results. *SIAM J. Sci. Comput.*, 19(5):1717–1736, 1998.
- [5] I. Aavatsmark, T. Barkve, and T. Mannseth. Control-volume discretization methods for 3D quadrilateral grids in inhomogeneous, anisotropic reservoirs. *Soc. Pet. Eng. J.*, 3(2):146–154, June 1998.
- [6] I. Aavatsmark, G. T. Eigestad, and R. A. Klausen. Numerical convergence of the MPFA O-method for general quadrilateral grids in two and three dimensions. In D. N. Arnold, P. B. Bochev, R. B. Lehoucq, R. A. Nicolaides, and M. Shashkov, editors, *Compatible spatial discretizations*, volume 142 of *IMA Vol. Ser.*, pages 1–21. Springer, New York, 2006.
- [7] I. Aavatsmark, G. T. Eigestad, R. A. Klausen, M.F. Wheeler, and I. Yotov. Convergence of a symmetric MPFA method on quadrilateral grids. *Comput. Geosci.*, 11:333–345, DOI:10.1007/s10596-007-9056-8, 2007.

- [8] T. Arbogast, C. N. Dawson, P. T. Keenan, M. F. Wheeler, and I. Yotov. Enhanced cell-centered finite differences for elliptic equations on general geometry. *SIAM J. Sci. Comput.*, 19:404–425, 1998.
- [9] T. Arbogast, M. F. Wheeler, and I. Yotov. Mixed finite elements for elliptic problems with tensor coefficients as cell-centered finite differences. *SIAM J. Numer. Anal.*, 34:828–852, 1997.
- [10] K. Aziz and A. Settari. *Petroleum Reservoir Simulation*. Elsevier, London, 1979.
- [11] I. Babuška. The finite element method with Lagrangian multipliers. *Numer. Math.*, 20:179–192, 1973.
- [12] R. P. Batycky. *A Three-Dimensional Two-Phase Field Scale Streamline Simulator*. PhD Dissertation, Stanford University, January 1997.
- [13] S. C. Brenner and L. R. Scott. *The Mathematical Theory of Finite Element Methods*, volume 15 of *Texts in Applied Mathematics*. Springer-Verlag, New York, 1994.
- [14] F. Brezzi. On the existence, uniqueness and approximation of saddle point problems arising from Lagrange multipliers. *RAIRO Anal. Numér.*, 8:129–151, 1974.
- [15] F. Brezzi, J. Douglas, Jr., R. Duran, and M. Fortin. Mixed finite elements for second order elliptic problems in three variables. *Numer. Math.*, 51:237–250, 1987.
- [16] F. Brezzi, J. Douglas, Jr., and L. D. Marini. Two families of mixed finite elements for second order elliptic problems. *Numer. Math.*, 47:217–235, 1985.
- [17] F. Brezzi and M. Fortin. *Mixed and Hybrid Finite Element Methods*, volume 15 of *Springer Series in Computational Mathematics*. Springer-Verlag, New York, 1991.

- [18] J. Caers. *Petroleum Geostatistics*. Environmental Science Series. Society of Petroleum Engineers, New York, 2005.
- [19] Z. Cai, J. Douglas, Jr., and M. Park. Development and analysis of higher order finite volume methods over rectangles for elliptic equations. *Adv. Comput. Math.*, 19:3–33, 2003.
- [20] G. Chavent and J. Jaffré. *Mathematical Models and Finite Elements for Reservoir Simulation*, volume 17 of *Studies in Mathematics and its Applications*. Elsevier, North-Holland, 1986.
- [21] Y. Chen, L. J. Durlofsky, M. Gerritsen, and X. H. Wen. A coupled local–global upscaling approach for simulating flow in highly heterogeneous formations. *Adv. Water Resour.*, 26(10):1041–1060, 2003.
- [22] Z. Chen. *Finite Element Methods and Their Applications*, volume 15 of *Springer Series in Scientific Computation*. Springer-Verlag, Berlin, 2005.
- [23] Z. Chen and J. Douglas Jr. Prismatic mixed finite elements for second order elliptic problems. *Calcolo*, 26:135–148, 1989.
- [24] Z. X. Chen and X. J. Yu. Implementation of mixed methods as finite difference methods and applications to nonisothermal multiphase flow in porous media. *J. Comput. Math.*, 24(3):281–294, 2006.
- [25] P. G. Ciarlet. *The finite element method for elliptic problems*. North-Holland, Amsterdam, 1978.
- [26] C. Cordes and W. Kinzelbach. Continuous groundwater velocity fields and path lines in linear, bilinear, and trilinear finite elements. *Water Resour. Res.*, 28(11):2903–2911, 1992.

- [27] R. Courant, K. Friedrichs, and H. Lewy. On the partial difference equations of mathematical physics. *IBM Journal*, pages 215–234, March 1967. English translation of the 1928 paper *Über die partiellen Differenzgleichungen der mathematischen Physik* in *Mathematische Annalen*, 100(1):32-74.
- [28] A. Datta-Gupta and M. J. King. *Streamline Simulation: Theory and Practice*. Society of Petroleum Engineers, Richardson, TX, 2007.
- [29] C. Deutsch. *Geostatistical Reservoir Modeling*. Oxford University Press, 2002.
- [30] J. R. Dormand and P. J. Prince. A family of embedded Runge–Kutta formulae. *J. Comput. Appl. Math.*, 6:19–26, 1980.
- [31] T. Dupont and R. Scott. Polynomial approximation of functions in Sobolev spaces. *Math. Comp.*, 34(150):441–463, 1980.
- [32] L. J. Durlofsky. Numerical calculation of equivalent grid block permeability tensors for heterogeneous porous media. *Water Resour. Res.*, 27(5):699–708, 1991.
- [33] M. G. Edwards. Unstructured, control-volume distributed, full-tensor finite-volume schemes with flow based grids. *Comput. Geosci.*, 6:433–452, 2002.
- [34] M. G. Edwards and C. F. Rogers. Finite-volume discretization with imposed flux continuity for the general tensor pressure equation. *Comput. Geosci.*, 2:259–290, 1998.
- [35] M. Fortin and R. Glowinski. *Augmented Lagrangian Methods: Applications to the Numerical Solution of Boundary-Value Problems*. North-Holland, Netherlands, 1983.

- [36] P. Goovaerts. *Geostatistics for Natural Resources Evaluation*. Oxford University Press, 1997.
- [37] H. Hægland. *Streamline Tracing on Irregular Grids*. Cand. Scient Thesis, University of Bergen, Dept. of Mathematics, December 2003.
- [38] H. Hægland, H. K. Dahle, G. T. Eigestad, K.-A. Lie, and I. Aavatsmark. Improved streamlines and time-of-flight for streamline simulation on irregular grids. *Adv. Water Resour.*, 30(4):1027–1045, 2007.
- [39] T. J. R. Hughes. *The Finite Element Method: Linear Static and Dynamic Finite Element Analysis*. Prentice-Hall, Englewood Cliffs, NJ, 1987. Reprinted with corrections, Dover, New York, 2000.
- [40] R. Juanes. *Flow Based Grids for Reservoir Simulation*. Masters thesis, Department of Petroleum Engineering. Stanford University, 2001.
- [41] R. Juanes and S. F. Matringe. Unified formulation for high-order streamline tracing on two-dimensional unstructured grids. *J. Sci. Comput.*, 2006. (Accepted).
- [42] R. A. Klausen and T. F. Russell. Relationships among some locally conservative discretization methods which handle discontinuous coefficients. *Comput. Geosci.*, 8(4):341–377, 2004.
- [43] R. A. Klausen and R. Winther. Convergence of multipoint flux approximations on quadrilateral grids. *Numer. Methods Partial Differential Equations*, 22(6):1438–1454, 2006.
- [44] R. A. Klausen and R. Winther. Robust convergence of multi point flux approximations on rough grids. *Numer. Math.*, 104(3):317–337, 2006.

- [45] S. H. Lee, P. Jenny, and H. A. Tchelepi. A finite-volume method with hexahedral multiblock grids for modeling flow in porous media. *Comput. Geosci.*, 6:353–379, 2002.
- [46] S. H. Lee, H. Tchelepi, P. Jenny, and L. F. DeChant. Implementation of a flux-continuous finite-difference method for stratigraphic, hexahedron grids. *Soc. Pet. Eng. J.*, 7(3):267–277, September 2002.
- [47] J.-L. Mallet. *Geomodeling*. Oxford University Press, 2002.
- [48] J. E. Marsden and T. J. R. Hughes. *Mathematical Foundations of Elasticity*. Prentice-Hall, Englewood Cliffs, NJ, 1983. Reprinted with corrections, Dover, New York, 1994.
- [49] S. F. Matringe. *On Accurate Streamline Tracing and Coverage*. Master’s thesis, Stanford University, January 2004.
- [50] S. F. Matringe, R. Juanes, and H. A. Tchelepi. Robust discretization method for tensor permeabilities and unstructured grids. In *European Conference on the Mathematics of Oil Recovery, ECMOR X*, Amsterdam, The Netherlands, September 4–7 2006. (Paper B025).
- [51] S. F. Matringe, R. Juanes, and H. A. Tchelepi. Robust streamline tracing for the simulation of porous media flow on general triangular and quadrilateral grids. *J. Comput. Phys.*, 219:992–1012, doi:10.1016/j.jcp.2006.07.004, 2006.
- [52] S. F. Matringe, R. Juanes, and H. A. Tchelepi. Mixed finite element and related control volume discretizations for reservoir simulation on three-dimensional unstructured grids. In *SPE Reservoir Simulation Symposium*, Houston, TX, February 26–28 2007. (SPE 106117).

- [53] S. F. Matringe, R. Juanes, and H. A. Tchelepi. A new mixed finite element on hexahedra that reduces to a cell-centered finite difference method. *Numer. Math.*, 2007. Submitted.
- [54] S. F. Matringe, R. Juanes, and H. A. Tchelepi. Streamline tracing on general triangular or quadrilateral grids. *Soc. Pet. Eng. J.*, 12(2):pp. 217–233, June 2007.
- [55] S. F. Matringe, R. Juanes, and H. A. Tchelepi. Tracing streamlines on unstructured grids from finite volume discretizations. *Soc. Pet. Eng. J.*, 2008. (SPE 103295) – Accepted.
- [56] R. Mosé, P. Siegel, P. Ackerer, and G. Chavent. Application of the mixed hybrid finite element approximation in a groundwater flow model: Luxury or necessity? *Water Resour. Res.*, 30(11):3001–3012, 1994.
- [57] R. L. Naff, T. F. Russell, and J. D. Wilson. Shape functions for velocity interpolation in general hexahedral cells. *Comput. Geosci.*, 6(3–4):285–314, 2002.
- [58] J. C. Nédélec. Mixed finite elements in \mathbb{R}^3 . *Numer. Math.*, 35:315–341, 1980.
- [59] J. C. Nédélec. A new family of mixed finite elements in \mathbb{R}^3 . *Numer. Math.*, 50:57–81, 1986.
- [60] D. W. Pollock. Semianalytical computation of path lines for finite difference models. *Ground Water*, 26:743–750, 1988.
- [61] M. Prevost. *Accurate coarse reservoir modeling using unstructured grids, flow-based upscaling and streamline simulation*. PhD Dissertation, Stanford University, Stanford, CA, December 2003.
- [62] M. Prevost, M. G. Edwards, and M. J. Blunt. Streamline tracing on curvilinear structured and unstructured grids. *Soc. Pet. Eng. J.*, 7(2):139–148, June 2002.

- [63] P. A. Raviart and J. M. Thomas. A mixed finite element method for second order elliptic problems. In I. Galligani and E. Magenes, editors, *Mathematical Aspects of the Finite Element Method*, volume 606 of *Lecture Notes in Mathematics*, pages 292–315, New York, 1977. Springer-Verlag.
- [64] T. F. Russell and M. F. Wheeler. Finite element and finite difference methods for continuous flows in porous media. In R. E. Ewing, editor, *The Mathematics of Reservoir Simulation*, pages 35–106. SIAM, Philadelphia, PA, 1983.
- [65] S. Strebelle. *Sequential Simulation Drawing Structures from Training Images*. PhD Dissertation, Stanford University, 2000.
- [66] J.-M. Thomas. *Sur l'analyse numérique des éléments finis hybrides et mixtes*. Thèse de doctorat d'état, Université Pierre et Marie Curie, France, 1977.
- [67] S. Verma and K. Aziz. A control volume scheme for flexible grids in reservoir simulation. In *SPE Reservoir Simulation Symposium*, Dallas, TX, June 8–11 1997. (SPE 37999).
- [68] M. Vohralik. Equivalence between mixed finite element and multi-point finite volume methods. *C. R. Acad. Sci. Paris, Sér I*, 339:525–528, 2004.
- [69] A. Weiser and M. F. Wheeler. On convergence of block-centered finite differences for elliptic problems. *SIAM J. Numer. Anal.*, 25(2):351–375, 1988.
- [70] M. F. Wheeler and I. Yotov. A multipoint flux mixed finite element method. *SIAM J. Numer. Anal.*, 44(5):2082–2106, 2006.
- [71] A. Younes, P. Ackerer, and G. Chavent. From mixed finite elements to finite volumes for elliptic PDEs in two and three dimensions. *Int. J. Numer. Meth. Engrg.*, 59:365–388, 2004.

- [72] O. C. Zienkiewicz and R. L. Taylor. *The Finite Element Method (3 vols), 1: The Basis, 2: Solid Mechanics, 3: Fluid Dynamics*. Butterworth-Heinemann, Oxford, fifth edition, 2000.